UCGE Reports
Number 20241

Department of Geomatics Engineering

Integration of Photogrammetry and LIDAR

(URL: http://www.geomatics.ucalgary.ca/research/publications/GradTheses.html)

by

Mwafag Ghanma

April 2006

UNIVERSITY OF CALGARY

Integration of Photogrammetry and LIDAR

by

Mwafag Ghanma

A THESIS

SUBMITTED TO THE FACULTY OF GRADUATE STUDIES

IN PARTIAL FULFILMENT OF THE REQUIREMENTS FOR THE

DEGREE OF DOCTOR OF PHILOSOPHY

DEPARTMENT OF GEOMATICS ENGINEERING

CALGARY, ALBERTA

APRIL, 2006

ABSTRACT

Photogrammetry is the art and science of deriving accurate 3D metric and descriptive object information from multiple analog and digital images. Photogrammetric reconstruction produces surfaces that are rich in semantic information, which can be clearly recognized in the captured imagery. The inherent redundancy associated with photogrammetric restitution results in highly accurate surfaces. Nevertheless, the extended amount of effort and time required by the photogrammetric reconstruction procedure is a major disadvantage. In LIDAR mapping, spatial coordinates of object space points are directly acquired, enabling quick turnaround of mapping products. Still, the positional nature of LIDAR points makes it difficult to derive semantic surface information such as discontinuities and types of observed structures. Additionally, no inherent redundancy is available in the reconstructed surfaces that may be utilized to enhance the accuracy of such surfaces. The complementary characteristics between photogrammetry and LIDAR, if exploited, can lead to a more complete surface description. The synergic advantages of both systems can be fully utilized only after the precise calibration of both systems and the successful registration of the photogrammetric and LIDAR data relative to a common reference frame. In this thesis, two new methodologies are introduced for the co-registration of LIDAR and photogrammetric datasets. Generally, a registration methodology has to deal with three issues: registration primitives, transformation function, and similarity measure. One track of methodologies uses straight-lines while the other uses planar patches as the registration primitives. The mathematical model and similarity measures corresponding to both types of primitives are also realized. In the straight-lines track, the registration methodology is implemented

in two ways; one step and two step procedures. The two-step procedure, besides registering the involved datasets, was meant to facilitate the detection of systematic errors in the imaging system. Also, the two-step procedure extended the purpose of LIDAR-imagery integration to more general LIDAR-LIDAR dataset registration. For the purpose of studying the effect of LIDAR data processing on the registration outcomes, a number of techniques were considered for extracting straight-lines form LIDAR datasets. In one attempt, straight lines were extracted from intersecting segmented LIDAR patches, while in a lower cost attempt, LIDAR intensity and range images interpolated in different methods were used for the same purpose. In the planar patches track, planar patches proved their efficiency, not only for registering together both LIDAR and photogrammetric datasets, but exceeded that to be used in successfully self-calibrating the involved camera.

The devised methodologies were tested and proved efficient in a multi sensor environment. On the imaging side, datasets acquired by satellite linear array scanner, analog aerial photogrammetric camera, and medium and small format digital cameras were involved in the experimentation. Auxiliary GPS and INS data were available for a part of the photogrammetric datasets. For LIDAR systems, point clouds from three types of scanners were used.

ACKNOWLEDGEMENTS

This thesis would not have been possible without the support of many people. First and foremost, I would like to express my sincere appreciation to my adviser Prof. Ayman Habib for his guidance and insight throughout the span of my studies. I owe him my basic and advanced knowledge in analog and digital photogrammetry. He never skipped an opportunity to enrich my experience in the academic and professional fields. His creativeness and wealth of scientific knowledge were an endless source of ideas that highly contributed to my research.

I wish to express my deep appreciation to Dr. Naser El-Sheimy, Dr. Matthew Tait, Dr. Simon Park, and Dr. Jie Shan for carefully reading and providing comments concerning various aspects of this research.

Of course, I am also indebted to many colleagues at the Digital Photogrammetry Research Group and beyond. I would like to especially acknowledge Changjae Kim, Doctors Rami Al-Ruzouq, Michel Morgan, and Eui Myoung Kim for the help and fruitful discussions we had together.

The author gratefully acknowledges Professor Edson Mitishita of Federal University of Paraná, Brazil, the Technology Institute for Development – LACTEC – UFPR, Brazil, and the Korean Electronics and Telecommunications Research Institute (ETRI) for providing a variety of datasets, which were used in the experimental results section.

Last but not least, I would like to thank my family and my friends for their patience and support. This was very important to me.

DEDICATION

To my beloved family

Jumana, Victoria, and Christopher

TABLE OF CONTENTS

APPROVAL PAGE ii

ABSTRACT ii

ACKNOWLEDGEMENTS iv

DEDICATION v

LIST OF TABLES x

LIST OF FIGURES xi

LIST OF SYMBOLS, ABBREVIATIONS, NOMENCLATURE xv

CHAPTER 1 1

INTRODUCTION 1

1.1 Problem Definition 1

1.2 Research Objectives and Scope 3

1.3 Thesis Outline 7

CHAPTER 2 8

LITERATURE REVIEW 8

2.1 Introduction 8

2.2 LIDAR overview 9

2.3 Photogrammetric Mapping Overview 12

2.4 Synergy between Photogrammetry and LIDAR 15

2.5 LIDAR-Photogrammetry Co-Registration: Overview and Rationale 17

2.5.1 Registration Primitives 19

2.5.2 Transformation Function 23

2.5.3 Similarity Measure 29

CHAPTER 3 34

CO-REGISTRATION METHODOLOGY USING LINEAR FEATURES 34

3.1 Introduction 34

3.2 Straight Lines as the Registration Primitives 34

3.2.1 Photogrammetric Straight-Lines 35

3.2.2 LIDAR Straight Lines 38
3.3 Mathematical Model: Direct incorporation of LIDAR features in the photogrammetric triangulation; One-Step Registration 41
3.4 Mathematical Model: LIDAR features for the absolute orientation of an arbitrarily established photogrammetric model; Two-Step Registration 43
3.4.1 Transformation Function 45
3.4.2 Similarity Measure 47

CHAPTER 4 53
CO-REGISTRATION METHODOLOGY USING PLANAR PATCHES 53
4.1 Introduction 53
4.2 Photogrammetric and LIDAR Planar Patches 54
4.2.1 Photogrammetric Patches: Representation and Extraction 55
4.2.2 LIDAR Patches: Representation and Extraction 55
4.3 Mathematical Model: Transformation Function and Similarity Measure 57
4.4 Mathematical Model: Implementation 59
4.5 Minimum Configuration 61
4.6 The Stochastic Model 63

CHAPTER 5 64
EXPERIMENTS AND RESULTS 64
5.1 Introduction 64
5.2 Objectives of Experimental Work 65
5.3 Implemented Sensors 66
5.3.1 Involved imaging sensors 67
5.3.2 Involved LIDAR scanners 67
5.4 Experiments Set I 70
5.4.1 Objectives 70
5.4.2 Dataset used 70
5.4.3 Evaluation Criteria 72
5.4.4 Processing outline 72

5.4.5 Conclusions....75
5.5 Experiments Set II.... 75
5.5.1 Objectives 76
5.5.2 Involved datasets 76
5.5.3 Evaluation Criteria....77
5.5.4 Processing outline....78
5.5.5 Conclusions....83
5.6 Experiments Set III.... 84
5.6.1 Objectives 84
5.6.2 Involved datasets 85
5.6.3 Evaluation Criteria....87
5.6.4 Processing outline....87
5.6.5 Conclusions....95
5.7 Experiments Set IV 96
5.7.1 Objectives 96
5.7.2 Involved datasets 97
5.7.3 Evaluation Criteria....98
5.7.4 Processing outline....98
5.7.5 Conclusions....106
5.8 Experiments Set V.... 107
5.8.1 Objectives 107
5.8.2 Involved datasets 107
5.8.3 Evaluation Criteria....110
5.8.4 Processing outline....110
5.8.5 Conclusions....118

CHAPTER 6 119
CONCLUSIONS AND FUTURE WORK 119
6.1 Conclusions 119
6.2 Recommendations for Future Work 125
REFERENCES 128

APPENDIX A 133
Stochastic Model of the Planar Patches Mathematical Model 133
APPENDIX B 139
Published Work 139

LIST OF TABLES

Table 2.1. Photogrammetric weaknesses as contrasted by LIDAR strengths.................. 16
Table 2.2. LIDAR weaknesses as contrasted by Photogrammetric strengths.................. 16
Table 5.1. Imaging sensors utilized in the experimental work 67
Table 5.2. Imaging sensors utilized in the experimental work 68
Table 5.3. Check-point analysis for point- and line-controlled bundle adjustment.......... 73
Table 5.4. Check-point analysis for point- and line-controlled bundle adjustment.......... 74
Table 5.5. The 3D similarity transformation parameters between LIDAR and photogrammetric model 80
Table 5.6. The 3D similarity parameters between LIDAR and photogrammetric models after radial distortion compensation.. 81
Table 5.7. Quality of fit of the 1-step procedure between Canon EOS 1D and LIDAR .. 82
Table 5.8. RMSE results of check points from 1- and 2-step procedures 83
Table 5.9. Specification and rationale of LIDAR data interpolation alternatives 89
Table 5.10. Check-point analysis of 1-step procedure of LIDAR – RC10 datasets 91
Table 5.11. Check-point analysis of 1-step procedure of LIDAR – SONY 717 datasets. 91
Table 5.12. Mean of normal distances between conjugate RC10 and LIDAR lines after absolute orientation 94
Table 5.13. Mean of normal distances between conjugate SONY F717 and LIDAR lines after absolute orientation... 95
Table 5.14. Check-point analysis for point- and patch-controlled bundle adjustment ... 100
Table 5.15. Camera calibration parameters using six patches as compared to original CCC.. 101
Table 5.16. Check-point analysis for point-controlled bundle adjustment..................... 102
Table 5.17. Check-point analysis for point-, line-, and patch-controlled bundle adjustment 103
Table 5.18. Check-point analysis for point-, line-, and patch-controlled bundle adjustment 104
Table 5.19. Check-point analysis for 10 point-controlled bundle adjustment with self-calibration.. 106
Table 5.20. Check-point analysis of MST bundle adjustment results 113

LIST OF FIGURES

Figure 2.1. Paradigm of LIDAR scanning (a) [Kraus 2002] emitted pulse interacting with ground objects (b) returned signal detected by the receiver (c) 10
Figure 2.2. Visualization of LIDAR coverage: shaded relief map of range data (a) and intensity image (b).. 10
Figure 2.3. Coordinate systems and parameters involved in direct georeferencing of LIDAR systems 12
Figure 2.4. A block of imagery georeferenced using ground control points – Indirect georeferencing.. 14
Figure 2.5. A block of imagery georeferenced using GPS/INS systems – Direct georeferencing.. 15
Figure 2.6. Examples of primitive alternatives in imagery... 20
Figure 2.7. Line and areas as clusters of individually measured points 20
Figure 2.8. LIDAR lines from intersecting planar patches (a) and as measured from intensity image (b).. 21
Figure 2.9. Similarity measure between two surfaces after transformation where the normal distance is minimized 31
Figure 3.1. Object space lines represented by its 3D end points 35
Figure 3.2. End points of tie lines are measured in one image (a) or in two images (b) while the intermediate points are measured in all images within which the line appears... 36
Figure 3.3. Image space control lines measured as a sequence of 2D intermediate points 37
Figure 3.4. LIDAR lines are used as a source of control to align the photogrammetric model in the 2-step procedure 38
Figure 3.5. Manually identified planar patches in the LIDAR data (a) guided by the corresponding optical image (b) in aerial datasets... 39
Figure 3.6. Manually measuring planimetric coordinates from intensity image (a) and height value from range image (b). 40
Figure 3.7. Similarity measure (coplanarity constraint) between photogrammetric and LIDAR features after transformation 41

Figure 3.8. Perspective transformation between image and LIDAR control straight lines and the coplanarity constraint for intermediate points along the line 42
Figure 3.9. Perspective transformation between image and model space straight lines and the coplanarity constraint for intermediate points along the line 45
Figure 3.10. 3D similarity transformation where the model undergoes translation, rotation, and scale 46
Figure 3.11. Similarity measure between photogrammetric and LIDAR linear features . 47
Figure 3.12. Singular (a) and optimum (b) configurations to recover rotation angles 49
Figure 3.13. Singular (a) and optimum (b) configurations to recover scale and shift components 51
Figure 4.1. LIDAR patches as a source of control for photogrammetric georeferencing 54
Figure 4.2. Photogrammetric and LIDAR coverage of a common planar surface 55
Figure 4.3. Photogrammetric planar patch represented by three points (A,B,C). LIDAR patch points are also shown on the roof 56
Figure 4.4. LIDAR patches manually identified and extracted with the aid of imagery .. 57
Figure 4.5. Photogrammetric (A,B,C) points and LIDAR patch points 58
Figure 4.6. Photogrammetric and LIDAR coverage of a common planar surface 58
Figure 4.7. Optimal configuration required to establish the datum using planar patches methodology 62
Figure 5.1. Laser scanners used to capture LIDAR datasets. 68
Figure 5.2. Coverage of RC10 color imagery. The red outline shows Kodak coverage .. 71
Figure 5.3. Coverage of Kodak 14N camera 71
Figure 5.4. Shaded-relief map of OPTECH LIDAR coverage 72
Figure 5.5. Coverage of Canon EOS 1D camera 76
Figure 5.6. Shaded-relief map of RIEGL LIDAR coverage 77
Figure 5.7. Manually identified planar patches in the LIDAR data (a) guided by the corresponding optical image in aerial datasets (b) 79
Figure 5.8. Plane fitting and blunder detection from LIDAR patches (a) and plane intersection for extracting LIDAR lines (b) 79
Figure 5.9. Photogrammetric and LIDAR datasets after transformation......................... 80

Figure 5.10. Aerial photogrammetric and LIDAR datasets after transformation and proper camera calibration 82
Figure 5.11. Coverage of RC10 B/W imagery. The yellow outline shows SONY F717 coverage 85
Figure 5.12. Coverage of SONY F717 camera 86
Figure 5.13. Shaded-relief map of OPTECH 2050 LIDAR coverage 86
Figure 5.14. Interpolated LIDAR range data visualized as range image (a) and intensity image (b). 88
Figure 5.15. Manually measuring planimetric coordinates from intensity image (a) and height value from range image (b). 88
Figure 5.16. Distribution of lines extracted from intensity images -I1 and I2- ( ) and from patch intersection ( ) technique 90
Figure 5.17. Simulated photogrammetric and LIDAR dataset 98
Figure 5.18. Planned experiments flow for the dataset 99
Figure 5.19. Estimating and assessing the camera parameters 100
Figure 5.20. DSS upper image block (a) and the corresponding LIDAR cloud (b) 108
Figure 5.21. DSS middle image block (a) and the corresponding LIDAR cloud (b) 108
Figure 5.22. DSS lower image block (a) and the corresponding LIDAR cloud (b) 109
Figure 5.23. DSS imagery and LIDAR coverage location on the IKONOS scene 109
Figure 5.24. Layout and distribution of control points in IKONOS scenes coverage 110
Figure 5.25. Process plan implemented for this dataset 111
Figure 5.26. Control and check points layout and distribution over IKONOS imagery 112
Figure 5.28. Check-point analysis from bundle adjustments involving IKONOS and DSS imagery 115
Figure 5.29. Check-point analysis from bundle adjustments involving IKONOS and DSS imagery (enlarged view of Figure 5.28) 116
Figure 5.27. Check points errors for control patches and 15 control points with no GPS experiment in X-direction (a), Y-direction (b), and Z-direction (c) 117
Figure 6.1. A patch of LIDAR intensity image overlaid by SONY-F717 orthophoto ... 120

Figure 6.2. Change detection between DSS (color) and IKONOS (b/w) orthophotos. Smooth transition between the two orthophotos can be observed in (a) while discontinuities are observed in (b) due to changes in the object space. 126
Figure 6.3. Textured 3D model produced by rendering optical images on LIDAR data 126
Figure 6.4. An orthophoto generated from Canon EOS 1D imagery in KOREA I dataset using differential rectification (a) and using true orthophoto generation technique (b).. 127
Figure A.1. Updates to the normal matrix **N** 138
Figure A.2. Updates to the normal vector **C** 138

LIST OF SYMBOLS, ABBREVIATIONS, NOMENCLATURE

$\hat{\sigma}_o^2$	Variance Component (a posterior variance factor) characterizes the precision of adjustment procedure
X, Y, Z	Ground Point Coordinates
X_o, Y_o, Z_o ω, φ, κ	Exterior Orientation Parameters (X_o, Y_o and Z_o represent the position of perspective center with respect to ground coordinate system, where ω, φ and κ represent the rotation angles between the ground and image coordinate systems)
x_p, y_p, c	Interior Orientation Parameters (Calibrated principal point position and principal distance of the camera with respect to image coordinate system)
2D	Two Dimensional
3D	Three Dimensional
CCD	Charge- Coupled Device
DEM	Digital Elevation Model
EOP	Exterior Orientation Parameters
GCP	Ground Control Point
GPS	Global Positioning System
IMU	Inertial Measurement Unit
INS	Inertial Navigation System
IOP	Interior Orientation Parameters
LIDAR	LIght Detection And Ranging
MMS	Mobile Mapping Systems
MST	Multi Sensor Triangulation
RMSE	Root Mean Square Error

CHAPTER 1

INTRODUCTION

1.1 Problem Definition

LIDAR and photogrammetric datasets have prominent synergic properties that, if integrated, will lead to better and faster mapping products. Photogrammetry, as an established mapping technique, requires reliable control information in order to produce accurate results. LIDAR data, with its 3D representation of the object space, is a potential source of control for photogrammetric triangulation. The inclusion of LIDAR control into the photogrammetric reconstruction can be viewed as a co-registration procedure between the two datasets. This co-registration step is essential since it leads to both datasets being described relative to the same reference frame, a prerequisite for utilizing the synergy between the two systems. In general, a registration process has three major components to be considered, mainly; the registration primitives, the transformation function that mathematically relates the datasets under consideration using the extracted primitives, and finally the similarity measure which ensures the coincidence of conjugate primitives after applying the transformation function. In light of the above, some fundamental issues are believed to hinder proper integration between photogrammetric and LIDAR data. Such issues can be categorized into the following main subjects:

- <u>Registration primitives</u>: While the majority of registration methodologies rely on point primitives for solving the registration problem between datasets, it is nearly impossible to establish a direct correspondence between a laser footprint and a certain point of interest in the imagery due to the discrete nature of collected LIDAR points. This indicates that point primitives are not suitable for LIDAR datasets. Hence, other higher level primitives, like linear and areal features, should be considered. The representation of these features in LIDAR and photogrammetric processing should alleviate any probable singularities related to such representation.

- Feature extraction issue: LIDAR primitives can be extracted from the multiple return raw point clouds and laser returned-intensity maps, which, based on the area covered and the sampling rate, can be in the range of hundreds of megabytes. Also, previous research attempts relied mainly on interpolated LIDAR datasets that made it compatible with that of standard photogrammetric procedures for feature identification and measurement. It proves useful if new methodologies can be added that utilize raw LIDAR data.

- Mathematical models: To cope with the linear and areal features, new mathematical models must be devised to establish the relation between the registered photogrammetric and LIDAR data which are assumed to be free of systematic errors. Hence, the mathematical models should also be extended, as possible, towards investigating any systematic biases in the datasets.

- Similarity measures: Along with the selection of registration primitives and the corresponding mathematical model, suitable similarity measures must also be defined to judge the proper alignment of registered datasets after implementing the registration procedure.

- Platform applicability: Although the delivery of LIDAR datasets is consistent in the form of range and intensity images, the situation is not quit the same for photogrammetric datasets. A plethora of imaging systems are now available for satellite-, aerial-, and terrestrial-based platforms. The diversity starts with analog and digital frame cameras and continues to include one- and three-line scanners. The revolution in the size, quality, and availability of digital imaging sensors is adding to the challenge of processing such photogrammetric datasets. The proposed methodologies should be applicable, as possible, to all variations of available datasets.

1.2 Research Objectives and Scope

The objective of this research is to introduce new methodologies for integrating LIDAR and photogrammetric systems. One track of methodologies will use straight-line features and the other will use planar patches. For both tracks the following points will be considered:

<u>Feature representation & extraction from imagery and LIDAR</u>

The representation scheme of 3D straight lines and planar patches in the object and image space is central to the methodology for producing such features from the photogrammetric and LIDAR datasets. For 3D straight lines, the representation and extraction of such lines in the image and object space will adopt the recommendations made by Habib et al. (2002) for producing well-defined lines. The conjugate lines from LIDAR datasets will be represented in the same way as the object space lines. Planar patches, on the other hand, will be represented in the image and object space by three distinct points, while the collection of raw LIDAR points falling on the same patch will be used to represent the patch in the LIDAR dataset. As for feature extraction, straight-line features will be extracted from LIDAR data in two methods. Firstly, neighboring planar patches are segmented from the cloud of raw points then intersected to produce the desired straight lines. Secondly, the lines are directly measured from intensity and range images interpolated in different methods and parameters. Planar patches from LIDAR dataset are manually identified, segmented, and extracted as a collection of raw 3D points. In imagery, the planar patches are represented by three points which are measured in all overlapping images.

Registration transformation function

An essential property of any registration technique is the type of transformation or mapping function adopted to properly overlay the two datasets. For 3D straight lines approach, two methodologies are developed. In the first, a one-step bundle adjustment procedure directly incorporates LIDAR lines as the source of control to establish the datum. The second method is based on preliminary and independent processing of the LIDAR and photogrammetric data. Then, conjugate LIDAR and photogrammetric lines are utilized in an absolute orientation procedure. The purpose of this two-step procedure is to explicitly monitor the behavior of each dataset before, during, and after the absolute orientation, as opposed to the above one-step method. For planar patches, the one-step procedure for directly introducing LIDAR patch points into the photogrammetric bundle adjustment is adopted.

Similarity measures

The mathematical formulation of the similarity measure depends on the selected registration primitives and their respective attributes as well as the mathematical model. For 1-step procedure incorporating 3D straight lines, the similarity measure is set to ensure that the projected LIDAR lines coincide with the photogrammetric lines in the image space. When the two-step procedure is applied, the similarity measure is formulated to verify that the reconstructed photogrammetric model lines coincide with the LIDAR lines after transformation. The similarity measure for planar patches is based on the fact that individual LIDAR points of a certain patch must be coplanar with the conjugate patch reconstructed from the photogrammetric dataset and represented by three points.

In general, the developed methodologies will target aerial-based frame and line cameras and satellite-based line cameras. Frame cameras include the traditional metric analog ones in addition to the metric and off-the-shelf digital types of cameras. The low-cost and stability of medium-format digital imaging systems is pushing towards its usage in mapping applications and research work. The proposed registration methodologies will be tested for its applicability on this common stream of digital frame cameras.

In summary, the contribution of this thesis can be manifested in the following:

- Two new methodologies are introduced for the co-registration of LIDAR and photogrammetric datasets. One track of methodologies uses straight-lines while the other uses planar patches as the registration primitives. The mathematical model and similarity measures corresponding to both types of primitives are also realized.

- In the straight-lines track, the registration methodology is implemented in two ways; one step and two step procedures. The two-step procedure, besides registering the involved datasets, was meant to facilitate the detection of systematic errors in the imaging system. Also, the two-step procedure extended the purpose of LIDAR-imagery integration to more general LIDAR-LIDAR dataset registration. For the purpose of studying the effect of LIDAR data processing on the registration outcomes, a number of techniques were considered for extracting straight-lines form LIDAR datasets. In one attempt, straight lines were extracted from intersecting segmented LIDAR patches, while in a lower cost attempt, LIDAR intensity and range images interpolated in different methods were used for the same purpose.

- In the planar patches track, planar patches proved their efficiency, not only for registering together both LIDAR and photogrammetric datasets, but exceeded that to be used in successfully self-calibrating the involved camera.

- The devised methodologies were tested and proved efficient in a multi sensor environment. On the imaging side, datasets acquired by satellite linear array scanner, analog aerial photogrammetric camera, and medium and small format digital cameras were involved in the experimentation. Auxiliary GPS and INS data were available for a part of the photogrammetric datasets. For LIDAR systems, point clouds from three types of scanners were used.

1.3 Thesis Outline

- Chapter 2 presents an overview of the photogrammetric and LIDAR mapping followed by components of the co-registration methodology/paradigm, and finally a literature review of the existing co-registration techniques is conducted.
- Chapter 3 introduces the co-registration methodology of LIDAR and photogrammetric datasets using straight line features.
- Chapter 4 details the co-registration methodology of LIDAR and photogrammetric datasets using planar patches.
- Chapter 5 describes the experiments carried out to demonstrate the feasibility and robustness of the proposed methodologies.
- Chapter 6 lists the conclusions drawn from this study and recommends future steps.

CHAPTER 2

LITERATURE REVIEW

2.1 Introduction

Different technologies have been recently developed for fast and reliable data collection over physical surfaces. Such developments were driven primarily by the growing demand by modern mapping applications such as true ortho-photo generation, city modeling, and object recognition. High quality digital imaging and LIDAR systems are examples of such evolving techniques. The new systems were accompanied by a vast increase in the volume and diverse characteristics of the collected data, a situation that needed efficient and reliable data handling procedures. LIDAR and photogrammetric systems are receiving major attention due to their complementary characteristics and potential. LIDAR has the advantage of directly and accurately capturing digital surfaces and is rapidly maturing on the hardware and supporting software levels. On the other hand, photogrammetry is a well established mapping and surface reconstruction technique that is characterized by high redundancy through observing desired features in multiple images.

In general, data points in a captured dataset from any acquisition system, including LIDAR and photogrammetry, should be associated with specific reference coordinate system on the earth’s surface. This leads to the term –georeferencing, which can be defined as “the assignment of coordinates of an absolute geographic reference system to a geographic feature” (ANZLIC 2006). In photogrammetry and LIDAR literature, georeferencing is a term given to the positioning and orientation of the sensor itself, which is then propagated to the acquired data points through the sensor mathematical model (Cramer et al. 2000, Wegmann et al. 2004).

In Sections 2.2 and 2.3, an overview of LIDAR and photogrammetric mapping systems is presented along with a description of the georeferencing methods for each system. A side by side comparison and discussion of the pros and cons of both systems are detailed in Section 2.4 followed by the co-registration definition and rationale.

2.2 LIDAR overview

LIDAR (LIght Detection And Ranging) has been conceived as a method to directly and accurately capture digital surfaces. Although 30 years old, the commercial market for LIDAR has only developed significantly within the last seven years (Faruque 2003). The affordability, the increased density, and the versatility of new LIDAR systems are causing an exponential profusion and availability of LIDAR datasets. On the paradigm level, LIDAR scanners are active data acquisition sensors where the measurements are done through emitting laser pulses, Figure 2.1(a). After interacting with the object space as shown in Figure 2.1(b), a portion of the emitted pulse is returned and detected by the receiver, Figure 2.1(c). The time of travel is recorded from which the range between the laser unit and the object is calculated. Besides using the returned signal for time calculations, the intensity of signal echo is also recorded by recent LIDAR scanners, Figure 2.2. The visualization of the intensity map can be used for object space segmentation and understanding. The position of a LIDAR-measured point is directly calculated using the LIDAR equation as shown in Equation 2.1, which involves four coordinate systems, namely: the ground coordinate system (mapping frame), the IMU body frame, the laser unit, and the laser beam coordinate systems.

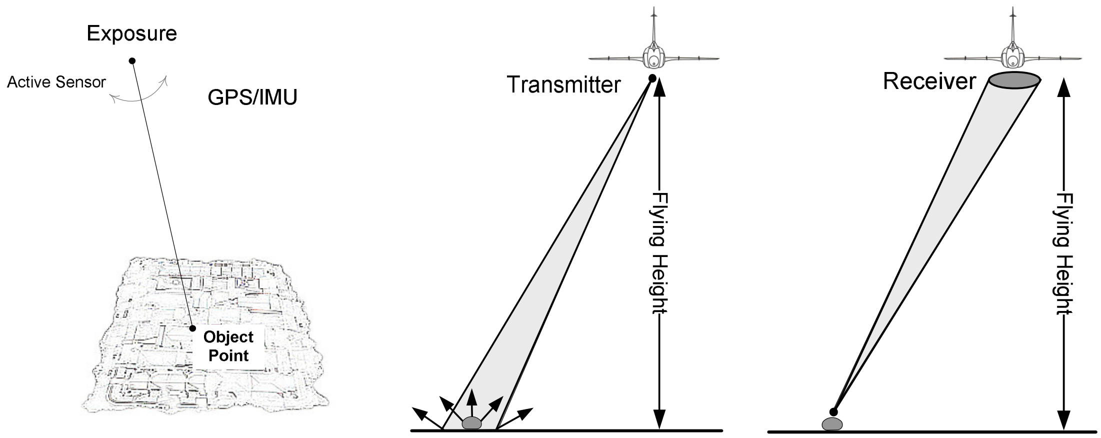

(a) (b) (c)

Figure 2.1. Paradigm of LIDAR scanning (a) [Kraus 2002] emitted pulse interacting with ground objects (b) returned signal detected by the receiver (c)

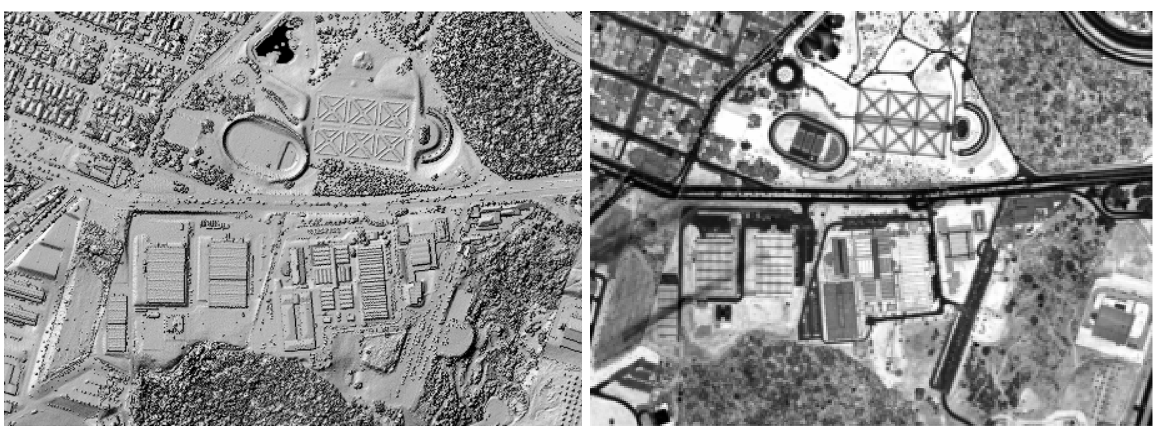

(a) (b)

Figure 2.2. Visualization of LIDAR coverage: shaded relief map of range data (a) and intensity image (b)

$$r_i^m = r_{GPS}^m(t) + R_{INS}^m(t) R_{\text{laser unit}}^{INS} r_{\text{laser unit}}^{INS} + R_{INS}^m(t) R_{\text{laser unit}}^{INS} R_{\text{laser beam}}^{\text{laser unit}}(t) \begin{bmatrix} \mathbf{0} \\ \mathbf{0} \\ -\rho_i \end{bmatrix} \quad (2.1)$$

where,

r_i^m	The coordinate vector of point (*i*) in the mapping frame (m-frame),
$r_{GPS}^m(t)$	The interpolated coordinate vector of GPS in the in the mapping frame,
$r_{laser\ unit}^{INS}$	The lever arm vector between INS center and origin of laser unit coordinate system, determined by calibration,
ρ_i	The coordinate vector of the point (*i*) in the laser beam coordinate system,
$R_{INS}^m(t)$	The interpolated rotation matrix between the IMU body frame (b-frame) and the mapping frame (m-frame),
$R_{laser\ unit}^{INS}$	The differential rotation (boresight) between the laser unit frame and the INS body frame, determined by calibration,
$R_{laser\ beam}^{laser\ unit}(t)$	The differential rotation between the laser beam frame and the laser unit frame at time (*t*), determined by laser scanner mechanism, and
(*t*)	The time of capturing the point, determined by synchronization.

Figure 2.3 also illustrates the parameters involved in the LIDAR equation, which indicate that the final LIDAR point coordinates are calculated with respect to the GPS reference frame (El-Sheimy et. al. 2005). In Equation 2.1 and Figure 2.3, the GPS phase center is assumed to coincide with the origin of the INS body frame (b-frame) after the GPS and INS systems integrationf. Also, from Equation 2.1, it can be inferred that there is no inherent redundancy in the computation of the captured LIDAR surface. Therefore, the overall accuracy depends on the accuracy and calibration of different components comprising the LIDAR system. The systematic errors in a LIDAR system includes, but not limited to, the following errors: range error, mounting errors, INS errors, systematic GPS Error, error in Geoid normal, and time bias. For further details discussion about these errors, please refer to Schenk (2001).

The positional nature of LIDAR data collection makes it difficult to derive semantic information from the captured surfaces (e.g., material and types of observed structures) (Wehr 1999, Baltsavias 1999, Schenk 1999a).

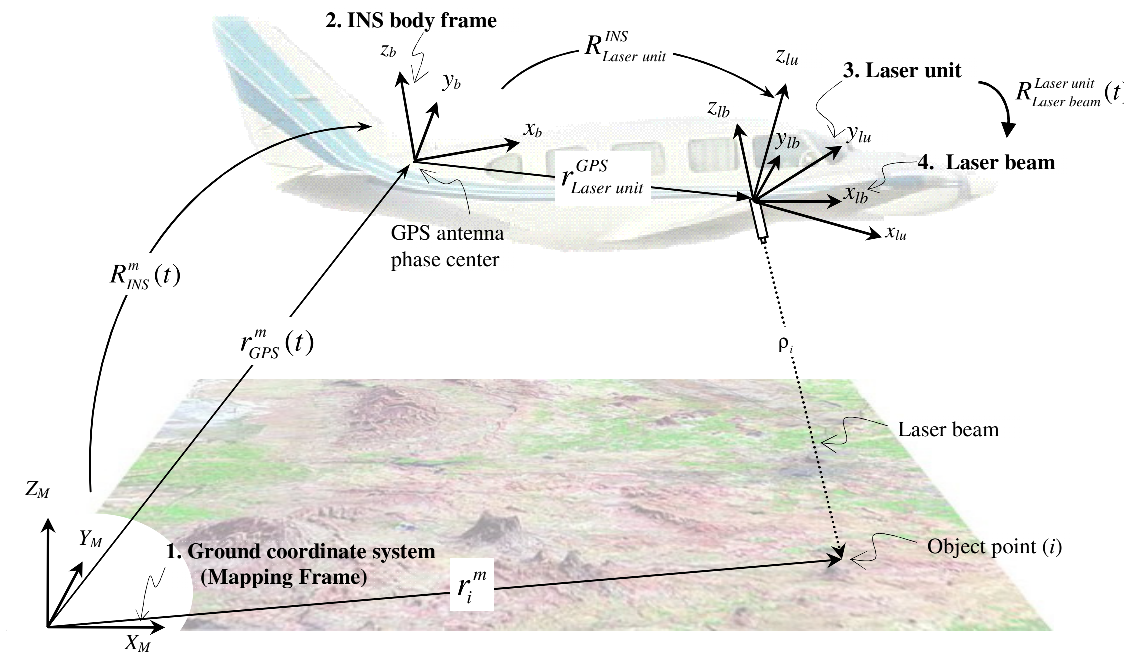

Figure 2.3. Coordinate systems and parameters involved in direct georeferencing of LIDAR systems

2.3 Photogrammetric Mapping Overview

Photogrammetry is the art and science of deriving accurate 3D metric and descriptive object information from multiple analog and digital images (Habib 2006). Reconstructed surfaces from photogrammetric measurements possess a rich body of semantic information that can be easily identified in the captured imagery. Moreover, reconstructed surfaces tend to be highly accurate due to the inherent redundancy associated with photogrammetric operations. Surface reconstruction using analog metric cameras is a well established methodology that has been repeatedly tested and proven over the last few decades. Still, photogrammetric reconstruction of real surfaces requires enough control information to re-establish the position and orientation of imagery (Kraus 1993). The drawback of surface reconstruction from imagery is the significant time consumed by the process of manually identifying conjugate points in overlapping images. Automating the matching problem is a difficult task, especially when dealing with large scale imagery over urban areas (Schenk and Csatho 2002). The imaging sensors witnessed vast development in the digital era. Recent developments in digital cameras, in terms of the sensor size and storage capacity, are leading to their application in traditional and new photogrammetric, surveying, and mapping functions. To attain larger ground coverage, high resolution single line and three line cameras on satellite and aerial platforms are developed and are extensively used. However, using these cameras requires careful calibration to estimate their internal characteristics which generally include: the principal distance, the coordinates of the principal point, and image coordinate corrections that compensate for various deviations from the collinearity model (Habib and Morgan, 2003a).

Traditionally, photogrammetric georeferencing was accomplished indirectly through the establishment of a basic network of image-identifiable ground control points with known horizontal and vertical coordinates relative to a specific ground coordinate system, Figure 2.4 (Kraus 1993, Wolf and Dewitt 2000, Mikhail et. al. 2001, McGlone 2004). Consequently, all features in the reconstructed object space will follow the reference frame in which the photogrammetric control is described. This reference frame can be a global, a local, or even an arbitrarily selected system. With the advent and availability of digital photogrammetric techniques, higher level features other than points could be efficiently used for photogrammetric georeferencing. Linear features were used in most manual and autonomous photogrammetric activities such as resection, intersection, and self-calibration purposes (Mulawa and Mikhail 1988, Heuvel 2000, Habib et al. 2002, Habib and Morgan 2003b, Habib et al. 2003, Schenk 2004). Control patches were also exploited for photogrammetric resection operations (Jaw 1999). In another study, Jaw and Wu (2006) used GIS databases as the source of control patches for photogrammetric bundle adjustment.

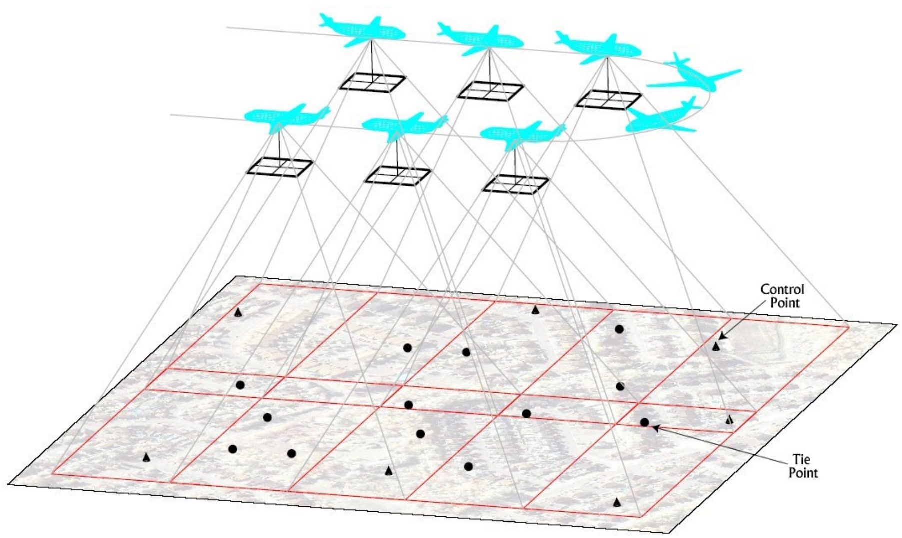

Figure 2.4. A block of imagery georeferenced using ground control points – Indirect georeferencing

The availability of Global Positioning Systems (GPS) and Inertial Navigation Systems (INS) allow for direct collection of dense data for the location and orientation of the imaging sensor during the flight mission, Figure 2.5. Essentially, a reading for each frame of photography flown during the mission is recorded, as opposed to establishing control points spanning three to four models utilizing conventional ground control. The direct collection of the exterior orientation parameters of imagery, using GPS/INS systems, automatically references the reconstructed photogrammetric surfaces to the GPS reference frame, the WGS84 in this case (El-Rabbany 2002).

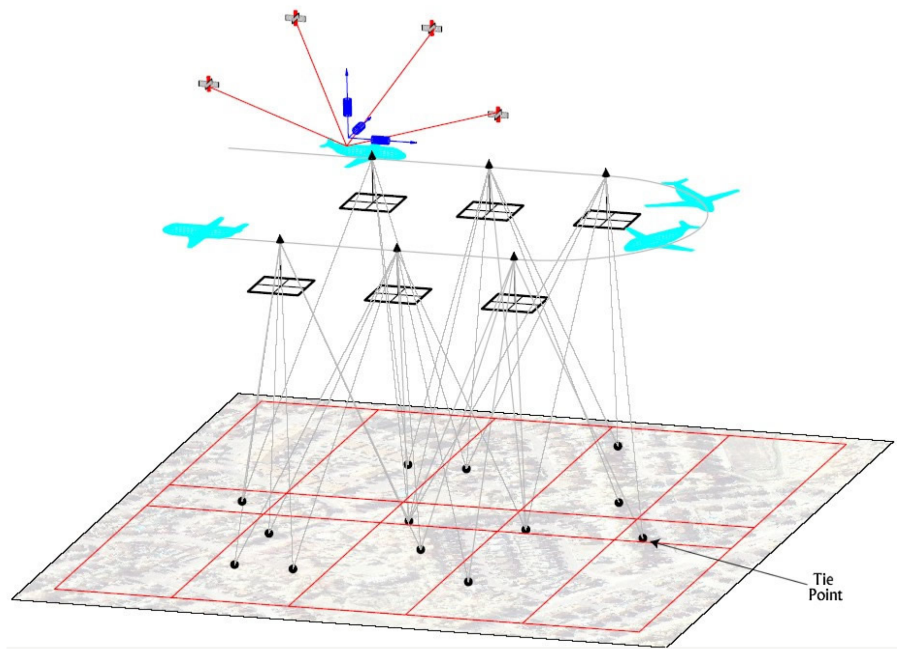

Figure 2.5. A block of imagery georeferenced using GPS/INS systems – Direct georeferencing

2.4 Synergy between Photogrammetry and LIDAR

In light of the inherent and explicit characteristics of the photogrammetric and LIDAR systems, a summary of features can be aggregated as shown in Tables 2.1 and 2.2 below (Baltsavias 1999).

The pros and cons of both LIDAR and photogrammetry and the complementary nature of such characteristics continuously push towards the integration of both systems. Such integration would lead to a more complete surface description from semantic and geometric points of view (Baltsavias 1999, Satale and Kulkarni 2003).

Table 2.1. Photogrammetric weaknesses as contrasted by LIDAR strengths

LIDAR Pros	Photogrammetric Cons
Dense information from homogeneous surfaces	Almost no positional information along homogeneous surfaces
Day or night data collection	Day time data collection
Direct acquisition of 3D coordinates	Complicated and sometimes unreliable matching procedures
Vertical accuracy is better than its planimetric accuracy	Vertical accuracy is worse than the planimetric accuracy

Table 2.2. LIDAR weaknesses as contrasted by Photogrammetric strengths

Photogrammetry Pros	LIDAR Cons
High redundancy	No inherent redundancy
Rich in semantic information	Positional; difficult to derive semantic information
Dense positional information along object space breaklines	Almost no information along breaklines
Planimetric accuracy is better than the vertical accuracy	Planimetric accuracy is worse than the vertical accuracy

The quality of the final synergic product unquestionably depends on the quality achieved from each individual system. Hence, a precise calibration of both systems, which is separately implemented for each system, would guarantee that both datasets are as free of systematic errors as possible (Schenk et. al. 2001). In addition to the calibration requirement for both systems, the synergic characteristics of both systems can be fully utilized only after ensuring that both datasets are georeferenced relative to the same common reference frame (Habib and Schenk 1999, Chen et al. 2004).

2.5 LIDAR-Photogrammetry Co-Registration: Overview and Rationale

The dataset registration process, in its basic definition, aims at combining multiple datasets acquired by different sensors in order to achieve better accuracy and enhanced inference about the environment than could be attained through the use of a single sensor.

A fundamental question is now asked: If both LIDAR and photogrammetric datasets are properly georeferenced to the same reference frame, why would we need to co-register them? To answer this question, two issues are recalled: LIDAR direct georeferencing method and the indirect photogrammetric georeferencing. As stated in Section 2.2, GPS/INS systems are essential components in the LIDAR georeferencing which references the point cloud relative to the GPS ECEF reference frame using the WGS84 ellipsoid. Utilizing LIDAR data as the source of control for the photogrammetric georeferencing is more economical and allows for establishing a common reference frame for multi-temporal and multi-source photogrammetric datasets. Utilizing LIDAR data for the photogrammetric georeferencing can be viewed as a co-registration process. This would combine multiple datasets acquired by different sensors leading to better accuracy and enhanced inference about the object space, serving the definition of the co-registration procedure stated at the beginning of this section.

The variation of reference frames between LIDAR and photogrammetric datasets can occur for several reasons. For example, in many cases, photogrammetric and LIDAR data collection missions are launched and processed independently of each other; hence, the reference frames might vary accordingly. Furthermore, previously processed and archived photogrammetric datasets might be utilized with more recent photogrammetric and LIDAR datasets for change detection purposes; again, there is no guarantee that all reference frames will be similar. As another example, imaging sensors might be flown on the same platform as the LIDAR without being bore-sighted relative to the onboard GPS/INS units. In this case, the processing of image data will depend on visible control, which might be in a different reference frame than that of the LIDAR's. A deceptive source of variation in reference frames can be the redefinition of the same reference frame over different periods of time. The use of the same generic name of such a redefined reference frame can lead to the false belief of identical reference frames.

From the above discussions of photogrammetric and LIDAR georeferencing, it can be inferred that datasets from both sources are not necessarily in the same reference frame. Considering the vast heritage of existing LIDAR and photogrammetric datasets and the ones being acquired, the importance of a proper co-registration methodology is obvious and indispensable.

In general, a registration methodology must deal with three issues. First, a decision has to be made regarding the choice of primitives for the registration procedure. The second issue is concerned with establishing a registration transformation function that mathematically relates the datasets under consideration. Finally, a similarity measure should be devised to ensure the coincidence of conjugate primitives after applying the appropriate transformation function (Brown, 1992). The decision on each of the registration procedure components is directly influenced by the inherent properties of the involved datasets. The traditional registration paradigm involves practices that are not in harmony with the nature of both LIDAR and photogrammetric systems; hence, more innovative application of the co-registration procedure is required. The various components of the registration paradigm are explained through the following outlines of the particularities of each registration component.

2.5.1 Registration Primitives

To register any two datasets, common features have to be identified and extracted from both sets. Such features will be subsequently used as the registration primitives tying the datasets together. The type of chosen primitives greatly influences subsequent registration steps. Hence, it is crucial to first decide upon the primitives to be used for establishing the transformation between the datasets in question (Habib and Schenk, 1999).

When considering registration problems involving spatial data, the three fundamental, and commonly, used registration primitives are points, lines and areal regions. Figure 2.6 shows examples of such features in photogrammetric datasets. Potential features include road intersections, corners of building, rivers, coastlines, roads, lakes, or similar dominant man-made or natural structures. These primitives are ultimately assigned one or more point locations (e.g. centroid of area, line endings, etc.) to represent the primitive in the registration procedure (Fonseca and Manjunath, 1996).

Conventionally, registration methods start with manually selecting a set of tie points in each dataset. These point primitives are then used to establish the registration transformation function from one dataset reference frame to the other. However, such a procedure, which relies on the identification of conjugate points, can lead to inaccurate results and is slow to execute, especially for LIDAR datasets where it is nearly impossible to identify the laser footprint in the corresponding image. At a higher processing cost, three intersecting patches can be segmented and utilized to extract LIDAR points. The above costly facts of collecting LIDAR points exclude point primitives from being the candidate primitive when working with LIDAR data.

Distinct Points Linear Features Areal Regions

Figure 2.6. Examples of primitive alternatives in imagery

Consequently, linear and areal features are the other potential primitives that can be more suitable for datasets involving LIDAR data. With these features, the geometric distribution of the points makes up the feature rather than individual occurrences, Figure 2.7.

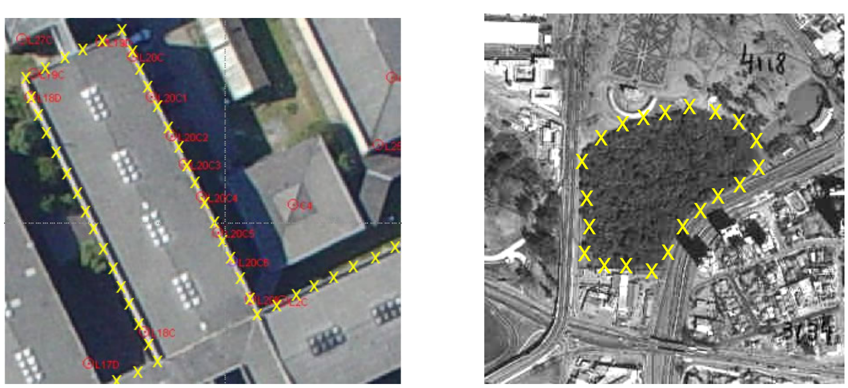

Figure 2.7. Line and areas as clusters of individually measured points

Linear features can be directly measured on involved photogrammetric dataset while conjugate LIDAR lines can be extracted through the use of homogeneous patch intersection or utilizing intensity images produced by most of today's LIDAR systems, Figure 2.8.

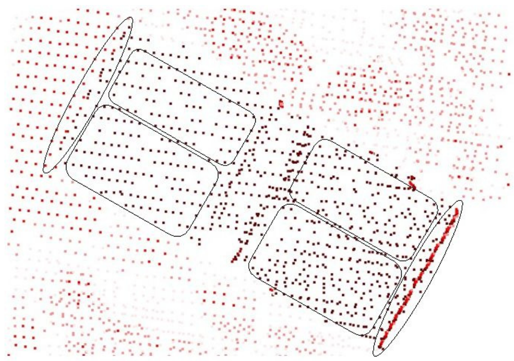

(a)

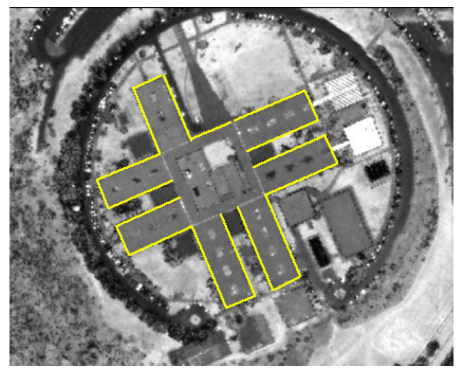

(b)

Figure 2.8. LIDAR lines from intersecting planar patches (a) and as measured from intensity image (b)

Linear features have a set of appealing properties (Habib and Morgan, 2003b), which include the following:

- Compared to distinct points, linear features have higher semantics, which can be useful for subsequent processes (such as DEM generation, map compilation, change detection, and object recognition).
- It is easier to automatically extract linear features from different-type and different-resolution datasets rather than distinct points. This is attributable to the nature of linear features, since they represent discontinuities in one direction. On the other hand, point features represent discontinuity in all directions. Even if the extraction

process is done manually, the identification of conjugate linear features is much easier than the identification of conjugate distinct points.

- Datasets of a man-made environment are rich in linear features.
- Geometric constraints are more likely to exist among linear features. This can lead to a simple and robust registration procedure.
- Linear features can be extracted with adequate accuracy across the direction of the edge.
- Linear features allow for the incorporation of areal features through the use of their boundaries. Moreover, linear features are easier to use in change detection applications than are areal features. The superiority of linear features stems from the possibility of dividing them into smaller subsets. On the other hand, breaking areal features into smaller subsets is not a trivial task.
- Terrestrial Mobile Mapping Systems (MMS) can economically provide accurate and current object space linear features in real time.
- Linear features increase the redundancy and improve the robustness and geometric strength of various photogrammetric adjustment activities.
- Point correspondence on matched linear features is not necessary, so the use of such features allows more flexibility than the use of points or areal features.

Areal primitives in photogrammetric datasets can be extracted using classification or segmentation algorithms. Such primitives include, for example, roof tops, lakes, and other homogeneous regions. Although planar patches might not be always available, especially in the case of medium-resolution satellite scenes over urban areas, they are easily identified and collected from aerial, terrestrial, and high-resolution satellite imagery. Planar patches that have well-defined edges are mostly available in large scale imagery over urban areas. This availability helps in representing such planar areas in a variety of ways. In LIDAR datasets, a patch of points falling on the same planar object can be detected and fit to a plane. Still this plane is infinite and locating the boundaries of such an object needs more processing efforts to be realized, unless the raw LIDAR points are used in its natively collected state.

2.5.2 Transformation Function

The most fundamental characteristic of any registration technique is the type of spatial transformation or mapping function needed to properly overlay the two datasets. For different data collection techniques, geometric distortions vary considerably with different factors such as the platform (i.e., terrestrial, airborne, or satellite), the sensor (i.e., frame camera, line scanner, linear or conical LIDAR systems), the total field of view, and the scanning trajectory. To overcome the problem of geometric distortions, several types of transformation functions can be considered.

In the photogrammetric datasets all primitives are measured in 2D while LIDAR primitives are represented in the native 3D LIDAR data coordinate system. Therefore, the registration transformation function should be able to register 2D imagery datasets to the 3D LIDAR point cloud. Moreover, the devised transformation functions adapt to the properties and representation of linear features and planar patches in the LIDAR (object space) and imagery datasets. Such mathematical models should not be confined only to establish a relationship between the registered datasets, but also to solve the boresighting problem of the LIDAR system and to validate and improve the internal characteristics of the implemented camera whenever possible. For background and completeness, the major transformation functions generally used for 2D-2D, 2D-3D, and 3D-3D datasets utilizing point primitives will be briefly described. The proposed 2D-3D mathematical models for straight lines and planar patches will be detailed in Chapters 3 and 4 respectively.

For 2D-2D transformation, the simplest model used is the two dimensional conformal transformation, which is also known as 2D similarity. This model can be satisfactorily used in image matching with rigid-body distortion (Brown, 1992) where the true shape is retained, Equation 2.2. Four parameters are included; two translations in x- and y-directions, one scale and one rotation.

$$\begin{bmatrix} \mathbf{x'} \\ \mathbf{y'} \end{bmatrix} = \begin{bmatrix} \mathbf{x_T} \\ \mathbf{y_T} \end{bmatrix} + \mathbf{s} \begin{bmatrix} \cos\kappa & \sin\kappa \\ -\sin\kappa & \cos\kappa \end{bmatrix} \begin{bmatrix} \mathbf{x} \\ \mathbf{y} \end{bmatrix} \tag{2.2}$$

Where (s) is the scale factor, (x_T, y_T) are the shifts in x and y directions, (κ) is the rotation angle, (x, y) are the image coordinates in the first image, and (x', y') are the corresponding image coordinates in the second image. At least two tie points are required to solve for the parameters of the 2D similarity transformation.

For 2D datasets that require more than rigid body transformation, the affine transformation is frequently used to obtain a mapping between two coordinate systems, Equation 2.3. Two extra parameters are added to those in the 2D similarity transformation, additional scale factor and non-orthogonality correction between the x and y axes. The addition of the parameters allows more distortions to be compensated for.

$$\begin{bmatrix} \mathbf{x}' \\ \mathbf{y}' \end{bmatrix} = \begin{bmatrix} \mathbf{x_T} \\ \mathbf{y_T} \end{bmatrix} + \begin{bmatrix} \mathbf{s_x} \cos\kappa & \mathbf{s_y} \sin(\kappa + \delta\kappa) \\ -\mathbf{s_x} \sin\kappa & \mathbf{s_Y} \cos(\kappa + \delta\kappa) \end{bmatrix} \begin{bmatrix} \mathbf{x} \\ \mathbf{y} \end{bmatrix} \tag{2.3}$$

Where (s_x) is the scale factor along x-axis, (s_y) is the scale factor along y-axis, ($\delta\kappa$) is the non-orthogonality angle, (x_T, y_T) are the shifts in x and y directions, (κ) is the rotation angle, (x, y) are the image coordinates in the first image, and (x', y') are the corresponding image coordinates in the input image. A minimum of three tie points are required to solve for the parameters.

The projective transformation in Equation 2.4, also known as eight-parameter transformation, is the appropriate transformation between two planes.

$$\begin{aligned} \mathbf{x}' &= \frac{\mathbf{a_0} + \mathbf{a_1 x} + \mathbf{a_2 y}}{\mathbf{a_3 x} + \mathbf{b_3 y} + \mathbf{1}} \\ \mathbf{y}' &= \frac{\mathbf{b_0} + \mathbf{b_1 x} + \mathbf{b_2 y}}{\mathbf{a_3 x} + \mathbf{b_3 y} + \mathbf{1}} \end{aligned} \tag{2.4}$$

Where (x, y) are the image coordinates in the first image and (x', y') are the corresponding image coordinates in the second image. Setting a_3 and b_3 in Equation 2.4 to zero reduces the model to the affine transformation. With eight unknown parameters, this transformation requires a minimum of four tie points.

The 3D-2D transformation is depicted by the perspective projection of frame images in which the projection rays from the object to the image space pass through the perspective center. For frame cameras, there are three models that can be used to describe the mathematical relationship between corresponding image and ground coordinates collinearity equations, Direct Linear Transformation (DLT), and projective transformation.

The collinearity equations define the relationship between image coordinates of a point and its corresponding object space coordinates. The conceptual basis of the collinearity equations is based on the fact that image point, object point, and the perspective center are collinear. The image coordinates of a point are expressed as a function of the Interior Orientation Parameters (IOP), the Exterior Orientation Parameters (EOP), and the ground coordinates of the corresponding object point, Equation 2.5 (Kraus, 1997). The IOPs are the camera characteristics required for the reconstruction of the image space bundle of rays from corresponding image points and are determined through a calibration procedure (Habib et al, 2002). The EOP describes the position and orientation of the bundle of rays with respect to the object space coordinate systems (Mikhail et al., 2001). EOPs can be directly determined through the use of GPS/INS or indirectly estimated through the use of ground control points in a bundle adjustment procedure.

$$
\begin{aligned}
\mathbf{x} &= \mathbf{x_p} - \mathbf{c}\frac{\mathbf{r_{11}} \cdot (\mathbf{X}-\mathbf{X_o}) + \mathbf{r_{21}} \cdot (\mathbf{Y}-\mathbf{Y_o}) + \mathbf{r_{31}} \cdot (\mathbf{Z}-\mathbf{Z_o})}{\mathbf{r_{13}} \cdot (\mathbf{X}-\mathbf{X_o}) + \mathbf{r_{23}} \cdot (\mathbf{Y}-\mathbf{Y_o}) + \mathbf{r_{33}} \cdot (\mathbf{Z}-\mathbf{Z_o})} \\
\mathbf{y} &= \mathbf{y_p} - \mathbf{c}\frac{\mathbf{r_{12}} \cdot (\mathbf{X}-\mathbf{X_o}) + \mathbf{r_{22}} \cdot (\mathbf{Y}-\mathbf{Y_o}) + \mathbf{r_{32}} \cdot (\mathbf{Z}-\mathbf{Z_o})}{\mathbf{r_{13}} \cdot (\mathbf{X}-\mathbf{X_o}) + \mathbf{r_{23}} \cdot (\mathbf{Y}-\mathbf{Y_o}) + \mathbf{r_{33}} \cdot (\mathbf{Z}-\mathbf{Z_o})}
\end{aligned}
\tag{2.5}
$$

where

x, y	Image point coordinates corresponding to object point (X, Y, Z).
X, Y, Z	Corresponding ground point coordinates.
x_p, y_p, c	Interior orientation parameters: calibrated principal point position and principal distance of the camera with respect to image coordinate system.

X_o, Y_o, Z_o: ω, φ, κ	Exterior orientation parameters: X_o, Y_o, and Z_o represent the position of perspective center with respect to ground coordinate system, where ω, φ and κ represent the rotation angles between the ground and image coordinate systems.
r_{11} ... r_{33}	The rotation matrix between the image and ground coordinates systems.

DLT is a linear model relating the image and ground coordinates, Equation 2.6. It is formulated using eleven parameters that include the interior and exterior orientation parameters (Abdel-Aziz and Karara, 1971). The wide spread of the DLT is due to its linear formulation of the relationship between image and object coordinates. The DLT model requires well distributed 3D object space control points to estimate the full set of its parameters. In this model, IOP and EOP are not explicitly needed.

$$\mathbf{x} = \frac{\mathbf{A_1 + A_2X + A_3Y + A_4Z}}{\mathbf{1 + A_9X + A_{10}Y + A_{11}Z}}$$
$$\mathbf{y} = \frac{\mathbf{A_5 + A_6X + A_7Y + A_8Z}}{\mathbf{1 + A_9X + A_{10}Y + A_{11}Z}} \tag{2.6}$$

where

x, y : Image point coordinates corresponding to object point coordinates (X, Y, Z)

A_1, …, A_{11} : Direct linear transformation parameters.

The third model is the projective transformation, Equation 2.7, which involves eight parameters, assumes a planar object space. Projective transformation can be used for high altitude photography over flat terrain. At least four planimetric ground control points are needed to solve for the eight parameters involved in the projective transformation. As in the case of the DLT, the IOP and EOP are not explicitly involved in the projective transformation.

$$
\begin{aligned}
\mathbf{x} &= \frac{\mathbf{A_1 + A_2X + A_3Y}}{\mathbf{1 + A_7X + A_8Y}} \\
\mathbf{y} &= \frac{\mathbf{A_4 + A_5X + A_6Y}}{\mathbf{1 + A_7X + A_8Y}}
\end{aligned}
\tag{2.7}
$$

where

x, y : Image point coordinates corresponding to object point coordinates (X, Y, Z)

$A_1, \ldots, A_8$: Projective transformation parameters.

The collinearity model used for frame imagery can be modified so as to be valid for linear array scanners (Habib and Beshah, 1998). In the case of linear array scanners, each image line is the result of a perspective projection in the CCD line direction and has its own EOP. The collinearity equations for linear array scanners are as in Equation 2.8.

$$
\begin{aligned}
\mathbf{x_t} &= \mathbf{x_p} - \mathbf{c}\frac{\mathbf{r^t_{11}\cdot(X - X^t_o) + r^t_{21}\cdot(Y - Y^t_o) + r^t_{31}\cdot(Z - Z^t_o)}}{\mathbf{r^t_{13}\cdot(X - X^t_o) + r_{23}\cdot(Y - Y^t_o) + r^t_{33}\cdot(Z - Z^t_o)}} \\
\mathbf{y_t} &= \mathbf{y_p} - \mathbf{c}\frac{\mathbf{r^t_{12}\cdot(X - X^t_o) + r^t_{22}\cdot(Y - Y^t_o) + r^t_{32}\cdot(Z - Z^t_o)}}{\mathbf{r^t_{13}\cdot(X - X^t_o) + r^t_{23}\cdot(Y - Y^t_o) + r^t_{33}\cdot(Z - Z^t_o)}}
\end{aligned}
\tag{2.8}
$$

where

x_t, y_t: Image point coordinates corresponding to object point (X, Y, Z) at time t

X, Y, Z: Corresponding ground point coordinates

x_p, y_p, c: Interior orientation parameters (calibrated principal point position and principal distance of the camera with respect to image coordinate system)

$r^t_{11}, r^t_{22}, \ldots, r^t_{33}$: Elements of rotation matrix R^t, which are function of ω^t, φ^t and κ^t at time t

X^t_o, Y^t_o, Z^t_o: The position of the perspective center at time of capturing the scan line under consideration.

An important member in the 3D-3D transformation function family is the 3D similarity transformation (a conformal transformation). The importance of this function, in this context, stems from its use in the photogrammetric absolute orientation procedure for model orientation purposes. As the name indicates, this type of transformation preserves the geometric similarity where the angles are preserved and all distances are changed in the same ratio, called the scale factor. In other words this transformation is described as a rigid-body transformation between the reference frames of datasets where the true shape is retained. Such a transformation involves seven-parameters which are one scale, three translations, and three rotations. Equation 2.9 represents the mathematical form of the 3D similarity transformation in the absence of systematic errors within the two systems.

$$\begin{bmatrix} \mathbf{X_A} \\ \mathbf{Y_A} \\ \mathbf{Z_A} \end{bmatrix} = \begin{bmatrix} \mathbf{X_T} \\ \mathbf{Y_T} \\ \mathbf{Z_T} \end{bmatrix} + \mathbf{S}\,\mathbf{R}(\Omega, \Phi, \mathrm{K}) \begin{bmatrix} \mathbf{X_a} \\ \mathbf{Y_a} \\ \mathbf{Z_a} \end{bmatrix} \tag{2.9}$$

where:

S	is the scale factor; the same in all directions,
$(X_T\ Y_T\ Z_T)^T$	is the translation vector between the origins of the coordinate systems,
$R_{(\Omega,\Phi,K)}$	is the 3D orthogonal rotation matrix between the two coordinate systems,
$(X_a\ Y_a\ Z_a)^T$	are the coordinates of one point from one dataset, and
$(X_A\ Y_A\ Z_A)^T$	are the coordinates of the corresponding point in the other dataset.

2.5.3 Similarity Measure

The role of the similarity measure is to introduce the necessary constraints for ensuring the coincidence of conjugate photogrammetric and LIDAR primitives after applying the proper transformation function. The formulation of the similarity measure depends on the selected registration primitives and their respective attributes (i.e., representation scheme). In addition, the similarity measure depends on the utilized methodology for incorporating the LIDAR and photogrammetric data in the registration process. Again, similarity criteria must be devised for linear features-based and areal-based co-registration methodologies.

A previous survey of registration techniques (Fonseca and Manjunath, 1996) reviewed registration techniques developed for many different types of applications and data. An earlier survey by Brown (1992) was far more wide-ranging and compared numerous different applications of image registration, including remote sensing, computer vision and medical imaging. The following survey outlines relevant research attempts in registering 3D datasets.

Conventionally, surface-to-surface registration and comparison have been achieved by interpolating both datasets into a uniform grid. After interpolating both datasets, Ebner and Ohlhof (1994) and Kilian et al. (1996) reduced the comparison to estimating the necessary shifts by analyzing the elevation differences at corresponding grid posts. Their approach used point primitives with 2D similarity or affine transformation functions. The similarity measure was to minimize the differences in the Z direction. This approach has several limitations. Firstly, the interpolation to a grid will introduce errors, especially when dealing with captured surfaces over urban areas. Secondly, minimizing the differences between surfaces along the Z direction is only valid when dealing with horizontal planar surfaces (Habib and Schenk 1999).

Postolov et al. (1999) presented another approach, which works on the original scattered data without prior interpolation. However, the implementation procedure involves an interpolation of one surface at the location of conjugate points on the other surface. Additionally, the registration is based on minimizing the differences between the two surfaces along the Z direction. This approach also has the disadvantage of interpolating the original surface for extracting point primitives at certain locations. In addition to that, minimizing the differences between surfaces along the Z direction is only valid when dealing with horizontal planar surfaces (Habib and Schenk 1999).

Schenk (1999a) and Habib and Schenk (1999) introduced an alternative approach for matching LIDAR and photogrammetric surfaces. In the proposed similarity measure the distances between points of one surface along surface normals to locally interpolated patches of the other surface are minimized, Figure 2.9. Habib et al. (2001) implemented this methodology within a comprehensive automatic registration procedure. This procedure is based on processing the photogrammetric data to produce object-space planar patches. A common problem in the above techniques is that they are 3D to 3D registration methodologies; therefore the photogrammetric model should be established first. However, 2D to 3D registration is needed to relate 2D imagery to 3D LIDAR data.

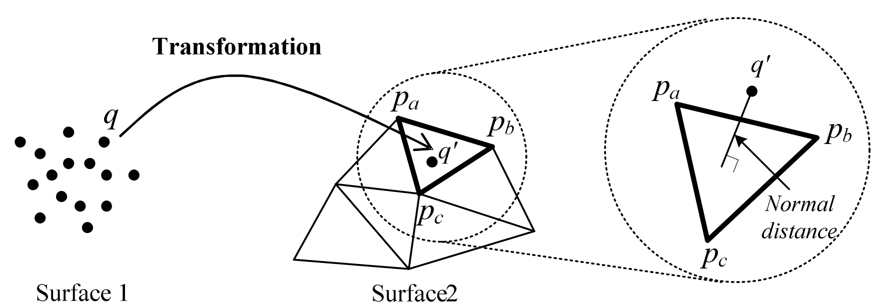

Figure 2.9. Similarity measure between two surfaces after transformation where the normal distance is minimized

Jaw and Wu (2006), suggested a framework that utilizes control patches stored in utility databases for photogrammetric single photo resection. The control patch is first back projected on the image using approximate exterior orientation parameters. A combined cross correlation and least squares matching is then used to sequentially locate the projected patch on all levels of the image pyramid. The EOPs are refined at each level until no further refinement is achieved. The disadvantage of this method is the extensive amount of information needed to be available and stored about control patches. Also, good first estimate for the EOPs seems necessary, a luxury that might not be always available. Another limitation might arise is the possibility of not matching the minimum number of patches necessary for single photo resection, three control patches in this case.

Further research attempts tried to exploit the complementary properties between photogrammetric and LIDAR systems for building extraction purposes (Nakagawa et al. 2002, Rottensteiner and Jansa 2002, Vosselman 2002, Huber et al. 2003, Chen et al. 2004, Rottensteiner et al. 2004, Savopol and Armenakis 2004). These studies start mainly by feature extraction through the segmentation of individual datasets. This is followed by a multi-step perceptual organization and object recognition through two-way augmentation of synergic features of the LIDAR and photogrammetric datasets. The drawback of these approaches is that raw measurements from both datasets are not visible during the implementation of the mathematical models. The segmentation and grouping of features can carry over undetected blunders and other inaccuracies to the final fusion results. Also, some studies reported sensitivity to the type and distribution of buildings in the object space. Furthermore, the objective of these methods is limited to building extraction applications.

In summary, new co-registration methodologies utilizing primitives that can be robustly represented and extracted in both LIDAR and photogrammetric datasets must be developed. Moreover, proper mathematical models and similarity measures must also be formulated to exploit the complementary nature between both datasets.

CHAPTER 3

CO-REGISTRATION METHODOLOGY USING LINEAR FEATURES

3.1 Introduction

The discussions in Chapter 2 laid the grounds for exploiting straight-lines and planar patches as the registration features for photogrammetric and LIDAR dataset integration. This chapter introduces two methodologies for the co-registration of photogrammetric and LIDAR surfaces relative to a common reference frame by means of linear features. The first methodology will directly incorporate the LIDAR lines in the photogrammetric bundle adjustment to establish the datum. The other methodology is based on preliminary and independent processing of the LIDAR and photogrammetric data, where a photogrammetric model is built relative to an arbitrary coordinate system. Then, conjugate LIDAR and photogrammetric lines are utilized in an absolute orientation of the photogrammetric model to the LIDAR reference frame.

Section 3.2 starts with the rationale behind adopting straight lines as one option for the registration primitives. In addition, it addresses the representation and extraction of linear features from the photogrammetric and LIDAR datasets. The mathematical models and similarity measures in the suggested registration methodologies are detailed in Sections 3.3 and 3.4.

3.2 Straight Lines as the Registration Primitives

As mentioned previously in Section 2.5.1, a number of advantages have led to decision on straight-line segments as an appropriate type of registration primitives for the co-registration between LIDAR and photogrammetric datasets. To devise a practical scheme by which straight lines can be extracted from the photogrammetric and LIDAR datasets, the representation of such straight lines in the object and image space must be clearly stated and justified. These issues are discussed in the following subsections.

3.2.1 Photogrammetric Straight-Lines

The representation scheme of 3D straight lines in the object and image space is central to the methodology for producing such features from photogrammetric datasets. Representing object space straight lines using two points along the line is the most convenient representation from a photogrammetric point of view since it yields well-defined line segments, Figure 3.1. (Habib et al., 2002).

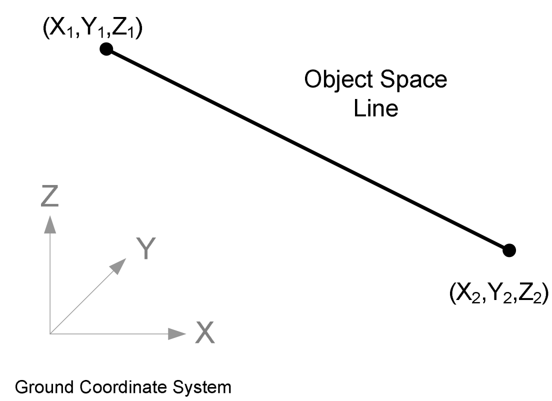

Figure 3.1. Object space lines represented by its 3D end points

On the other hand, image space lines will be represented by a sequence of 2D coordinates of image points along the feature, Figure 3.1.3.2. This is an appealing representation since it can handle image space linear features in the presence of distortions as they will cause deviations from straightness. Furthermore, it will allow for the inclusion of linear features in scenes captured by line cameras since perturbations in the flight trajectory would lead also to deviations from straightness in image space linear features corresponding to object space straight lines (Habib et al., 2002). It is important to note that image space representation of lines is different in the 1-step and 2-step procedures. In the following, the representation and extraction of photogrammetric lines in both procedures are explained.

<u>2-Step Procedure:</u>

In the 2-step procedure, a 3D photogrammetric model involving tie lines is first constructed using arbitrary datum. For this purpose, tie straight lines appearing in a group of overlapping images are represented by two points which are used to define the corresponding 3D model space line through the collinearity model, and a series of intermediate points. See Habib et al. (2002) and Habib and Morgan (2003b) for more details on bundle adjustment using straight line features.

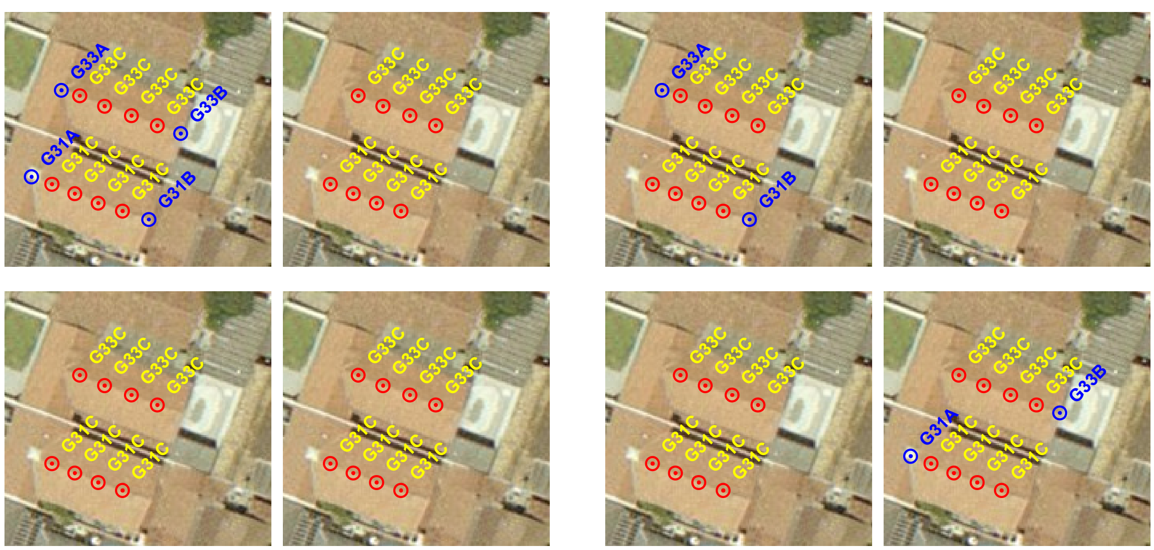

Points defining the line in the object space

Intermediate points

(a)

(b)

Figure 3.2. End points of tie lines are measured in one image (a) or in two images (b) while the intermediate points are measured in all images within which the line appears

The extraction of image lines starts by identifying two points in one (Figure 3.2a) or two images (Figure 3.2b) along the line under consideration. One should note that these points need not be identifiable or even visible in other images. Intermediate points along the line are measured in all the overlapping images. Similar to the end points, the intermediate points need not be conjugate, Figure 3.2. After collecting all required image lines and constructing the photogrammetric model, the 3D model lines, each represented by two 3D points, are now ready to be used in the 2-step co-registration procedure as will be shown in Section 3.4.

1-Step Procedure:

In the 1-step method, LIDAR lines are directly involved in the photogrammetric bundle adjustment procedure. In this case the 3D model constructed in the 2-step method is not needed. The photogrammetric lines required for the co-registration with LIDAR lines are represented on the image level as a series of intermediate points. The extraction of image space lines is achieved by only measuring the intermediate points in all images in which the line appears, Figure 3.3.

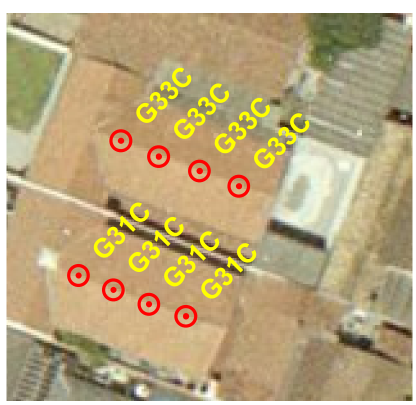

Figure 3.3. Image space control lines measured as a sequence of 2D intermediate points

3.2.2 LIDAR Straight Lines

In addition to the straight-lines represented and extracted from the photogrammetric dataset, a corresponding set of LIDAR straight lines have to be extracted as well to be used in the registration procedure. LIDAR lines will be used in two ways; firstly, in the 2-step procedure will be used as the source of control to align the photogrammetric model, Figure 3.4. Secondly, in the 1-step procedure, it will be used as the source of control in the photogrammetric bundle adjustment. Since the datum for LIDAR dataset is directly established by the GPS system installed onboard the sensor platform, LIDAR lines will be represented by two 3D points as shown previously in Figure 3.1.

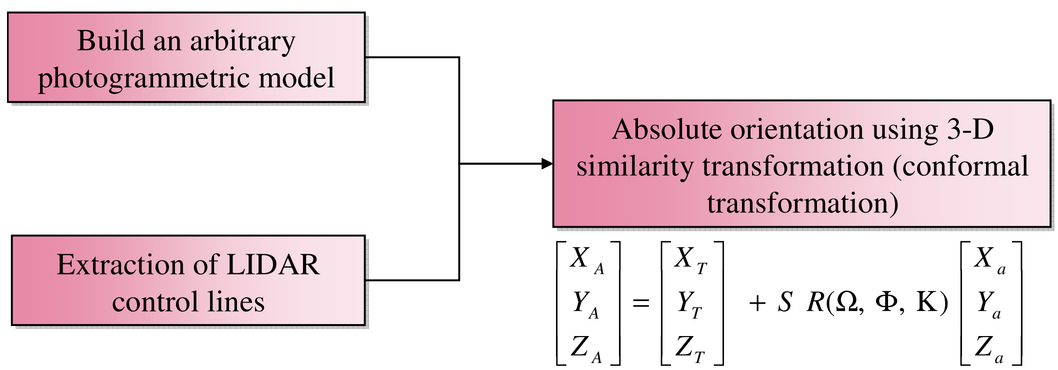

Figure 3.4. LIDAR lines are used as a source of control to align the photogrammetric model in the 2-step procedure

There are different approaches by which LIDAR lines can be collected. Two approaches were investigated, which are summarized as follows:

- In the first approach, suspected planar patches in the LIDAR dataset are manually identified with the help of corresponding optical imagery, Figure 3.5. The points comprising the patches are then checked using a least-squares adjustment procedure to determine whether they are planar or not, and to remove blunders. Finally, planar patches are fit to planes and then neighboring planes with different orientation are intersected to determine the end points along object space discontinuities between the patches under consideration.

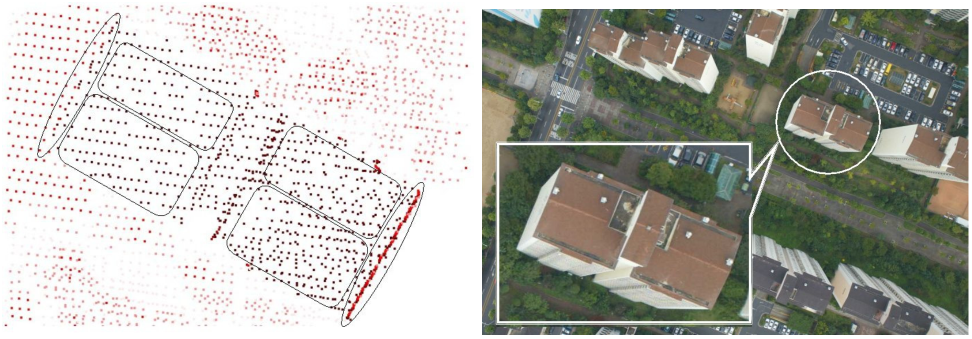

(a) (b)

Figure 3.5. Manually identified planar patches in the LIDAR data (a) guided by the corresponding optical image (b) in aerial datasets

- In the second approach, where the goal is to simplify the extraction process, intensity and range data recorded by the LIDAR system are utilized for direct measurement of linear features. Raw range and intensity data are first interpolated to a uniform grid using identical interpolation methods and parameters. Linear features previously extracted from photogrammetry are then identified on the intensity image from which the planimetric coordinates of line ends are measured while observing height readings from the range image, Figure 3.6.

Many factors, including the availability of intensity data, can play a role in the choice of the extraction method. Automatic extraction of straight lines is beyond the objectives of this study and will be suggested for future work. The main objective is focused on dataset registration using straight lines, not the extraction method.

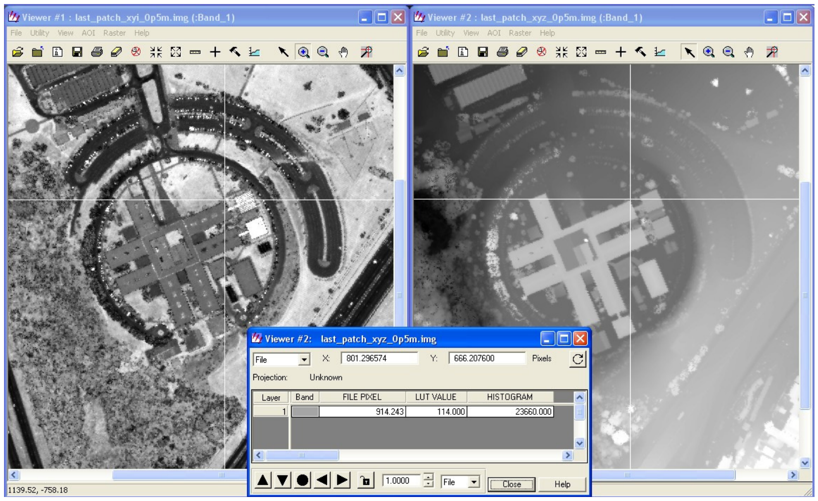

(a) (b)

Figure 3.6. Manually measuring planimetric coordinates from intensity image (a) and height value from range image (b).

After all straight line primitives from both datasets are extracted, the next step is to select a proper transformation function that can faithfully represent the transformation between the reference frames of involved datasets.

As for the processing methodology, this research implements two techniques for incorporating the linear features in the registration procedure. The first technique will directly incorporate the LIDAR lines in the photogrammetric bundle adjustment to establish the datum. The other technique is based on preliminary and independent processing of the LIDAR and photogrammetric data, where a photogrammetric model is built relative to an arbitrary coordinate system. Then, conjugate LIDAR and photogrammetric primitives are utilized in an absolute orientation of the photogrammetric model to the LIDAR reference frame. The following subsections discuss the involved mathematical models in the two processing techniques.

3.3 Mathematical Model: Direct incorporation of LIDAR features in the photogrammetric triangulation; One-Step Registration

In this methodology, the photogrammetric dataset will be aligned to the LIDAR reference frame through direct incorporation of LIDAR lines as the source of control in the photogrammetric bundle adjustment. In this procedure LIDAR lines are conceptually projected onto the image space, Figure 3.7. The similarity measure is implicitly described by the coincidence of projected LIDAR line with the image line.

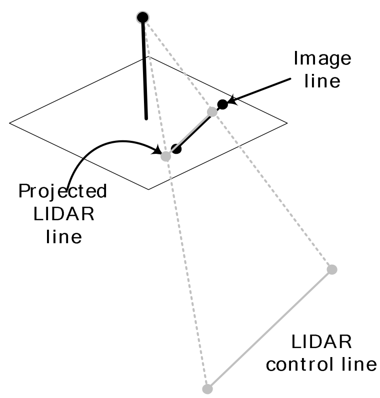

Figure 3.7. Similarity measure (coplanarity constraint) between photogrammetric and LIDAR features after transformation

The implementation of the transformation function and similarity measure are applied simultaneously for each intermediate point measured on the imagery in the form of a coplanarity condition as shown in Figure 3.8. This constraint indicates that the vector from the perspective centre to any intermediate image point along the line is contained within the plane defined by the perspective centre of that image and the two points defining the LIDAR line. In other words, for a given intermediate point, k'', the points $\{(\mathbf{X_1},\mathbf{Y_1},\mathbf{Z_1}),\ (\mathbf{X_2},\mathbf{Y_2},\mathbf{Z_2}),\ (\mathbf{X''_O},\mathbf{Y''_O},\mathbf{Z''_O})$, and $(\mathbf{x_{k''}},\mathbf{y_{k''}},\mathbf{0})\}$ are coplanar. This coplanarity constraint is mathematically represented in Equation 3.1.

$$\left(\vec{\mathbf{V}}_1 \times \vec{\mathbf{V}}_2\right) \bullet \vec{\mathbf{V}}_3 = \mathbf{0} \tag{3.1}$$

Where

$\vec{\mathbf{V}}_1$ is the vector connecting the perspective centre to the first end point along the LIDAR line,

$\vec{\mathbf{V}}_2$ is the vector connecting the perspective centre to the second end point along the LIDAR line, and

$\vec{\mathbf{V}}_3$ is the vector connecting the perspective centre to an intermediate point along the corresponding image line.

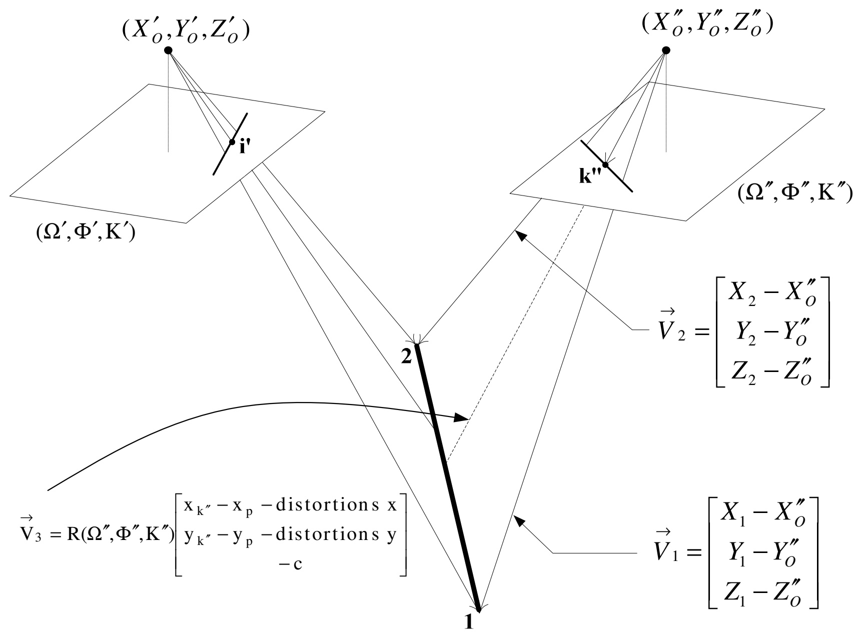

Figure 3.8. Perspective transformation between image and LIDAR control straight lines and the coplanarity constraint for intermediate points along the line

One should note that this condition assumes that LIDAR data is free from any systematic errors which might affect the straightness of the line. Recovering existing LIDAR systematic errors is not a trivial task since LIDAR lines are processed through the segmentation and intersection of the original LIDAR data or through interpolated range and intensity images. However, photogrammetric systematic errors can be rectified using the coplanarity constraint as shown in Equation 3.1 where vector $\mathbf{V_3}$ in Figure 3.8 is explicitly expressed as a function of the sensor parameters. This explicit representation of the imaging sensor parameters can be utilized for its calibration within the bundle adjustment procedure (i.e., bundle adjustment with self-calibration). In general, the presence of uncompensated systematic errors, either in the photogrammetric or LIDAR data, will show as a poor quality of fit between the involved datasets following the registration procedure.

3.4 Mathematical Model: LIDAR features for the absolute orientation of an arbitrarily established photogrammetric model; Two-Step Registration

In this approach, the photogrammetric and LIDAR datasets are separately processed to generate the linear features from each set. It has to be mentioned that the datum for the photogrammetric bundle adjustments will be established by choosing an arbitrary reference frame. For example, seven of the nine coordinates of three well-distributed tie points can be arbitrarily fixed. Afterwards, conjugate lines from photogrammetry and LIDAR will be manipulated through a similarity measure to determine the 7 parameters of the conformal transformation function relating the photogrammetric coordinate system to the LIDAR reference frame.

The mathematical model for incorporating tie lines in the photogrammetric bundle adjustment is detailed in Habib et al. (2002) and Habib and Morgan (2003b), but repeated here for completeness.

Generally, for the purpose of constructing a photogrammetric model using tie straight lines appearing in a group of overlapping images, two points are identified in one (Figure

3.2a) or two images (Figure 3.2b) along the line under consideration. These points will be used to define the corresponding object space line segment. One should note that these points need not be identifiable or even visible in other images. Intermediate points along the line are measured in all the overlapping images. Similar to the end points, the intermediate points need not be conjugate, Figure 3.2.

For the end points, the relationship between the measured image coordinates $\{(x_1, y_1), (x_2, y_2)\}$ and the corresponding ground coordinates $\{(X_1, Y_1, Z_1), (X_2, Y_2, Z_2)\}$ is established through the collinearity equations, see Figure 3.9. Only four collinearity equations will be written for each line, two equations for each end point. As explained in Section 3.3, the incorporation of intermediate points into the adjustment procedure is achieved through a mathematical constraint. The underlying principle in this constraint is that the vector from the perspective centre to any intermediate image point along the line is contained within a plane. This plane is defined by the perspective centre of that image and the two points defining the straight line in the object space, Figure 3.9. This constraint is mathematically described in Equation 3.2.

$$\left(\vec{\mathbf{V}}_1 \times \vec{\mathbf{V}}_2\right) \bullet \vec{\mathbf{V}}_3 = \mathbf{0} \tag{3.2}$$

In the above equation, $\vec{\mathbf{V}}_1$ is the vector connecting the perspective centre to the first end point along the model space line, $\vec{\mathbf{V}}_2$ is the vector connecting the perspective centre to the second end point along the model space line, and $\vec{\mathbf{V}}_3$ is the vector connecting the perspective centre to an intermediate point along the corresponding image line. It should be noted that the three vectors should be represented relative to a common coordinate system (e.g., the ground coordinate system). The constraint in Equation 3.2 incorporates the image coordinates of the intermediate point, the Exterior Orientation Parameters (EOP), the Interior Orientation Parameters (IOP) including distortion parameters, and the ground coordinates of the points defining the object space line. Such a constraint does not introduce any new parameters and can be written for all intermediate points along the line in the imagery. The number of constraints is equal to the number of intermediate points measured along the image line.

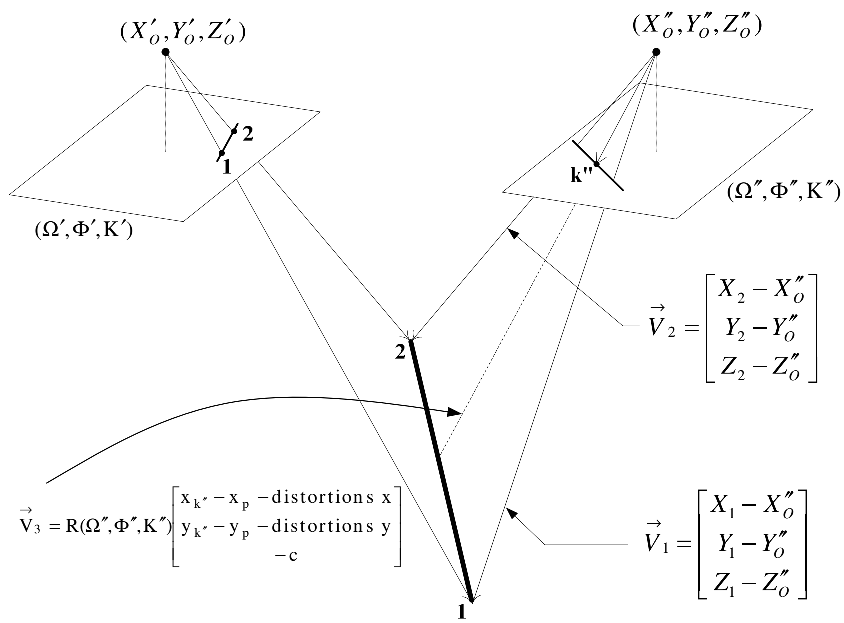

Figure 3.9. Perspective transformation between image and model space straight lines and the coplanarity constraint for intermediate points along the line

3.4.1 Transformation Function

In this methodology, 3D similarity transformation is used to align the photogrammetric model relative to the LIDAR coordinate system, Figure 3.10. Equation 3.3 represents the mathematical form of the 3D similarity transformation in the absence of systematic errors within the two systems.

$$\begin{bmatrix} \mathbf{X_A} \\ \mathbf{Y_A} \\ \mathbf{Z_A} \end{bmatrix} = \begin{bmatrix} \mathbf{X_T} \\ \mathbf{Y_T} \\ \mathbf{Z_T} \end{bmatrix} + \mathbf{S}\,\mathbf{R}(\Omega, \Phi, \mathrm{K}) \begin{bmatrix} \mathbf{X_a} \\ \mathbf{Y_a} \\ \mathbf{Z_a} \end{bmatrix} \tag{3.3}$$

where:

S is the scale factor,

$(X_T\ Y_T\ Z_T)^T$ is the translation vector between the origins of the photogrammetric and LIDAR coordinate systems,

$R_{(\Omega,\Phi,K)}$ is the 3D orthogonal rotation matrix between the two coordinate systems,

$(X_a\ Y_a\ Z_a)^T$ are the photogrammetric point coordinates, and

$(X_A\ Y_A\ Z_A)^T$ are the coordinates of the corresponding point relative to the LIDAR reference frame.

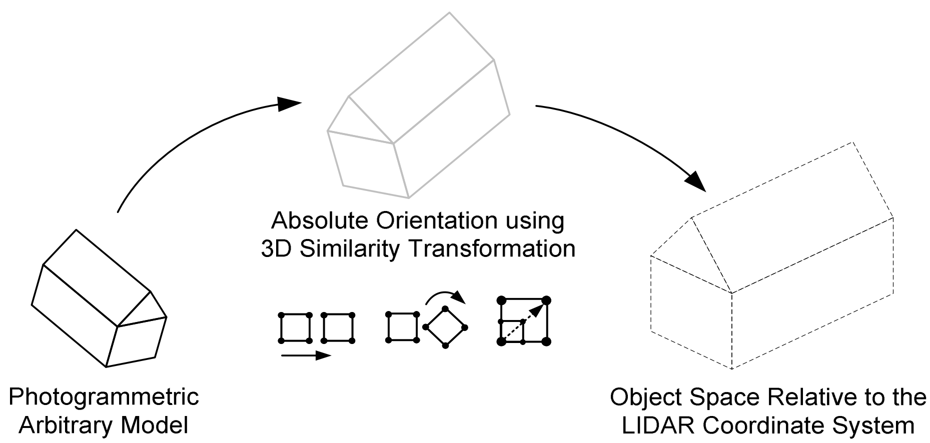

Figure 3.10. 3D similarity transformation where the model undergoes translation, rotation, and scale

The absolute orientation using conjugate points is a well known procedure. However, there is no established procedure for estimating the 3D similarity transformation parameters while using corresponding linear features represented by their end points, which might not be conjugate. Determining the parameters of the registration transformation function will be carried out using a similarity measure that involves the attributes of linear features as discussed in the next subsection.

3.4.2 Similarity Measure

The role of the similarity measure is to describe the necessary constraints for ensuring the correspondence of conjugate primitives in overlapping surfaces, photogrammetric model lines and LIDAR lines in this methodology. The derivation of the similarity measure is based on the fact that the photogrammetric line segment should coincide with the corresponding LIDAR segment after applying the registration transformation function, Figure 3.11.

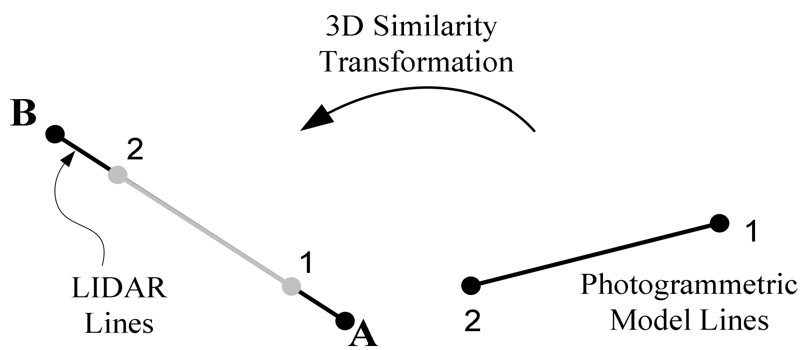

Figure 3.11. Similarity measure between photogrammetric and LIDAR linear features

As mentioned before in Subsection 3.2.1, representing object line segments using two points along the line is the most convenient representation alternative. In this regard, it is worth mentioning that the end points, representing corresponding photogrammetric model and LIDAR line segments, need not be conjugate.

Referring to Figure 3.11, the points 1 and 2 describing the line segment from the photogrammetric model undergo a 3D similarity transformation onto the LIDAR line segment represented by points A and B. The objective here is to introduce the necessary constraints to describe the fact that the model segment (1,2) coincides with the object segment (A,B) after applying the transformation. For these photogrammetric points (1,2), the constraint equations can be written as in Equations 3.3 and 3.4.

For the photogrammetric point (1), this constraint can be mathematically described as in Equation 3.4.

$$\begin{bmatrix} \mathbf{X_T} \\ \mathbf{Y_T} \\ \mathbf{Z_T} \end{bmatrix} + \mathbf{S}\,\mathbf{R}_{(\Omega,\,\Phi,\,K)} \begin{bmatrix} \mathbf{X_1} \\ \mathbf{Y_1} \\ \mathbf{Z_1} \end{bmatrix} = \begin{bmatrix} \mathbf{X_A} \\ \mathbf{Y_A} \\ \mathbf{Z_A} \end{bmatrix} + \lambda_1 \begin{bmatrix} \mathbf{X_B} - \mathbf{X_A} \\ \mathbf{Y_B} - \mathbf{Y_A} \\ \mathbf{Z_B} - \mathbf{Z_A} \end{bmatrix} \tag{3.4}$$

Where $(X_T\ Y_T\ Z_T)^T$ is the translation vector between the origins of the imagery and LIDAR scanner coordinate systems, R is the 3D orthogonal rotation matrix, and S and λ_1 are scale factors. Equation 3.5 shows the constraint for point (2)

$$\begin{bmatrix} \mathbf{X_T} \\ \mathbf{Y_T} \\ \mathbf{Z_T} \end{bmatrix} + \mathbf{S}\,\mathbf{R}_{(\Omega,\,\Phi,\,K)} \begin{bmatrix} \mathbf{X_2} \\ \mathbf{Y_2} \\ \mathbf{Z_2} \end{bmatrix} = \begin{bmatrix} \mathbf{X_A} \\ \mathbf{Y_A} \\ \mathbf{Z_A} \end{bmatrix} + \lambda_2 \begin{bmatrix} \mathbf{X_B} - \mathbf{X_A} \\ \mathbf{Y_B} - \mathbf{Y_A} \\ \mathbf{Z_B} - \mathbf{Z_A} \end{bmatrix} \tag{3.5}$$

Subtracting Equation 3.5 from 3.4 yields

$$(\lambda_2 - \lambda_1) \begin{bmatrix} \mathbf{X_B} - \mathbf{X_A} \\ \mathbf{Y_B} - \mathbf{Y_A} \\ \mathbf{Z_B} - \mathbf{Z_A} \end{bmatrix} = \mathbf{S}\,\mathbf{R}_{(\Omega,\,\Phi,\,K)} \begin{bmatrix} \mathbf{X_2} - \mathbf{X_1} \\ \mathbf{Y_2} - \mathbf{Y_1} \\ \mathbf{Z_2} - \mathbf{Z_1} \end{bmatrix} \tag{3.6}$$

Substituting λ for S/(λ2 - λ1), Equation 3.6 can be rewritten as follows:

$$\begin{bmatrix} \mathbf{X_B} - \mathbf{X_A} \\ \mathbf{Y_B} - \mathbf{Y_A} \\ \mathbf{Z_B} - \mathbf{Z_A} \end{bmatrix} = \lambda\,\mathbf{R}_{(\Omega,\,\Phi,\,K)} \begin{bmatrix} \mathbf{X_2} - \mathbf{X_1} \\ \mathbf{Y_2} - \mathbf{Y_1} \\ \mathbf{Z_2} - \mathbf{Z_1} \end{bmatrix} \tag{3.7}$$

Equation 3.7 emphasizes the concept that photogrammetric line segments should be parallel to the LIDAR line segments after applying the rotation matrix. To recover the elements of the rotation matrix, Equation 3.7 is further manipulated and rearranged by dividing the first and second rows by the third to eliminate λ resulting in Equations 3.8.

$$\begin{aligned}
\frac{(\mathbf{X_B} - \mathbf{X_A})}{(\mathbf{Z_B} - \mathbf{Z_A})} &= \frac{\mathbf{R_{11}}\ (\mathbf{X_2} - \mathbf{X_1}) + \mathbf{R_{12}}\ (\mathbf{Y_2} - \mathbf{Y_1}) + \mathbf{R_{13}}\ (\mathbf{Z_2} - \mathbf{Z_1})}{\mathbf{R_{31}}\ (\mathbf{X_2} - \mathbf{X_1}) + \mathbf{R_{32}}\ (\mathbf{Y_2} - \mathbf{Y_1}) + \mathbf{R_{33}}\ (\mathbf{Z_2} - \mathbf{Z_1})} \\
\frac{(\mathbf{Y_B} - \mathbf{Y_A})}{(\mathbf{Z_B} - \mathbf{Z_A})} &= \frac{\mathbf{R_{21}}\ (\mathbf{X_2} - \mathbf{X_1}) + \mathbf{R_{22}}\ (\mathbf{Y_2} - \mathbf{Y_1}) + \mathbf{R_{23}}\ (\mathbf{Z_2} - \mathbf{Z_1})}{\mathbf{R_{31}}\ (\mathbf{X_2} - \mathbf{X_1}) + \mathbf{R_{32}}\ (\mathbf{Y_2} - \mathbf{Y_1}) + \mathbf{R_{33}}\ (\mathbf{Z_2} - \mathbf{Z_1})}
\end{aligned} \tag{3.8}$$

A pair of conjugate line segments yields two equations, which contribute to the estimation of two rotation angles, the azimuth and pitch, along the line. On the other hand, the roll angle across the line cannot be estimated, Figure 3.12(a). Hence a minimum of two non-parallel lines is needed to recover the three elements of the rotation matrix (Ω, Φ, K), Figure 3.12(b).

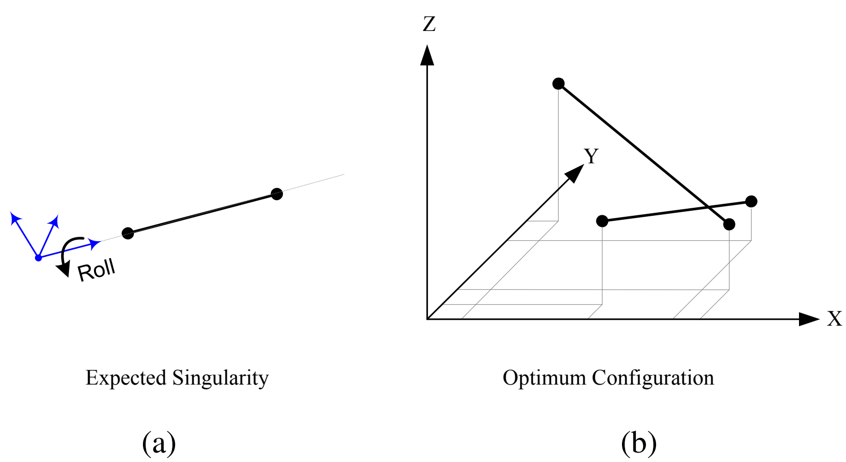

Figure 3.12. Singular (a) and optimum (b) configurations to recover rotation angles

Now, we need to investigate how to recover the scale factor and the shift components. We start by applying the rotation matrix to the coordinates of the points defining the model line.

Again, applying the constraint to photogrammetric point (1) yields Equation 3.9.

$$\begin{bmatrix} \mathbf{X_T} \\ \mathbf{Y_T} \\ \mathbf{Z_T} \end{bmatrix} + \mathbf{S} \begin{bmatrix} \mathbf{x_1} \\ \mathbf{y_1} \\ \mathbf{z_1} \end{bmatrix} = \begin{bmatrix} \mathbf{X_A} \\ \mathbf{Y_A} \\ \mathbf{Z_A} \end{bmatrix} + \lambda_1 \begin{bmatrix} \mathbf{X_B} - \mathbf{X_A} \\ \mathbf{Y_B} - \mathbf{Y_A} \\ \mathbf{Z_B} - \mathbf{Z_A} \end{bmatrix} \tag{3.9}$$

where,

$[\mathbf{x_1} \quad \mathbf{y_1} \quad \mathbf{z_1}]^T = \mathbf{R}_{(\Omega,\ \Phi,\ K)} [\mathbf{X_1} \quad \mathbf{Y_1} \quad \mathbf{Z_1}]^T$

Rearranging the terms of Equation 3.9, we get

$$\lambda_1 \begin{bmatrix} \mathbf{X_B} - \mathbf{X_A} \\ \mathbf{Y_B} - \mathbf{Y_A} \\ \mathbf{Z_B} - \mathbf{Z_A} \end{bmatrix} = \begin{bmatrix} \mathbf{X_T} + \mathbf{S}\ \mathbf{x_1} - \mathbf{X_A} \\ \mathbf{Y_T} + \mathbf{S}\ \mathbf{y_1} - \mathbf{Y_A} \\ \mathbf{Z_T} + \mathbf{S}\ \mathbf{z_1} - \mathbf{Z_A} \end{bmatrix} \tag{3.10}$$

In Equation 3.10, eliminate λ_1 by dividing the first and second rows by the third to get:

$$\begin{aligned} \frac{(\mathbf{X_B} - \mathbf{X_A})}{(\mathbf{Z_B} - \mathbf{Z_A})} &= \frac{(\mathbf{X_T} + \mathbf{S}\ \mathbf{x_1} - \mathbf{X_A})}{(\mathbf{Z_T} + \mathbf{S}\ \mathbf{z_1} - \mathbf{Z_A})} \\ \frac{(\mathbf{Y_B} - \mathbf{Y_A})}{(\mathbf{Z_B} - \mathbf{Z_A})} &= \frac{(\mathbf{Y_T} + \mathbf{S}\ \mathbf{y_1} - \mathbf{Y_A})}{(\mathbf{Z_T} + \mathbf{S}\ \mathbf{z_1} - \mathbf{Z_A})} \end{aligned} \tag{3.11}$$

Applying the same procedure for point 2, a similar result is reached, Equations 3.12

$$\begin{aligned} \frac{(\mathbf{X_B} - \mathbf{X_A})}{(\mathbf{Z_B} - \mathbf{Z_A})} &= \frac{(\mathbf{X_T} + \mathbf{S}\ \mathbf{x_2} - \mathbf{X_A})}{(\mathbf{Z_T} + \mathbf{S}\ \mathbf{z_2} - \mathbf{Z_A})} \\ \frac{(\mathbf{Y_B} - \mathbf{Y_A})}{(\mathbf{Z_B} - \mathbf{Z_A})} &= \frac{(\mathbf{Y_T} + \mathbf{S}\ \mathbf{y_2} - \mathbf{Y_A})}{(\mathbf{Z_T} + \mathbf{S}\ \mathbf{z_2} - \mathbf{Z_A})} \end{aligned} \tag{3.12}$$

Dividing Equations 3.11 of point (1) by Equations 3.12 of point (2) and rearranging the terms, we can write the result in Equations 3.13.

$$\begin{aligned} \frac{(\mathbf{X_T} + \mathbf{S}\ \mathbf{x_1} - \mathbf{X_A})}{(\mathbf{Z_T} + \mathbf{S}\ \mathbf{z_1} - \mathbf{Z_A})} &= \frac{(\mathbf{X_T} + \mathbf{S}\ \mathbf{x_2} - \mathbf{X_A})}{(\mathbf{Z_T} + \mathbf{S}\ \mathbf{z_2} - \mathbf{Z_A})} \\ \frac{(\mathbf{Y_T} + \mathbf{S}\ \mathbf{y_1} - \mathbf{Y_A})}{(\mathbf{Z_T} + \mathbf{S}\ \mathbf{z_1} - \mathbf{Z_A})} &= \frac{(\mathbf{Y_T} + \mathbf{S}\ \mathbf{y_2} - \mathbf{Y_A})}{(\mathbf{Z_T} + \mathbf{S}\ \mathbf{z_2} - \mathbf{Z_A})} \end{aligned} \tag{3.13}$$

Two pairs of intersecting line segments yield four equations. The shift components can be estimated (using the intersection points) but the scale factor cannot be recovered,

Figure 3.13(a). As a result at least two non-coplanar line segments are needed to recover these parameters Figure 3.13(b).

In summary, a minimum of two non-coplanar line segments is needed to recover the seven elements of the 3D similarity transformation. It is important to note that the correspondence between linear features in overlapping surfaces is established manually.

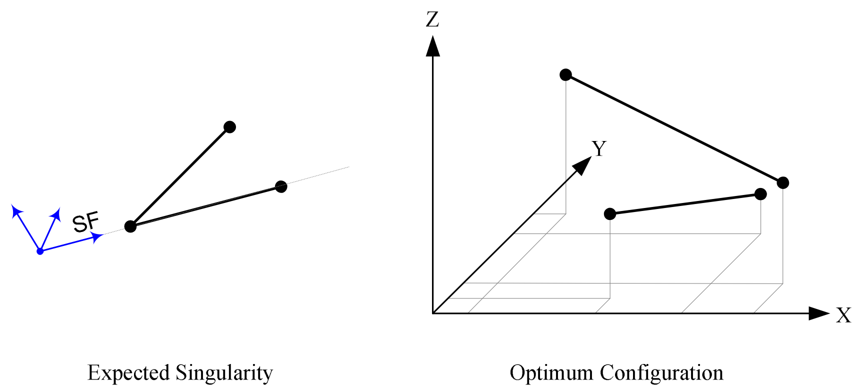

(a) (b)

Figure 3.13. Singular (a) and optimum (b) configurations to recover scale and shift components

In general, the first approach, where LIDAR lines are directly incorporated in the photogrammetric triangulation (2D-3D transformation), can be considered restrictive since it is not general enough to allow for any surface-to-surface (3D-3D transformation) registration exercise regardless of their origin. For example, it cannot be used to establish the registration between two overlapping LIDAR surfaces. Moreover, incorporating the LIDAR features within the photogrammetric adjustment will not allow for the inspection of the compatibility and discrepancy between the involved surfaces. Such discrepancy might be expected due to improper system calibration, measurement blunders, and physical changes in the object space.

At this point, the components of the registration methodology have been addressed. Straight line segments are chosen as the registration primitives, along with a 3D similarity as the registration transformation function. Also, the similarity measure is formulated based on the selected primitives and transformation function. The quality of fit, represented by the resulting variance component from the similarity measure, as well as the residuals and discrepancy between conjugate features, will be used to validate and check the quality of the calibration parameters associated with the imaging and ranging systems.

In the Experiments and Results chapter (Chapter 5), various experiments will be conducted to test the methodologies setout in this chapter. One aspect is to verify the validity of the mathematical models (both the transformation functions and similarity measures) when LIDAR lines are used as the source of control for the photogrammetric georeferencing. This is implemented for the one and two step procedures. Also to test the effect of LIDAR lines extraction techniques either from patch intersection or through using intensity and range images. More importantly is testing the methodologies under multi sensor environment. High resolution satellite line cameras, aerial analog and digital cameras, medium format digital cameras, and direct georeferencing GPS/INS systems on top of the imaging sensors are all involved in the experiments.

CHAPTER 4

CO-REGISTRATION METHODOLOGY USING PLANAR PATCHES

4.1 Introduction

The previous chapter discussed the inclusion of straight-line features extracted from photogrammetric and LIDAR datasets in two approaches. The first approach utilizes LIDAR features as the source of control for the photogrammetric reconstruction in an integrated bundle adjustment. The second approach starts with constructing an arbitrary photogrammetric model, which is later aligned to the LIDAR reference frame through an absolute orientation using conjugate lines from both datasets. Still, such implementation required preliminary processing of LIDAR data in the form of planar patch detection and intersection or through interpolating the LIDAR range and intensity images to a uniform grid. The rationale behind implementing the methodology based on planar patches is referred to the following:

- As mentioned in Section 2.4, LIDAR systems are characterized by its ability to collect dense information from homogeneous surfaces, an advantage that encourages the utilization of such surfaces. On the other hand, areal primitives in photogrammetric datasets can be classified and extracted as mentioned in Subsection 2.5.1. Such primitives include, for example, roof tops and lakes.

- To come up with an alternative that will reduce the amount of processing and avoid probable quality risks of segmenting, intersecting, and interpolating LIDAR data to extract straight linear primitives. Utilizing LIDAR point patches in its raw state will considerably reduce the jeopardy of undetected processing errors. In addition to that, if raw LIDAR points are replaced by the LIDAR equation which includes the sensor model (as seen in Equation 2.1), this will open the door for self-calibrating the LIDAR system within a unified bundle adjustment procedure.

In principle, the co-registration of photogrammetric and LIDAR datasets using planar patches can be implemented in the same fashion as that of straight lines; one and two step procedure. In this thesis the 1-step method of directly incorporate LIDAR patches in the photogrammetric bundle adjustment will only be considered as schematically shown in Figure 4.1. The two-step procedure is already implemented in the research work of Habib et al. (2006b).

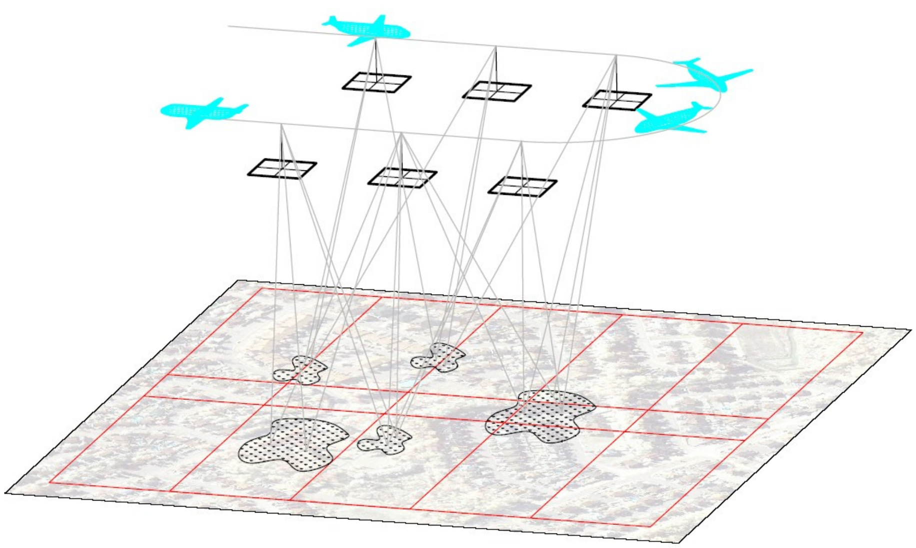

Figure 4.1. LIDAR patches as a source of control for photogrammetric georeferencing

4.2 Photogrammetric and LIDAR Planar Patches

A key factor in the successful implementation of this methodology is the availability of planar patches. As shown in the symbolic cartoon of Figure 4.2, planar patches are usually abundant in urban areas. With the high point density of today's LIDAR scanners, an adequate number of hits are collected from most of ground features of interest.

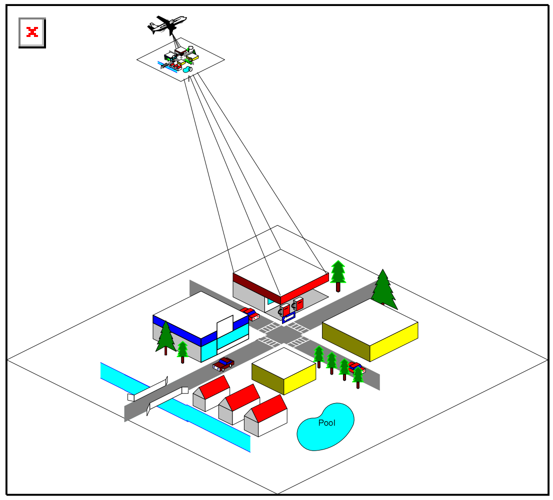

Figure 4.2. Photogrammetric and LIDAR coverage of a common planar surface

4.2.1 Photogrammetric Patches: Representation and Extraction

The photogrammetric planar surface will be identified and represented by three 2D points in the image space while in the object space three 3D points will be used, Figure 4.3. Three points are the minimum number of points required to explicitly define a plane.

Extracting the photogrammetric patches in the image space requires the representative image points to be measured on all overlapping images the points appear in. Figure 4.3 shows the three points measured in a sample image.

4.2.2 LIDAR Patches: Representation and Extraction

LIDAR patches are represented by the set of 3D points that comprise the patch under consideration in its raw format as collected by the scanner. For the scope set forth in this thesis, LIDAR patches are manually extracted from the point cloud. To extract such patches; the LIDAR patch is identified with the aid of the imagery dataset after which the set of points is extracted, grouped, labeled, and stored for further processing, Figure 4.4. Due to the fact that some planar patches that appear in the imagery might have some artifacts within it, chimneys on rooftops for example, the LIDAR patch points are run through a simple blunder detection to exclude points that do not belong to the real planar surface. This processing trend targets the superiority of LIDAR in efficiently describing homogenous surfaces. The main goal sought from this implementation is to use raw LIDAR footprints, which are assumed to be free of systematic errors, as the source of control for image georeferencing.

Figure 4.3. Photogrammetric planar patch represented by three points (A,B,C). LIDAR patch points are also shown on the roof

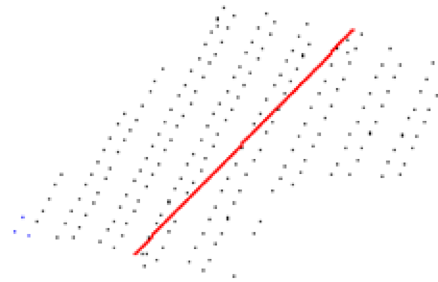

Figure 4.4. LIDAR patches manually identified and extracted with the aid of imagery

In summary, it is important to stress the following points:

- No point correspondence is required between the LIDAR and photogrammetric patch points,
- Raw LIDAR points will be used after the preliminary processing for the purpose of blunder detection only, and
- The correspondence and matching between the photogrammetric and LIDAR patches is achieved manually.

4.3 Mathematical Model: Transformation Function and Similarity Measure

The algorithm will mainly focus, similar to the case of straight line primitives, on the characteristics of planar patches in both datasets. The core principle behind this methodology is that in the absence of systematic errors, LIDAR points belonging to a certain planar-surface patch should coincide with the photogrammetric patch representing the same object space surface, Figure 4.5.

To explain the concept, let us consider a surface patch that is represented by two sets of points, namely the photogrammetric S_{PH}= {A, B, C} set and the LIDAR S_L= {(X_P, Y_P,

Z_P), P=1 to n} set, Figure 4.6. Since the LIDAR points are randomly distributed, no point-to-point correspondences can be assumed between the datasets; nevertheless, all points are coplanar. If a point (X_P, Y_P, Z_P) from the LIDAR patch belongs to the plane represented by the three photogrammetric points (A,B,C), then the volume of the pyramid with its vertex at the LIDAR point and its base at the photogrammetric patch (A,B,C) should equal zero. In a mathematical form, the determinant in Equation 4.1 represents twice the volume of the pyramid.

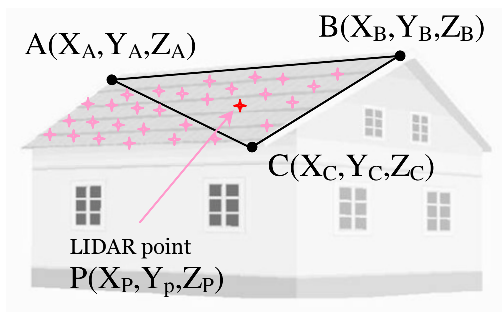

Figure 4.5. Photogrammetric (A,B,C) points and LIDAR patch points

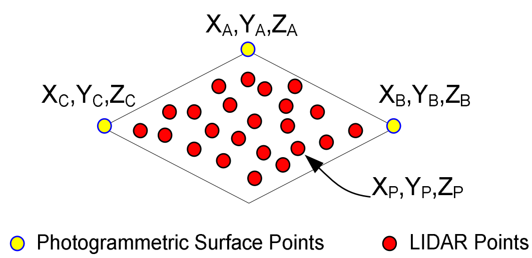

Figure 4.6. Photogrammetric and LIDAR coverage of a common planar surface

$$\mathbf{V} = \begin{vmatrix} \mathbf{X_P} & \mathbf{Y_P} & \mathbf{Z_P} & \mathbf{1} \\ \mathbf{X_A} & \mathbf{Y_A} & \mathbf{Z_A} & \mathbf{1} \\ \mathbf{X_B} & \mathbf{Y_B} & \mathbf{Z_B} & \mathbf{1} \\ \mathbf{X_C} & \mathbf{Y_C} & \mathbf{Z_C} & \mathbf{1} \end{vmatrix} = \begin{vmatrix} \mathbf{X_P - X_A} & \mathbf{Y_P - Y_A} & \mathbf{Z_P - Z_A} \\ \mathbf{X_B - X_A} & \mathbf{Y_B - Y_A} & \mathbf{Z_B - Z_A} \\ \mathbf{X_C - X_A} & \mathbf{Y_C - Y_A} & \mathbf{Z_C - Z_A} \end{vmatrix} = \mathbf{0} \qquad (4.1)$$

The above constraint is used as the basis for incorporating LIDAR points into the photogrammetric triangulation. In physical terms, this constraint means that the normal distance between any LIDAR point and the photogrammetric surface should be zero, or the volume of the tetrahedron comprised of the four points is also equal to zero when these points are coplanar. The ground coordinates of points A, B, and C, which are unknown at the beginning, are related to their image coordinates through the collinearity equations. This constraint is applied for all LIDAR points that are part of this surface patch. The same procedure is applied again for another candidate patch and so on.

Another advantage of this approach can be noticed when considering the systematic errors of a LIDAR system. If the system model is available with explicit expression of the error terms, the raw LIDAR points (X_P Y_P Z_P) in Equation 4.1 can be replaced by the LIDAR equation. In this case, any unknown error terms can be solved for in the overall bundle adjustment procedure.

4.4 Mathematical Model: Implementation

Assuming an object space planar surface, a roof of a house as shown in Figure 4.5 with the following facts:

- In the imagery, the planar surface is represented by three tie points (A,B,C) which are visible in at least two images. These points are measured in the imagery where this patch appears. One should note that the coordinates of (A,B,C) points in the ground coordinate system are not known.
- At the same time, a patch of LIDAR points is also collected on the same surface. The set of LIDAR points are represented by point (P).

The principle of the proposed similarity measure is that of the photogrammetric and LIDAR point sets to represent the same surface; each LIDAR point should be in-plane with the photogrammetric points (A, B, C). Repeating Equation 4.1,

$$\mathbf{V} = \begin{vmatrix} \mathbf{X_P} & \mathbf{Y_P} & \mathbf{Z_P} & \mathbf{1} \\ \mathbf{X_A} & \mathbf{Y_A} & \mathbf{Z_A} & \mathbf{1} \\ \mathbf{X_B} & \mathbf{Y_B} & \mathbf{Z_B} & \mathbf{1} \\ \mathbf{X_C} & \mathbf{Y_C} & \mathbf{Z_C} & \mathbf{1} \end{vmatrix} = \mathbf{0} \tag{4.2}$$

When using Laplace expansion along row 1, the determinant in Equation 4.2 can be represented as:

$$\mathbf{V} = \mathbf{X_P C_{X_P}} + \mathbf{Y_P C_{Y_P}} + \mathbf{Z_P C_{Z_P}} + \mathbf{1} \cdot \mathbf{C_1} = \mathbf{0} \tag{4.3}$$

Where $\mathbf{C_{X_P}}, \mathbf{C_{Y_P}}, \mathbf{C_{Z_P}}, \mathbf{C_1}$ in Equation 4.3 are the cofactors corresponding to row 1: ($\mathbf{X_P}$, $\mathbf{Y_P}$, $\mathbf{Z_P}$, and 1) and columns 1 through 4 respectively. Using the minors' notation, Equation 4.3 can be written as shown in Equation 4.4:

$$\mathbf{V} = \mathbf{X_P}\left|\mathbf{M_{X_P}}\right| - \mathbf{Y_P}\left|\mathbf{M_{Y_P}}\right| + \mathbf{Z_P}\left|\mathbf{M_{Z_P}}\right| - \mathbf{1} \cdot \left|\mathbf{M_1}\right| = \mathbf{0} \tag{4.4}$$

Where $\left|\mathbf{M_{X_P}}\right|$, $\left|\mathbf{M_{Y_P}}\right|$, $\left|\mathbf{M_{Z_P}}\right|$, $\left|\mathbf{M_1}\right|$ are the minors for $\mathbf{X_P}$, $\mathbf{Y_P}$, $\mathbf{Z_P}$, and 1 respectively, as shown in expanded form in Equations 4.5 to 4.8

$$\left|\mathbf{M_{X_P}}\right| = \mathbf{Y_A}(\mathbf{Z_B} - \mathbf{Z_C}) - \mathbf{Z_A}(\mathbf{Y_B} - \mathbf{Y_C}) + (\mathbf{Y_B Z_C} - \mathbf{Y_C Z_B}) \tag{4.5}$$

$$\left|\mathbf{M_{Y_P}}\right| = \mathbf{X_A}(\mathbf{Z_B} - \mathbf{Z_C}) - \mathbf{Z_A}(\mathbf{X_B} - \mathbf{X_C}) + (\mathbf{X_B Z_C} - \mathbf{X_C Z_B}) \tag{4.6}$$

$$\left|\mathbf{M_{Z_P}}\right| = \mathbf{X_A}(\mathbf{Y_B} - \mathbf{Y_C}) - \mathbf{Y_A}(\mathbf{X_B} - \mathbf{X_C}) + (\mathbf{X_B Y_C} - \mathbf{X_C Y_B}) \tag{4.7}$$

$$\left|\mathbf{M_1}\right| = \mathbf{X_A}(\mathbf{Y_B Z_C} - \mathbf{Y_C Z_B}) - \mathbf{Y_A}(\mathbf{X_B Z_C} - \mathbf{X_C Z_B}) + \mathbf{Z_A}(\mathbf{X_B Y_C} - \mathbf{X_C Y_B}) \tag{4.8}$$

Re-substituting the above minor formulas in Equation 4.4, we get the results as shown in Equation 4.9:

$$\begin{aligned} \mathbf{V} = \quad & \mathbf{X_P}\{\mathbf{Y_A}(\mathbf{Z_B}-\mathbf{Z_C})-\mathbf{Z_A}(\mathbf{Y_B}-\mathbf{Y_C})+(\mathbf{Y_B}\mathbf{Z_C}-\mathbf{Y_C}\mathbf{Z_B})\} \\ & -\mathbf{Y_P}\{\mathbf{X_A}(\mathbf{Z_B}-\mathbf{Z_C})-\mathbf{Z_A}(\mathbf{X_B}-\mathbf{X_C})+(\mathbf{X_B}\mathbf{Z_C}-\mathbf{X_C}\mathbf{Z_B})\} \\ & +\mathbf{Z_P}\{\mathbf{X_A}(\mathbf{Y_B}-\mathbf{Y_C})-\mathbf{Y_A}(\mathbf{X_B}-\mathbf{X_C})+(\mathbf{X_B}\mathbf{Y_C}-\mathbf{X_C}\mathbf{Y_B})\} \\ & -1\cdot\{\mathbf{X_A}(\mathbf{Y_B}\mathbf{Z_C}-\mathbf{Y_C}\mathbf{Z_B})-\mathbf{Y_A}(\mathbf{X_B}\mathbf{Z_C}-\mathbf{X_C}\mathbf{Z_B})+\mathbf{Z_A}(\mathbf{X_B}\mathbf{Y_C}-\mathbf{X_C}\mathbf{Y_B})\}=0 \end{aligned} \tag{4.9}$$

Equation 4.9 is a nonlinear relationship between the unknown parameters which are the ground coordinates of the photogrammetric points (A), (B), and (C) and the observed quantities as represented by the ground coordinates of the LIDAR point under consideration. This mathematical model is used to incorporate the constraint in the general bundle adjustment solution.

4.5 Minimum Configuration

It is of great importance that the minimum number and required orientation of patches be investigated for proper implementation of the methodology. LIDAR patches should be able to provide all the datum parameters; three translations (X_T, Y_T, Z_T), three rotations (ω, ϕ, κ), and one scale (S). Inspecting Figure 4.7, it is evident that the patches normal to the axes will provide the shift in the respective direction. For example, if any shift happens in the X-direction then the LIDAR point and the photogrammetric patch in the YZ plane will not be coplanar. The same discussion applies for the other directions. Hence a vertical patch is needed in each of the principle planes; XY, XZ, YZ.

The same rationale can be applied to estimating the rotation angles. For ω around the X-axis, the vertical patch in the YZ will not contribute to estimating that angle since LIDAR points will still belong to the photogrammetric patch even with a rotation around the X-axis. The patches in the XY and XZ planes will contribute to ω in this case. The same condition also applied to rotations around Y and Z axes. Consequently the patches already needed for estimating the shifts are adequate to determine the rotations. For the scale factor (S), an opposite patch is needed in one of the planes XY, XY, or YZ. Figure 4.7 shows an extra patch opposite to that in the YZ plane needed to determine the scale.

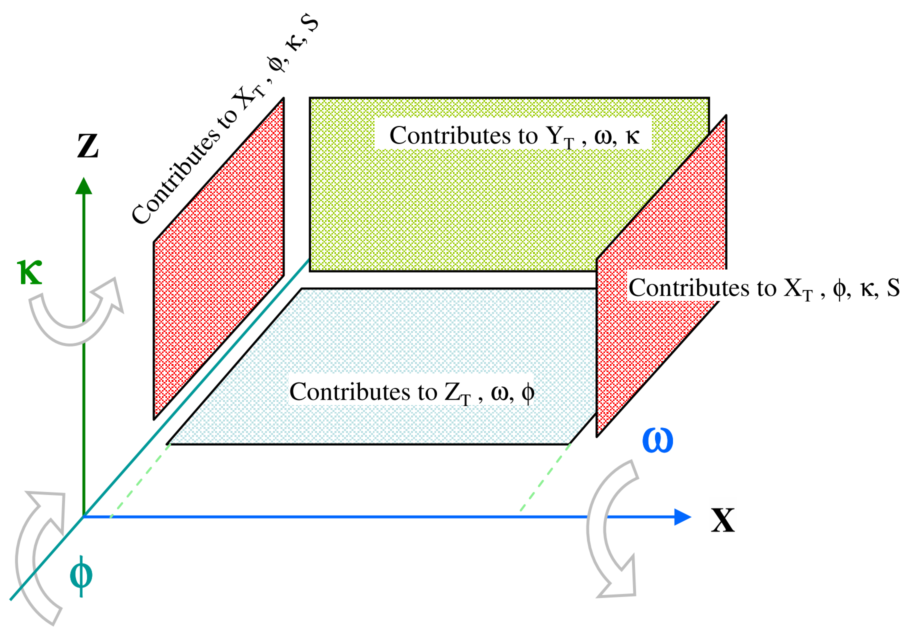

Figure 4.7. Optimal configuration required to establish the datum using planar patches methodology

In summary, for the situation of orthogonal patch configuration, a minimum of 4 patches along the major planes are required. It is important to note that in real object space, patches in different orientation usually exist and hence one patch, based on its orientation, may contribute to more than one shift, orientation, or the scale.

4.6 The Stochastic Model

To accommodate the solution process, the nonlinear relation between the parameters and observations, as shown in Equation 4.9, must be linearized. Due to the fact that both the parameters and the observations should be treated as observations infected by random errors, the linearization should be done with respect to the parameters and the observations. Details of the implementation of the stochastic model are shown in Appendix A.

After addressing the three basic components of the registration methodology using straight-line segments and areal patches, the performance of these components will be evaluated in the next experiments and results chapter using simulated and real data that have been captured by different cameras and high end LIDAR system.

CHAPTER 5

EXPERIMENTS AND RESULTS

5.1 Introduction

In the previous chapters, different approaches were devised for co-registering LIDAR and photogrammetric datasets. Chapter 3 presented two methodologies to utilize LIDAR straight-line features as the source of control information for aligning the photogrammetric model relative to the LIDAR reference frame. The first approach incorporates LIDAR lines as control information directly in a photogrammetric triangulation (1-step procedure). The second approach starts by generating a photogrammetric model through a photogrammetric triangulation using an arbitrary datum. LIDAR features are then used as control for the absolute orientation of the photogrammetric model. Chapter 4, on the other hand, introduced an approach for integrating LIDAR and photogrammetric datasets using planar patches. To validate the feasibility and applicability of the above methodologies, a number of datasets were solicited and analyzed.

In addition to verifying the different photogrammetric and LIDAR dataset integration methodologies, experimentation was also performed on the alternative techniques for extracting LIDAR linear features. LIDAR point clouds have no explicit semantic properties and consequently linear features are not readily available for direct measurement. In this work, LIDAR linear features are extracted from planar patch intersection and also by direct measurement from interpolated intensity and range images.

These experiments also feature four generations of photogrammetric acquisition systems; the traditional analog cameras, digital photogrammetric frame camera with GPS/INS systems, medium format frame cameras, and finally, the satellite-based line camera. With LIDAR dataset, this resembles a Multi Sensor Triangulation (MST). Multi-sensor triangulation is becoming an attractive area of research due to the recent and continuous development of diverse sensors and the profusion of multi spatial and multi temporal datasets from such sensors. For technical details about MST, please refer to Habib et al. (2006a). In the following section, a preview and summary of the objectives of the experimental procedure are given followed by a description of the available datasets and the experiments applied to each one.

5.2 Objectives of Experimental Work

This section summarizes the general goals of the experiments conducted in this thesis. These goals are reiterated for the individual sets of experiments in Sections 5.4 through 5.8. Although each set of experiments tackled a subset of these objectives, some objectives overlapped between two or more experiments.

- Suitability of the 1-step and 2-step procedures for georeferencing the photogrammetric model using LIDAR control lines.
- Suitability of LIDAR patches in providing adequate control for the photogrammetric bundle adjustment where LIDAR patches are directly involved in the adjustment procedure.
- Ability of the 2-step procedure using LIDAR control lines to detect systematic errors in either system.

- Applicability of the 1-step procedure using control patches for bundle adjustment with self-calibration.
- Effect of LIDAR lines extraction from patch intersection or from direct measurement from interpolated range and intensity images on the accuracy of the extracted lines and consequently on the quality of the georeferencing process.
- Effect of LIDAR interpolation method and grid size on the accuracy of the extracted lines and consequently on the quality of the georeferencing process.
- The performance of registration primitives, straight lines and planar patches, with metric analog cameras and medium format digital cameras.
- Validity of using the line-based georeferencing procedure for scenes captured by line camera.
- Validity of using the patch-based georeferencing procedure for scenes captured by line camera.
- Impact of integrating satellite scenes, aerial scenes, LIDAR data, and GPS/INS systems in a unified bundle adjustment procedure.

5.3 Implemented Sensors

Several datasets from different imaging and LIDAR sensors were acquired to fulfill the intended tests. In the following subsections, details about these datasets and sensors are presented.

5.3.1 Involved imaging sensors

Datasets from one analog camera, four frame digital cameras, and one line digital scanner were utilized in this research, as shown in Table 5.1.

Table 5.1. Imaging sensors utilized in the experimental work

<table>
<tr><td colspan="2">Analog Frame Camera</td><td colspan="2">Digital Line Scanner</td></tr>
<tr><td colspan="2"></td><td colspan="2"></td></tr>
<tr><td colspan="2">WILD RC10 9×9”</td><td colspan="2">Satellite Line Scanner: IKONOS</td></tr>
<tr><td colspan="4">Digital Frame Cameras</td></tr>
<tr><td></td><td></td><td></td><td></td></tr>
<tr><td>Applanix DSS (16MP)</td><td>Kodak 14n (14MP)</td><td>SONY 717 (5MP)</td><td>Canon EOS 1D (4MP)</td></tr>
</table>

A summary of the specifications of such imaging sensors and datasets is shown in Table 5.2 below.

5.3.2 Involved LIDAR scanners

Two laser scanners were used to capture the available LIDAR datasets: OPTECH ALTM 2050 and RIEGL Q140, which are shown in Figure 5.1. A brief listing of the specifications of each system is as follows:

Table 5.2. Imaging sensors utilized in the experimental work

Camera model	RC10 B/W	RC10 Color	Kodak 14N	SONY F717	Canon 1D	DSS	IKONOS
Focal length (mm)	153.167	153.167	~51.5	~11.67	~28.5	~55	~10,000
Frame size (W × H)	9” × 9”	9” × 9”	4500 × 3000	2560 × 1920	2464 × 1648	4077 × 4092	13800 × 1
# of captured images / scenes	6	7	9	17	23	18	2
Avg. flying height (m)	975	1375	1315	737	200	1500	800,000
Avg. base (m)	540	700	250	221	70	500	800,000
Pixel size (mm)	0.024	0.024	0.008	0.004	0.0115	0.009	0.010
Expected image measurement accuracy (mm)	±0.024	±0.024	±0.008	±0.004	±0.0115	±0.009	±0.010
Expected accuracy (assuming one pixel measurement error)							
planimetric (m)	0.15	0.21	0.20	0.25	0.08	0.25	1.00
vertical (m)	0.39	0.60	1.10	1.19	0.33	0.74	1.14

OPTECH ALTM 2050

RIEGL LMS Q140

Figure 5.1. Laser scanners used to capture LIDAR datasets.

OPTECH ALTM 2050

- 1,064 nm laser
- Laser pulse rate 50 KHz where the first and last responses of the range and intensity data were recorded
- Scan angle: to +/- 20 deg
- Max. operating altitude: 2,000 m
- At an altitude of 1,000 m a laser beam has a diameter of approximately 25cm
- Average flying height: 975m
- Mean point density: 2.24 points/m2 (~0.7m point spacing)
- Expected accuracy: 15 cm vertical and 50 cm horizontal.

RIEGL LMS Q140

- Effective shot rate: 9,000 pulses per second recording only the last range return.
- 60 degree swath
- 250 meter flying height above ground
- Expected accuracy: 15 cm vertical and 70 cm horizontal
- Beam divergence: 3 millirads

The available datasets were acquired in batches for research purposes. Based on the source and content, the datasets can be categorized as follows:

- KOREA I: Digital Imagery (Canon EOS 1D) + LIDAR (Riegl Q140)

- BRAZIL I: Analog (RC10 B/W) + Digital Imagery (SONY 717) + LIDAR (OPTECH ALTM 2050)
- BRAZIL II: Analog (RC10 Color) + Digital Imagery (KODAK 14n) + LIDAR (OPTECH ALTM 2050)
- KOREA II: Digital Frame Imagery (DSS) + Satellite Line Scanner (IKONOS) + LIDAR (OPTECH ALTM 2050)

As mentioned in Section 5.1, different datasets were processed to verify the suggested methodologies. In the following sections, five sets of experiments are presented along with the goals and results drawn from each set. The setup and design of the experimental work was intended to be carried out in a hierarchical fashion towards testing all objectives set forth in this thesis.

5.4 Experiments Set I

5.4.1 Objectives

The objective of this set of experiments is to compare the 1-step line-based georeferencing procedure versus the point-based one. Also the performance of analog metric and medium format digital imaging systems is evaluated. All above comparisons are based on LIDAR lines that are collected using patch intersection method.

5.4.2 Dataset used

In this set of experiments, the dataset BRAZIL II was used. It contains 7 color images taken by WILD-RC10 analog camera, Figure 5.2, and 9 images from Kodak N14 digital camera, Figure 5.3. More details about both cameras are previously listed in Table 5.2

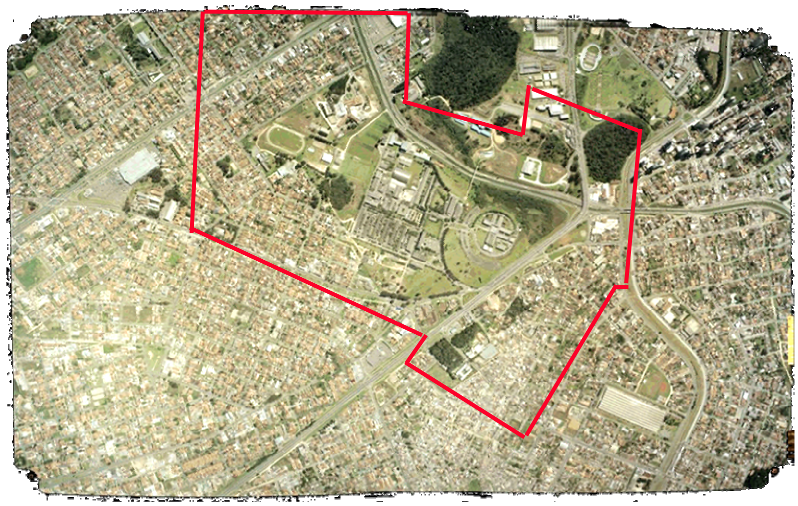

Figure 5.2. Coverage of RC10 color imagery. The red outline shows Kodak coverage

The LIDAR dataset was captured using OPTECH 2050 scanner. Figure 5.4 shows a shaded relief visualization of the point cloud. The expected accuracies of this scanner are 0.50m planimetric and 0.15m in the vertical direction.

Figure 5.3. Coverage of Kodak 14N camera

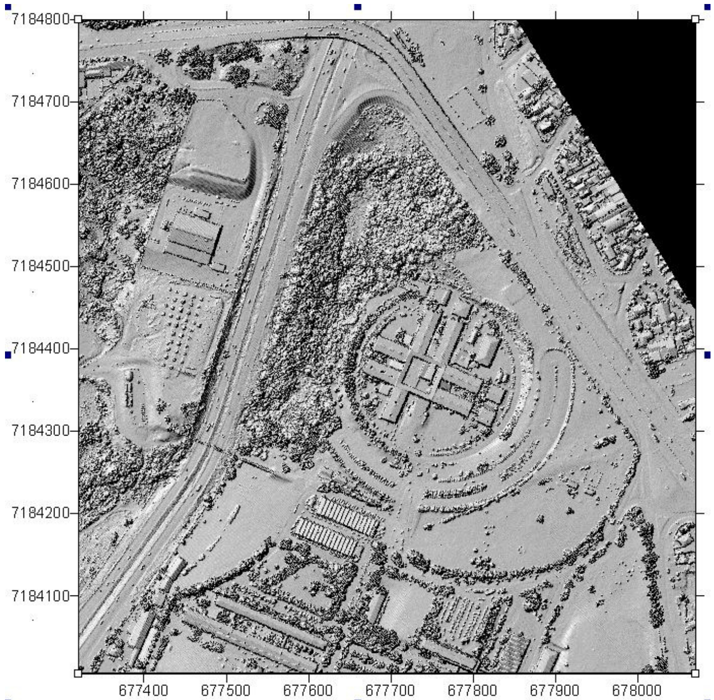

Figure 5.4. Shaded-relief map of OPTECH LIDAR coverage

5.4.3 Evaluation Criteria

A set of ground control points was provided with this dataset. These control points will be used to assess the registration results through check-point analysis. Moreover, check-point analysis of line controlled experiment will be compared to those from point-based bundle adjustment procedure.

5.4.4 Processing outline

In order to have a reference against which to validate the results obtained using LIDAR control lines, a point-based bundle adjustment is performed without incorporating any of the LIDAR lines. To do this, a set of tie and pre-surveyed points were identified and measured in the imagery. Part of the pre-surveyed points was allocated for control while the rest were used as check points. The line-based bundle adjustment is then conducted using LIDAR lines as the only source of control leaving all pre-surveyed points as check points. LIDAR lines were introduced to the bundle adjustment in two doses. Firstly, a limited number of lines are used to test the performance under restricted availability of linear features. Secondly, all LIDAR lines which were collected are used to control the bundle adjustment procedure.

RC10 – LIDAR Processing

For point-based processing, eleven control points and twenty four check points were used. Check-point analysis of this run is presented in the second column of Table 5.3. For line-based experiments, one hundred and nine lines were extracted from the LIDAR data. A subset of twenty seven well distributed lines was picked as the source of control for the -limited number of lines- version of the bundle adjustment. All 109 lines were used as the source of control in a third bundle adjustment case. Table 5.3 summarizes the quality of the aligned photogrammetric dataset through check-point analysis. The third column shows the results of using the 27 control lines, while the third column shows the results when all 109 available control lines were used.

Table 5.3. Check-point analysis for point- and line-controlled bundle adjustment

	Control points: 11	Control lines: 27	Control lines: 109
	24 check points	24 check points	24 check points
	RMSE, m	RMSE, m	RMSE, m
X	0.276	0.308	0.286
Y	0.176	0.206	0.199
Z	0.246	0.396	0.348

When compared to the point-based results, line-based results in both versions (limited- and all lines) demonstrated similar outcomes. LIDAR lines proved their feasibility in providing the necessary control to the photogrammetric bundle adjustment.

Kodak 14N – LIDAR Processing

As in the previous RC10 dataset processing, eight control points were used in the point-based georeferencing procedure. The results of analyzing forty-eight check points are shown in the second column of Table 5.4. To see the effect of the number of involved lines, line-based bundle adjustment was implemented in two ways; once with a subset of collected lines, and then using the whole set of extracted lines. In the first bundle adjustment, 24 lines from a total of one 103 extracted lines were used as the source of control, while all 103 lines were used in the second bundle adjustment.

Table 5.4. Check-point analysis for point- and line-controlled bundle adjustment

	Control points: 8	Control line: 24	Control line: 103
	48 check points	48 check points	48 check points
	RMSE, m	RMSE, m	RMSE, m
X	0.330	0.307	0.262
Y	0.273	0.290	0.335
Z	0.786	0.833	0.684

Table 5.4 summarizes the quality of the aligned photogrammetric dataset through check-point analysis. When compared to the second column of the table, the results presented in the third and fourth columns demonstrate the feasibility of using control LIDAR lines in the photogrammetric bundle adjustment. The results in the third column (less number of

lines) also confirm that a limited number of well-distributed lines is sufficient and leads to an acceptable solution.

5.4.5 Conclusions

Analyzing the previous results, a set of conclusions can be made:

- Straight-line features proved to be suitable in establishing a common reference frame for the photogrammetric and LIDAR surfaces.
- LIDAR-based and GCP-based photogrammetric results are comparable.
- Analog and digital cameras were both compatible with the LIDAR data, although the accuracies of the results in the digital camera case were inferior to that of the analog camera. This result is logical considering the expected accuracy of the digital camera as listed in Table 5.2.
- The registration of analog and digital blocks of imagery was successful with 20 to 30 lines. Considering an urban environment where man-made objects are available, this number of lines is accessible and can be collected in most datasets.

5.5 Experiments Set II

The first set of experiments showed several successful results. The registration between photogrammetric and LIDAR datasets using straight lines is now put to test using different datasets and different objectives. As with the previous set of experiments, the targeted objectives are first given, followed a by brief description of the involved datasets and processing scheme, and finally ending with the achieved results.

5.5.1 Objectives

In the previous dataset, only the 1-step procedure was tested. The objective of this set of experiments is to check the suitability of the 2-step procedure for georeferencing the photogrammetric model using LIDAR control lines. During the course of these experiments, the ability of the 2-step procedure to detect systematic errors in either system will be tested. Remedial measures, if possible, will be taken to alleviate the effects of such errors. The 1-step procedure will be tested again for this dataset. LIDAR lines are collected from the dataset using patch intersection.

5.5.2 Involved datasets

In this set of experiments the dataset KOREA I was used. The dataset contains 23 (2464 × 1648 pixel) digital images taken by Canon EOS-1D camera Figure 5.5. The expected accuracies in this dataset are 0.08m in planimetric and 0.33m in the vertical direction. In the overall spatial direction, 0.34m is expected.

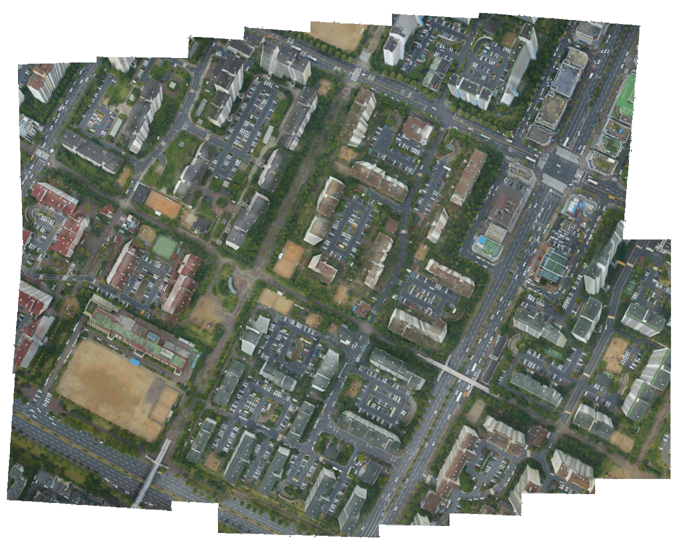

Figure 5.5. Coverage of Canon EOS 1D camera

On the LIDAR side, this dataset was collected by a RIEGL Q140 laser scanner. Figure 5.6 shows the shaded relief visualization of the point cloud. The expected accuracies of this scanner are 0.70m in the planimetric directions and 0.15m in the vertical.

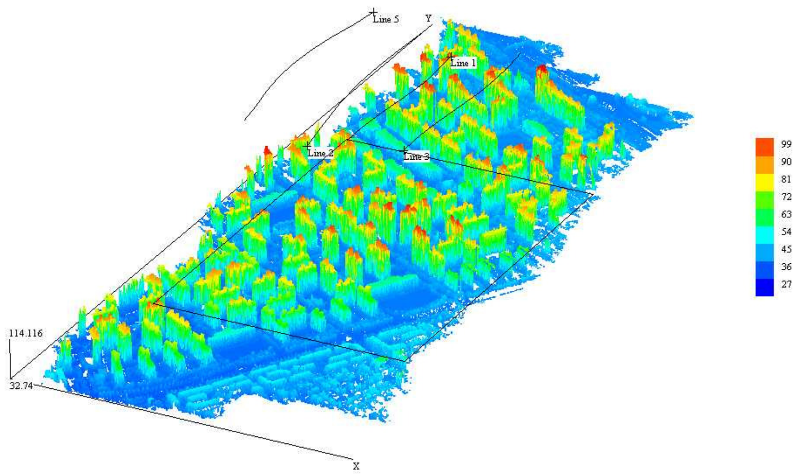

Figure 5.6. Shaded-relief map of RIEGL LIDAR coverage

5.5.3 Evaluation Criteria

Unfortunately, no independent ground control points were supplied along with this dataset. Hence, the adopted evaluation criteria will be as follows:

- The quality of fit, represented by the resulting variance component, of the 1-step bundle adjustment procedure when LIDAR lines are used as the source of control for the photogrammetric bundle adjustment.
- The quality of fit assessed as the normal distance between transformed photogrammetric lines and LIDAR lines.
- Comparative analysis of derived object coordinates from the 1- & 2-step methods. The object space coordinates of a certain object are estimated in both methods and compared.

5.5.4 Processing outline

With the objectives and evaluation criteria already set, the processing of this dataset is abstracted in the following points:

- 2-Step procedure: A model space is constructed with respect to an arbitrary datum. An absolute orientation is then implemented using LIDAR lines as the source of control. The quality of fit is assessed using normal distance between transformed lines
- 1-Step bundle adjustment is implemented using LIDAR lines as the source of control, the quality of fit is assessed by computing the variance component involving the observation residuals.
- Ground coordinates of tie points from 1- & 2-step methods are analyzed.

The above processing steps require the extraction of LIDAR and photogrammetric lines. In this dataset, homogeneous patches are manually identified to correspond to that of selected features in imagery, Figure 5.7. Planar surfaces are then fitted through the selected patches from which neighboring planar surfaces are intersected to produce object space line segments, Figure 5.8. A total of twenty-three well distributed 3D edges within the area of interest have been identified along ten buildings from three LIDAR strips. For the photogrammetric lines, the same set of lines corresponding to the LIDAR's was extracted using the procedure described in Subsection 3.2.1.

<u>2-Step Procedure</u>

With the linear features from both datasets extracted and on hand, a line-based photogrammetric model is constructed. Then, least-squares adjustment is used to solve for the parameters of the 3D similarity transformation function, and the results are shown in Table 5.5. A visual presentation of datasets after transformation is shown in Figure 5.9.

To assess the quality of fit, the mean normal distance between LIDAR lines and transformed photogrammetric line segments is computed. The results show a 3.45 m mean normal distance, a surprisingly poor result considering the camera, flight mission, and laser scanner specifications. The expected surface fit should be in the range of a sub-meter.

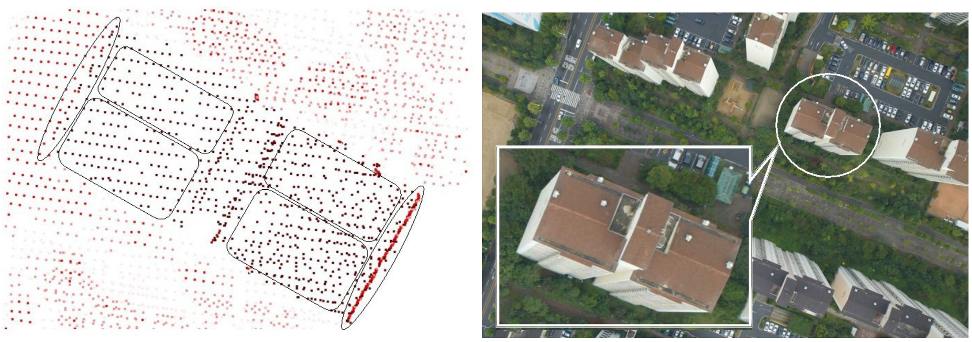

(a) (b)

Figure 5.7. Manually identified planar patches in the LIDAR data (a) guided by the corresponding optical image in aerial datasets (b)

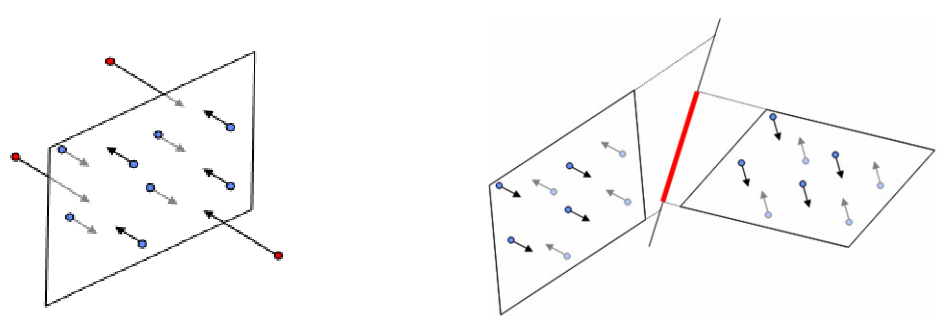

(a) (b)

Figure 5.8. Plane fitting and blunder detection from LIDAR patches (a) and plane intersection for extracting LIDAR lines (b)

Table 5.5. The 3D similarity transformation parameters between LIDAR and photogrammetric model

Parameter	Scale	X_T (m)	Y_T (m)	Z_T (m)	Ω (°)	Φ (°)	K (°)
Value	1.014034	5.36	-3.28	-42.03	1.99124	-1.23812	1.14074
StdDev	±0.002345	±0.86	±0.49	±0.47	±0.13926	±0.37131	±0.10388

Pursuing the problem, a closer look at the side view in the lower part of Figure 5.9, the discrepancy reveal a pattern of deviation between LIDAR and photogrammetric features similar to deformations arising from ignored radial lens distortion. The attention is now directed towards re-calibrating the camera.

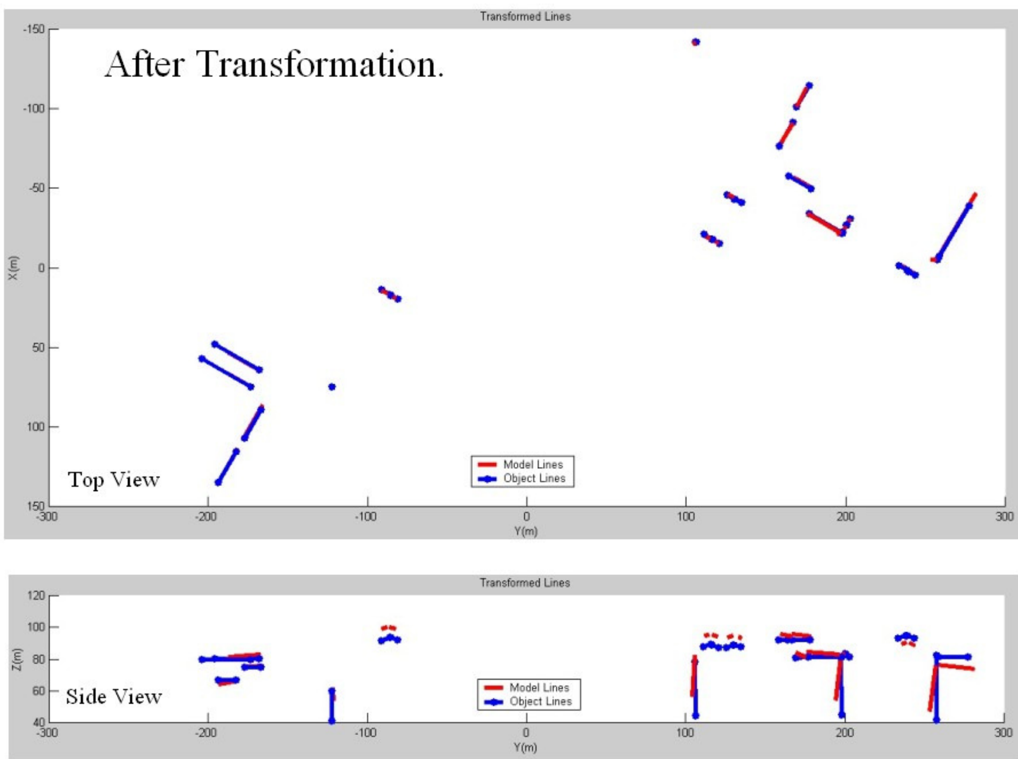

Figure 5.9. Photogrammetric and LIDAR datasets after transformation

To determine the radial lens distortion of the implemented camera, two alternatives were followed. The first alternative implemented the LIDAR features as control information within the bundle adjustment procedure in a self-calibration mode, allowing for the derivation of an estimate for the radial lens distortion. The estimated radial lens distortion coefficient turned out to be $-6.828\times10^{-5}mm^{-2}$. The second alternative determined an estimate of the radial lens distortion through a bundle adjustment with self-calibration involving imagery captured from a test field with numerous control points, which had been surveyed earlier. The estimated radial lens distortion coefficient turned out to be $-6.913\times10^{-5}mm^{-2}$, which is almost identical to the value determined by implementing the LIDAR features as control within the photogrammetric bundle adjustment. Afterwards, the registration procedure had been repeated while considering the radial lens distortion. The new parameters of the transformation function are presented in Table 5.6.

After considering the radial lens distortion, the mean normal distance between the laser and transformed photogrammetric line segments turned out to be 0.59 m, which is within the expected accuracy range. A sharp drop in the standard deviations of the transformation function parameters also took place, as can be seen when comparing Tables 5.5 and 5.6. The overall improvement in the spatial discrepancies, after introducing the radial lens distortion, verifies its existence. The side view in Figure 5.10 visually displays the improvement in the quality of fit between both datasets after proper camera calibration.

Table 5.6. The 3D similarity parameters between LIDAR and photogrammetric models after radial distortion compensation

Scale	X_T (m)	Y_T (m)	Z_T (m)	Ω (°)	Φ (°)	K (°)
1.026757	9.79	1.69	-43.45	5.197468	-3.910114	1.142367
±0.000732	±0.24	±0.15	±0.13	±0.037225	±0.099313	±0.033288

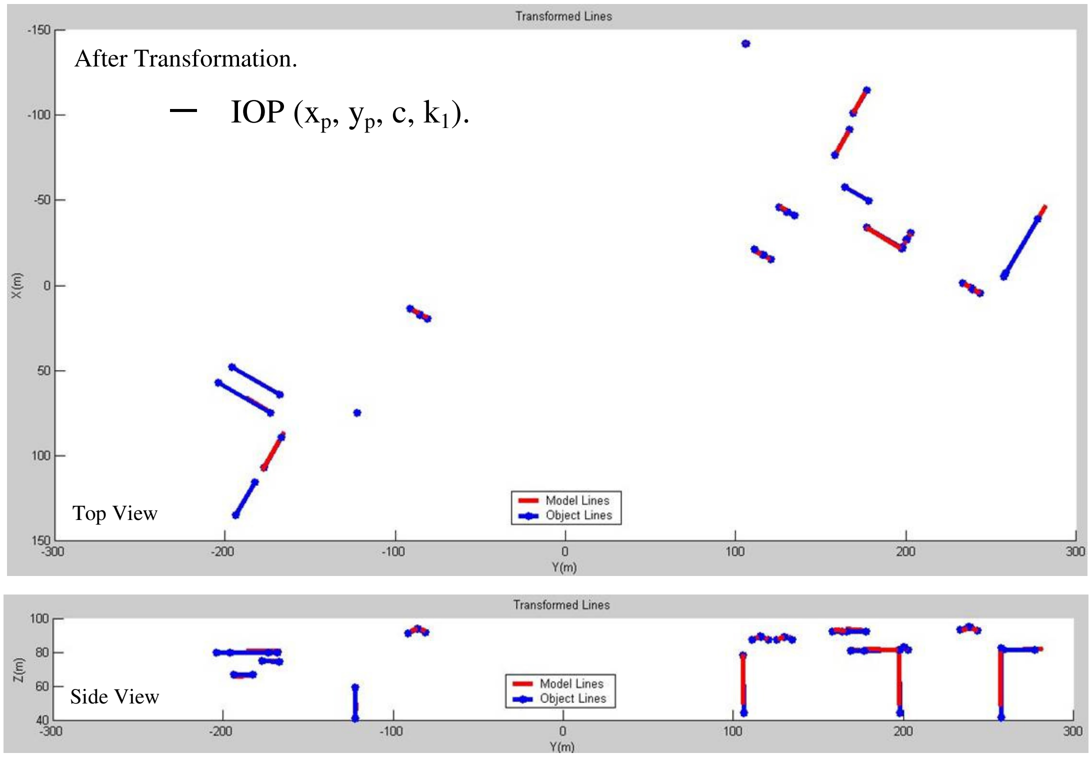

Figure 5.10. Aerial photogrammetric and LIDAR datasets after transformation and proper camera calibration

1-Step Procedure:

In this experiment, LIDAR lines were used as the source of control for the photogrammetric bundle adjustment procedure. The quality of fit, as represented by the variance component, using the camera before and after calibration is shown in Table 5.7. Although the value of variance component (1.3 pixels) using the un-calibrated camera is higher than after calibration, this increase is not significant enough to judge the presence of a systematic error in the camera.

Table 5.7. Quality of fit of the 1-step procedure between Canon EOS 1D and LIDAR

Before Camera Calibration	After Camera Calibration
Solution converged after 9 iterations σ_o = 0.01491mm (1.3 pixels)	Solution converged after 7 iterations σ_o = 0.00816mm (0.71 pixels)

Check-Point Analysis:

Due to the fact that no independent control points were provided with the dataset, check-point analysis was made internally between the point coordinates produced from the 1-one and 2-step procedures. Please note that the comparison is done between the results after calibrating the camera. Check-point analysis yielded RMSE values as shown in Table 5.8. Such RMSE values are within the range of expected errors.

Table 5.8. RMSE results of check points from 1- and 2-step procedures

# of control lines in both procedures	23
# of points used for RMSE	183
RMSE, X (m)	0.172
RMSE, Y (m)	0.120
RMSE, Z (m)	0.531

5.5.5 Conclusions

Analyzing the previous results, a set of conclusions can be made:

- Both 1-step & 2-step procedures were successful in registering the photogrammetric dataset to the LIDAR reference frame.
- The 2-step registration procedure was efficient in identifying systematic discrepancies in the involved sensors. After a closer look at the discrepancies' behavior, it was possible to justify the cause and take the necessary remedial measures to remove such errors. This conclusion stresses the need to precisely

calibrate both systems to guarantee the absence of systematic biases before the co-registration procedure.

- The 1-step procedure showed, to a certain degree, an indication of miss-fit between the two datasets (σ_o = .01491mm). The source of miss-fit is not directly plausible as it is in the 2-step case.
- The compatibility of the results from 1-step and 2-step procedures in registering the involved datasets.

5.6 Experiments Set III

In the previous two sets of experiments, LIDAR lines were extracted through patch intersection. LIDAR patches belonging to intersecting surfaces are identified and then processed for line extraction. This set of experiments deals primarily with alternate ways of extracting LIDAR lines and the effect of using such methods on the final registration outcomes between LIDAR and photogrammetric datasets.

5.6.1 Objectives

The primary objective of this dataset is to compare the 1- and 2-step georeferencing procedures in the following contexts:

- LIDAR lines are collected from patch intersection or from direct measurement from interpolated range and intensity images.
- Exploring the effect of LIDAR interpolation method and grid size on the accuracy of the extracted lines and consequently on the quality of the georeferencing process.

- Studying the effect of the above variations on datasets from metric analog and amateur digital cameras.

5.6.2 Involved datasets

The dataset used here is the one denoted by BRAZIL I and includes 6 B/W images taken by WILD-RC10 analog camera, Figure 5.11, and 17 images from SONY F717 digital camera, Figure 5.12. More details about the cameras can be found in Table 5.2.

Figure 5.11. Coverage of RC10 B/W imagery. The yellow outline shows SONY F717 coverage

The LIDAR dataset was captured using OPTECH 2050 scanner. Figure 5.13 shows a shaded relief visualization of the point cloud. The expected accuracies of this scanner are 0.50m planimetric and 0.15m in the vertical direction.

Figure 5.12. Coverage of SONY F717 camera

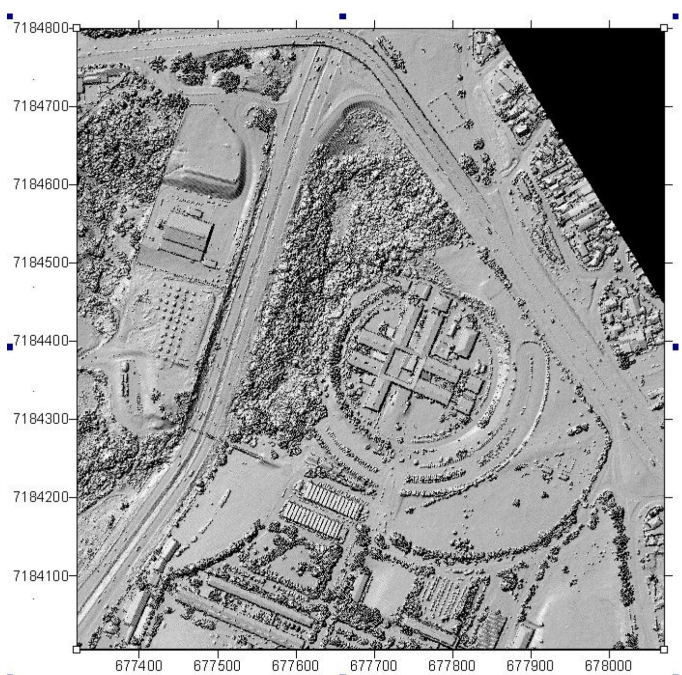

Figure 5.13. Shaded-relief map of OPTECH 2050 LIDAR coverage

5.6.3 Evaluation Criteria

A set of ground control points was provided with this dataset. For the 1-step procedure, these control points will be used to assess the registration results through check-point analysis. For the 2-step procedure, the normal distances between transformed photogrammetric lines and LIDAR lines.

5.6.4 Processing outline

LIDAR data will be processed to collect the needed lines using two techniques:

- The first technique is the same patch intersection used in the previous two experiment groups. Planar patches in the LIDAR dataset are identified, manually segmented, and then checked for blunders. Finally, neighboring planar patches intersected to extract the lines.
- In the second technique, where the goal is to simplify the extraction process, raw range and intensity data are first interpolated to a uniform grid using identical interpolation methods and parameters, Figure 5.14. The desired lines are then identified on the intensity image from which the planimetric coordinates of line ends are measured while observing height readings from the range image, Figure 5.15.

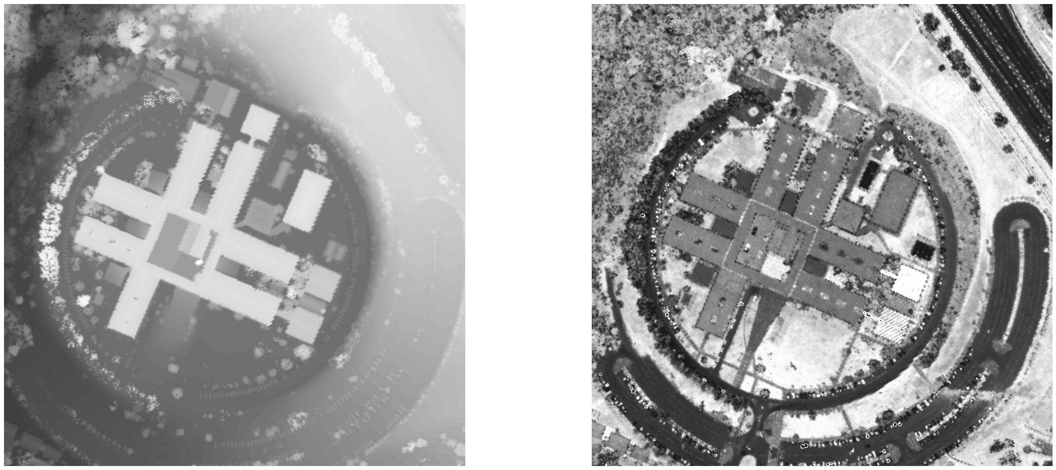

(a) (b)

Figure 5.14. Interpolated LIDAR range data visualized as range image (a) and intensity image (b).

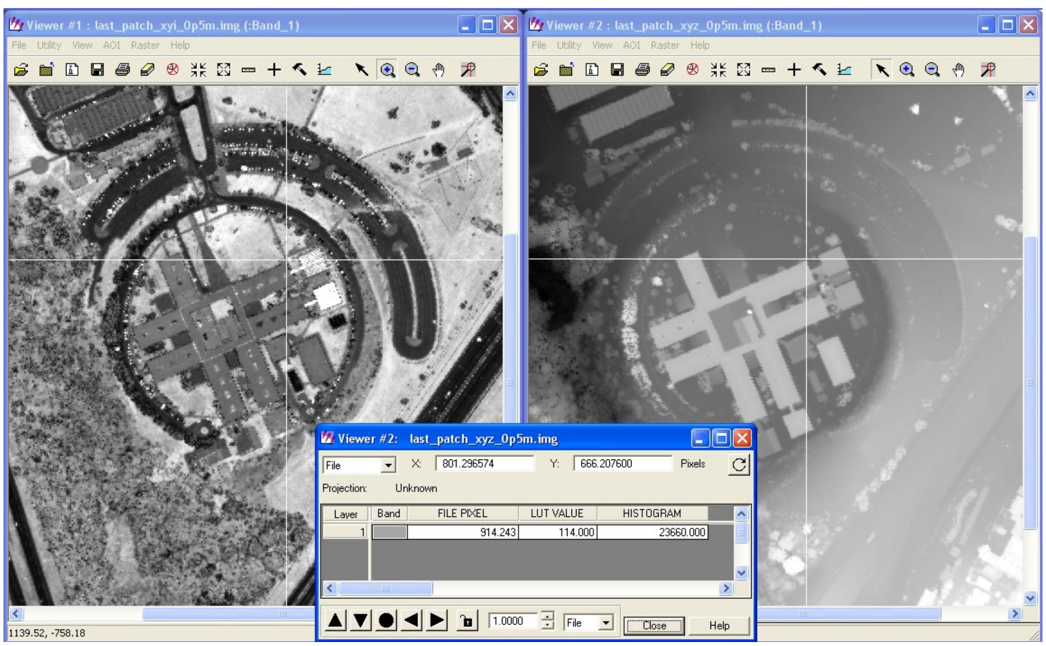

(a) (b)

Figure 5.15. Manually measuring planimetric coordinates from intensity image (a) and height value from range image (b).

Two alternatives were considered when interpolating LIDAR range and intensity data. The differences were mainly in the interpolation technique and grid size. Table 5.9 lists the specification and rationale of each interpolation alternative.

Table 5.9. Specification and rationale of LIDAR data interpolation alternatives

Interpolation: I1		**Rationale**
Grid Size	0.30 m	Closer to imagery Ground Sampling Distance (GSD)
Radius of Search Window	4 m	Guarantee at least 10 points in the neighborhood and fast processing.
Interpolation Method	IDW 2^{nd} degree	Inverse Distance Weighting takes into consideration the effect of neighboring points.
Interpolation: I2		**Rationale**
Grid Size	1.0 m	Closer to LIDAR point density
Radius of Search Window	4 m	Guarantee at least 10 points in the neighborhood and fast processing.
Interpolation Method	Nearest Neighbor	To avoid smoothing of the resulting surface

5.6.4.1 LIDAR lines as the source of control of the bundle adjustment: 1-Step procedure

In this set of experiments, extracted linear features from the interpolated intensity and range imagery are used as the source of control for the photogrammetric model. Due to limitations in identifying a sufficient number of neighboring planar patches over the entire area, linear features from patch intersection were not enough to establish proper datum for the photogrammetric adjustment. However, extracted LIDAR lines from patch intersection will be utilized later in the analysis of the 2-step procedure, Figure 5.16.

LIDAR – RC10

Straight-line segments from the interpolated LIDAR datasets (I1 and I2) are used in separate 1-step bundle adjustment experiments as the source of control for the photogrammetric triangulation of the RC-10 image block. Table 5.10 summarizes the quality of the photogrammetric triangulation through check-point analysis. More specifically, the photogrammetric coordinates of the check points are compared with those derived from independent geodetic measurements. The comparison results in Table 5.10 include the average difference between the photogrammetric and geodetic coordinates together with the corresponding standard deviation. The results for the I2 dataset in Table 5.10 demonstrate some overall improvement of the mean in the X- and Y- components.

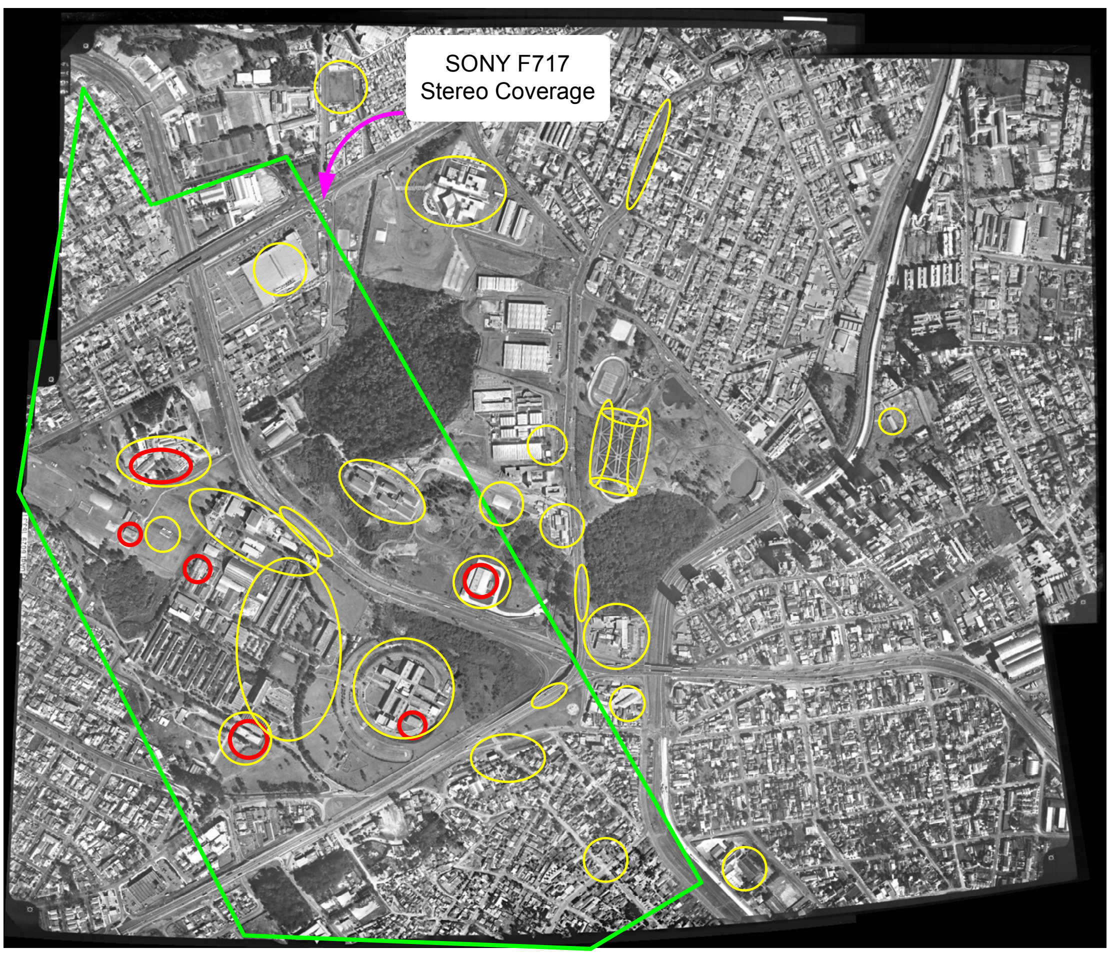

Figure 5.16. Distribution of lines extracted from intensity images -I1 and I2- (▬) and from patch intersection (▬) technique

LIDAR – SONY F717

Similar to the previous experiments for RC10, extracted straight-line segments from the two LIDAR datasets I1 and I2 are used in separate experiments as the source of control information for the photogrammetric triangulation of the SONY-F717 image block. Table 5.11 summarizes the results of check-point analysis after the photogrammetric BA.

Table 5.10. Check-point analysis of 1-step procedure of LIDAR – RC10 datasets

	LIDAR set I1			LIDAR set I2		
# of Control lines	80			79		
# of Check points	32			32		
	Mean	Std Dev	RMSE	Mean	Std Dev	RMSE
ΔX (m)	0.30	±0.21	0.366	0.15	±0.28	0.318
ΔY (m)	-0.21	±0.20	0.290	-0.04	±0.26	0.263
ΔZ (m)	-0.16	±0.28	0.322	0.18	±0.28	0.333

Table 5.11. Check-point analysis of 1-step procedure of LIDAR – SONY 717 datasets

	LIDAR set I1			LIDAR set I2		
# of Control lines	68			68		
# of Check points	31			31		
	Mean	Std Dev	RMSE	Mean	Std Dev	RMSE
ΔX (m)	0.41	±0.62	0.743	0.45	±0.68	0.815
ΔY (m)	0.33	±0.69	0.765	0.18	±0.65	0.674
ΔZ (m)	-0.32	±1.15	1.194	0.29	±1.14	1.176

Comparing the results in Tables 5.10 and 5.11, one can observe the following:

- Based on the standard deviations associated with the check points, the RC-10 data shows better alignment when compared to the SONY data. This should come as no surprise since the expected accuracy from the RC-10 is superior to that from the SONY (refer to Table 5.2).
- Based on the mean differences associated with the check points, the RC-10 shows better alignment when using linear features from the I2 dataset in place of those derived from I1. This is expected since the point spacing in I2 (1.0m) is closer to the point spacing associated with the raw LIDAR points (0.7m). In other words, I2 is a more realistic sampling considering the raw point density. Thus, the interpolation point density should be selected to be commensurate with the raw LIDAR data.
- Based on the mean differences and standard deviations associated with the check points, the SONY data shows almost identical alignment quality when using LIDAR features derived from the I1 and I2 datasets. This is expected since the photogrammetric errors for the SONY block (Table 5.2) are more dominant than the errors in the derived LIDAR linear features using different interpolation techniques.

5.6.4.2 LIDAR lines for the absolute orientation of the photogrammetric model: 2-Step procedure

In these experiments, separate photogrammetric models involving tie linear features have been generated from the RC-10 and SONY image blocks. After the bundle adjustment, the resulting model lines are represented by their 3D end points. The next step is to use these model straight line segments with the corresponding LIDAR lines in an absolute orientation procedure to align the photogrammetric model to the LIDAR reference frame. The LIDAR features are either derived from the interpolated I1 and I2 datasets or plane fitting and intersection procedures. It is important to note that the normal distances between transformed photogrammetric lines and LIDAR lines are used to evaluate the quality of fit. This change in evaluation criteria is caused by the distribution of lines extracted through patch intersection. As seen in Figure 5.16, the location of such lines is confined to a narrow area, hence, the calculated coordinates of check points based on this limited control includes extrapolation and can bias the results.

LIDAR – RC10

Table 5.12 lists the average normal vector components between conjugate RC-10 and LIDAR lines after the absolute orientation. These lines have been derived from I1, I2, and patch intersection, respectively. In Table 5.12, the standard deviations of the normal distances between the LIDAR and photogrammetric lines after the absolute orientation indicate that the best fit is achieved for the linear features, which have been derived from patch intersection followed by these from I2 and I1. This is not surprising since it is expected that the patch intersection will lead to the highest quality linear features since they are based on the raw LIDAR data. However, the improvement is mainly plausible in the planar sense, while little or no improvement is noticed in the vertical direction. Such a result indicates that the major improvement on the quality of LIDAR lines between I1, I2, and patch intersection falls in the quality of planimetric coordinates. The vertical quality is mainly shaped by that coming from the imagery side.

Table 5.12. Mean of normal distances between conjugate RC10 and LIDAR lines after absolute orientation

	I1		I2		Patch intersection	
# of lines	80		79		23	
DX (m)	0.03	±0.96	0.04	±0.52	0.005	±0.13
DY (m)	-0.03	±1.04	0.02	±0.54	-0.057	±0.12
DZ (m)	-0.02	±0.45	-0.06	±0.46	-0.115	±0.41

LIDAR – SONY 717

Table 5.13 lists the average normal vector components between conjugate SONY F717 and LIDAR lines after the absolute orientation. These lines have been derived from I1, I2, and patch intersection, respectively. Referring to Table 5.13, one can observe the same trend of improvement as noticed in the RC-10 results. A better quality of fit manifested in lower standard deviations is seen between the photogrammetric model and the derived LIDAR lines from patch intersection, then from I2, and finally from those derived from I1. Again, this improvement is mainly expressed in the planar direction rather than the vertical one for the reason explained in the RC-10 case above. However, this improvement is not as significant as that associated with the RC-10 data, especially between I2 and patch-intersection cases. This is expected since the photogrammetric errors in the SONY data are more dominant than those arising from using different interpolation and extraction techniques.

Table 5.13. Mean of normal distances between conjugate SONY F717 and LIDAR lines after absolute orientation

	I1		I2		Patch intersection	
# of lines	68		68		33	
DX (m)	0.07	±1.02	0.03	±0.60	0.02	± 0.31
DY (m)	-0.07	±1.09	0.01	±0.59	-0.008	± 0.26
DZ (m)	-0.10	±1.12	-0.13	±1.09	0.26	± 1.45

5.6.5 Conclusions

Analyzing the previous results, a set of conclusions can be made:

- The feasibility of using LIDAR intensity images to collect necessary control lines for orienting photogrammetric models.
- LIDAR linear features, which are derived from the neighboring patch intersection, are more accurate than those derived from the interpolated intensity and range images.
- The experiments highlighted the role played by the sampling methodology through the choice of the interpolation method, grid size, and search space. The enormous extra computational effort and storage space spent to produce over-sampled grids inversely affected the reconstruction of the object space. The sampling interval when interpolating LIDAR is recommended to match that of the original point density of LIDAR point cloud.

- Linear features from the RC-10 data exhibit higher quality when compared to these derived from the SONY-F717 data. This should be expected due to the better height-base ratio associated with the RC-10 image block.
- The quality of the derived LIDAR linear features influences the quality of the registration if the photogrammetric features exhibit a commensurate or better quality. Hence, the usage of patch intersection procedure for deriving LIDAR linear features is recommended only in the case of higher accuracy photogrammetric datasets like the RC-10. The extra effort in this approach cannot be justified when used with lower accuracy datasets like the SONY F717.
- The price/performance of the SONY F717 can be justified for a broad range of applications when compared to that of the more expensive RC-10 camera.

5.7 Experiments Set IV

The foregoing three sets of experiments comprehensively tested the registration procedure between LIDAR and photogrammetric datasets using straight lines. In this set of experiment, the registration methodology using planar patches will be verified using simulated and real datasets.

5.7.1 Objectives

Georeferencing of imagery using LIDAR patches is targeted in these experiments. The involved datasets will be processed to achieve the following goals:

- Verify the suitability of LIDAR patches in providing adequate control for the photogrammetric bundle adjustment where LIDAR patches are directly involved in the adjustment procedure.

- Comparing the patch-based bundle adjustment versus those based on lines and points.

- Applicability of the introduced methodology for bundle adjustment with self-calibration using control patches.

- Studying the performance of planar patches with metric analog cameras and medium format digital cameras.

5.7.2 Involved datasets

The BRAZIL II datasets will be used again in these experiments. It includes 7 color images taken by WILD-RC10 analog camera, and 9 images from Kodak 14n digital camera. The LIDAR dataset was captured using OPTECH ALTM 2050 scanner. The reader is referred to Figures 5.2, 5.3, and 5.4 for coverage details.

To monitor the performance of the patch-controlled bundle adjustment, a simulated dataset comprised of a stereopair with 60% overlap was generated using RC10 camera parameters over a simulated terrain of ±50 meters elevation variation. Eighty two control points were available in the overlap area. For the LIDAR data, 36 patches were generated parallel to the principal planes of the coordinate system (XY, XZ, and YZ), Figure 5.17.

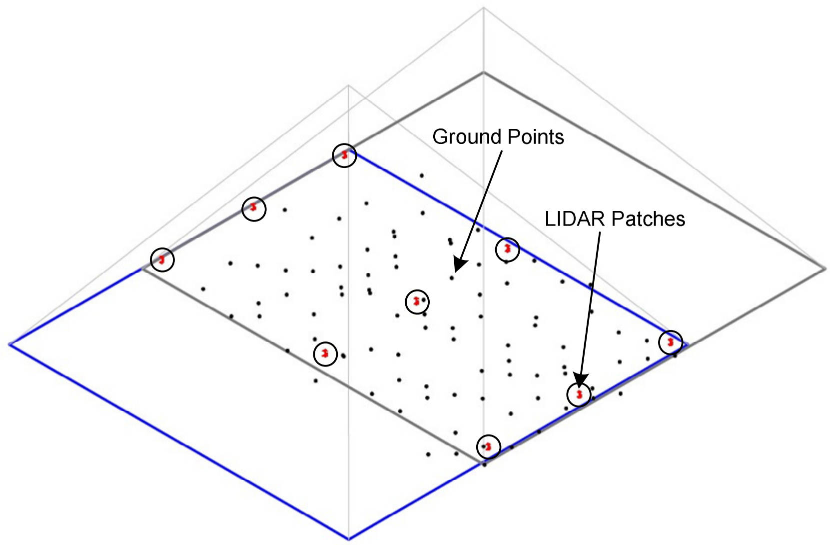

Figure 5.17. Simulated photogrammetric and LIDAR dataset

5.7.3 Evaluation Criteria

The provided control points will be used to assess the registration results through check-point analysis. Furthermore, check-point analysis of patch-controlled experiment will be compared to those from point-based and line-based bundle adjustment procedures implemented in the first set of experiments.

For self-calibration experiments, the assessment of the resulting camera parameters is based on check-point analysis of a point-based object space reconstruction. The object space is reconstructed once using the original Camera Calibration Certificate parameters and again using patch-based self-calibration results.

5.7.4 Processing outline

With the objectives and evaluation criteria already set, the experiments intended for the simulated and real parts of this dataset will proceed as depicted in the flow chart of Figure 5.18. The results of the simulated datasets will be assessed first. A point-based bundle adjustment will be done and check-point analysis will be performed. After that, the results of check-point analysis from the patch-controlled case are compared to those of the point-based. For real datasets, check-point analysis from point-based, line-based, and patch-based are compared.

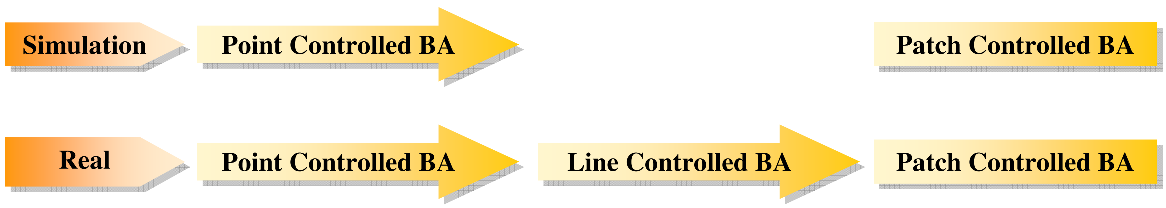

Figure 5.18. Planned experiments flow for the dataset

Simulated LIDAR – RC10 Analog Camera

As planned in Figure 5.18, a point-controlled bundle adjustment is implemented first. Nine of the 82 available ground control points were used as the sole source control; the remaining 73 points were used as check points. The first column of Table 5.14 shows the RMSE analysis of check points.

The attention now shifts to using LIDAR patches as the only source of control for the bundle adjustment. All 82 available control points are now used as check points. As seen in Table 5.14 for the RMSE analysis of check points, a complete compatibility of the results is obtained, indicating the suitability of LIDAR patches in controlling the photogrammetric bundle adjustment.

It is worth mentioning that the patches in this experiment were in an optimal configuration that completely serves the needs of the bundle adjustment procedure. Such perfect configuration is not always available in a real environment.

Table 5.14. Check-point analysis for point- and patch-controlled bundle adjustment

	73 check points	82 check points
	Control points used: 9	Control patches used: 36
	RMSE, m	RMSE, m
X	0.143334	0.123587
Y	0.126870	0.122276
Z	0.187240	0.178677

Simulated LIDAR – RC10 Analog Camera Self-Calibration

Continuing the tests in the simulated environment, further experiments were conducted to determine if LIDAR patches can be utilized for self-calibrating the implemented camera. For analysis purposes, the estimated camera parameters from the patch-controlled bundle adjustment with self-calibration procedure are used to perform a point-controlled bundle adjustment from which the results of check-point analysis are compared to those using the original camera parameters used for the simulation, Figure 5.19.

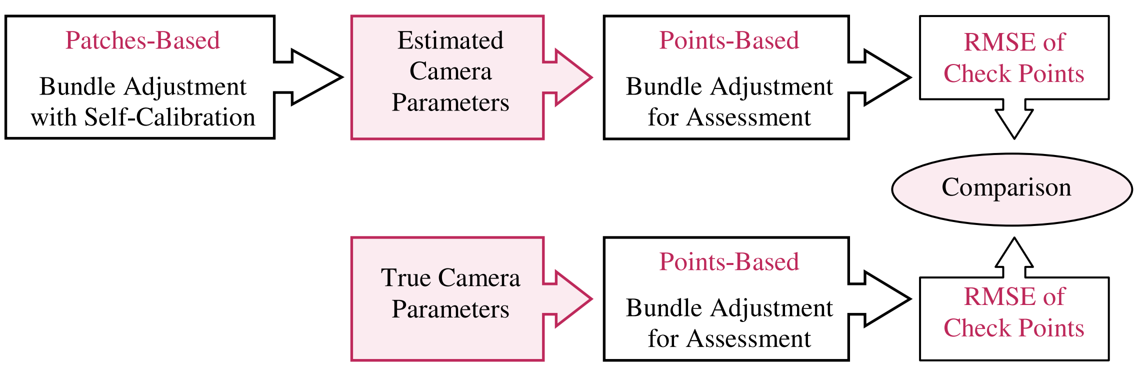

Figure 5.19. Estimating and assessing the camera parameters

Thirty-six patches are used in a patch-controlled bundle adjustment with self-calibration. The estimated camera parameters are shown in Table 5.15 in which a plausible difference especially in x_p and y_p parameters is noticed. This difference can be attributed to some IOP-EOP correlation during the bundle adjustment procedure. As an ultimate check of the quality of the estimated camera parameters, the estimated and true sensor parameters are then used in a point-controlled bundle adjustment. The check point analyses for these experiments are shown in Table 5.16. Comparing the results in Table 5.16, one can see a perfect compatibility between the reconstructed object space from the true parameters and those of the estimated ones using planar patches. Thus, LIDAR patches can be effectively used for patch-controlled bundle adjustment with the self-calibration procedure. Again, it is important to stress that the involved patches were optimally oriented and distributed.

Table 5.15. Camera calibration parameters using six patches as compared to original CCC

	Parameter Value	Std Dev	original CCC
x_p, mm	-0.268	1.7211153142e-01	0.001
y_p, mm	0.247	1.5845759820e-01	-0.053
c, mm	153.161	5.3967557184e-02	153.167
K1	3.2886171931e-08	1.1289922675e-09	2.99778547E-08
K2	-3.2512258510e-12	3.0607193964e-14	3.15091119E-12
P1	3.2667558448e-07	5.9666162499e-08	2.76490955E-07
P2	-1.1174580512e-06	6.2057780871e-08	1.06518601E-06
A1	0.0	1.5499218391e-05	0.0
A2	0.0	1.5499218391e-05	0.0

Table 5.16. Check-point analysis for point-controlled bundle adjustment

	Camera Used	
	Original CCC	Calibration from 36 patches
	RMSE, m	RMSE, m
X	0.125457	0.128792
Y	0.115792	0.118390
Z	0.156087	0.154765

In the following experiments, the findings using simulated data are to be verified using real datasets available for this purpose. Firstly, the behavior of RC10 analog and Kodak 14n digital imaging sensors under patch-controlled bundle adjustment is tested, followed by self-calibration experiments for RC10 camera.

Real LIDAR - RC10 Analog Camera

As setout in Figure 5.18, the patch-controlled bundle adjustment will be compared to that of point-based and line-based runs already done in the previous sets of experiments. The results are repeated in the second and third columns of Table 5.17. Seventeen patches along the roof tops of residential houses were collected throughout the available images. Conjugate LIDAR patches were manually identified and segmented to be used as the source of control for the photogrammetric bundle adjustment. The fourth column of Table 5.17 shows the results of check-point analysis from this patch-based case. The results presented in Table 5.17 demonstrate the feasibility of using control LIDAR patches similar to that when using control points or control lines in the photogrammetric bundle adjustment. Taking a closer look at the RMSE values in the fourth column of

Table 5.17, one can see some elevated values in the Y direction, which hints at the presence of slight biases in this direction. Pursuing this unexpected finding, one control point was added to the bundle adjustment in addition to the original 17 control patches. Inspecting the fifth column of Table 5.17 for the new RMSE analysis, one can notice the disappearance of such biases. The conclusion which can be drawn from these results is that the roof tops, which are mainly closer to the horizontal direction, did not adequately constrain the reconstructed object space in the horizontal direction. The elimination of the problem using only one control point supports the efficiency in using planar patches as the source control of the bundle adjustment procedure.

Table 5.17. Check-point analysis for point-, line-, and patch-controlled bundle adjustment

	Control points: 11	Control line: 109	Control patches: 17	Control: 17 patch +1 point
	24 check points	24 check points	24 check points	24 check points
	RMSE, m	RMSE, m	RMSE, m	RMSE, m
X	0.276	0.286	0.295	0.252
Y	0.176	0.199	**0.301**	0.193
Z	0.246	0.348	0.282	0.275

Real LIDAR – Kodak 14n Digital Camera

As in the previous RC10 dataset processing, the patch-controlled bundle adjustment will be compared to that of point-based and line-based runs already done in the previous sets of experiments. The results are repeated in the second and third columns of Table 5.18. Twenty six patches along the roof tops of residential houses were collected throughout the available images. Conjugate LIDAR patches were manually identified and segmented to be used as the source of control for the photogrammetric bundle adjustment. The fourth column of Table 5.18 shows the results of check-point analysis from this patch-based case. The results presented in Table 5.18 demonstrate comparative feasibility of using control LIDAR patches to that when using control points or control lines in the photogrammetric bundle adjustment. As in the RC10 case, the mean error in the fourth column of Table 5.18 shows some elevated values in the X and Y directions, which hints at the presence of slight biases in these directions. Pursuing this unexpected finding, three control points were added to the bundle adjustment in addition to the original 26 control patches. Inspecting the fifth column of Table 5.17 for the new RMSE analysis, one can notice the disappearance of such biases. The same conclusion can be drawn from these results. The roof tops, which are mainly closer to the horizontal direction, did not adequately constrain the reconstructed object space in the horizontal direction. The elimination of the problem, using as few as three control points, supports the efficiency of planar patches as the source control of the bundle adjustment procedure.

Table 5.18. Check-point analysis for point-, line-, and patch-controlled bundle adjustment

	Control points: 8	Control line: 103	Control patches: 26	Control: 26 patches +3 points
	48 check points	48 check points	48 check points	48 check points
	RMSE, m	RMSE, m	RMSE, m	RMSE, m
X	0.330	0.262	**0.987**	0.505
Y	0.273	0.335	**1.504**	0.279
Z	0.786	0.684	0.714	0.529

It is interesting to note that only one control was needed to have better results in the case of RC10 camera (Table 5.17), while it took 3 control points for the same purpose in the KODAK 14n camera case. This can be referred to the stronger geometry specifications of the RC10 imagery block. RC10 camera has 75° field of view compared to 26.2° for the KODAK 14n. Also, the average Base/Height ratio for the RC10 is 0.5 compared to 0.18 for the KODAK 14n.

Real LIDAR - RC10 Analog: Camera Self-Calibration

Similar to the simulated data experiments, real datasets are used to evaluate the feasibility of using LIDAR patches in a bundle adjustment with self-calibration of the implemented camera. Table 5.19 shows the results of these experiments, where the reconstructed object space, while using the original sensor parameters in the original camera calibration report (CCC), is compared to that derived while using the sensor parameters estimated from a patch-based bundle adjustment with self-calibration. Inspecting the RMSE results in Table 5.19, one can notice the lower quality of the reconstructed object space, using the estimated sensor parameters from the patch-based self-calibration procedure. This indicates that the available patches are in a less than optimal distribution and orientation; some help from additional control might be helpful in this case. In two separate follow-up experiments, 4 and 10 control points were added to the patch-based self-calibration run. The results, as indicated in the columns 5 and 6 of Table 5.19, show improved results for the 4 points case but not enough to reach the points-based accuracy level. For the 10 added control points, excellent compatibility with the original and the point-based calibration sets of sensor parameters. Hence, the same conclusion of the inadequacy of the orientation of the measured patches can be drawn for the self-calibration case as well.

Table 5.19. Check-point analysis for 10 point-controlled bundle adjustment with self-calibration

	Original CCC	Calibration from 10 Points	Calibration from 17 Patches	Calibration from 4 Points & 17 Patches	Calibration from 10 Points & 17 Patches
	RMSE, m	RMSE, m	RMSE, m	RMSE, m	RMSE, m
X	0.276	0.296	0.547	0.382	0.280
Y	0.175	0.169	0.656	0.263	0.176
Z	0.245	0.178	0.690	0.400	0.204

5.7.5 Conclusions

Analyzing the previous results, a set of conclusions can be made:

- Planar patches proved to be suitable in establishing a common reference frame for the LIDAR and photogrammetric surfaces provided that an adequate number of patches with optimal orientation are involved. Since most of the patches are almost horizontal, the quality of the georeferencing outcome in the planimetric directions is weaker when compared with point-based and line-based georeferencing procedures. This weakness can be compensated for by the inclusion of few ground control points.

- In addition, planar patches proved to be suitable for a bundle adjustment with self-calibration procedure. As with the previous conclusion, an adequate number of patches with optimal orientation must be available.

5.8 Experiments Set V

In the previous sets of experiments, the proposed line based and patch based georeferencing methodologies were tested with various aerial imaging and LIDAR systems. In this set of experiments, the scope of the involved sensory systems is extended to a complete Multi Sensor Triangulation (MST) environment. Satellite-based line cameras and GPS/INS systems attached to the aerial imaging system are added.

5.8.1 Objectives

The availability of acquired data from multiple sources motivated the realization of the following objectives:

- Validity of using the line-based georeferencing procedure for scenes captured by line camera.
- Validity of using the patch-based georeferencing procedure for scenes captured by line camera.
- Impact of integrating satellite scenes, aerial scenes, LIDAR data, and GPS/INS systems in a unified bundle adjustment procedure.

5.8.2 Involved datasets

In this set of experiments, the dataset KOREA II is utilized. It contains three blocks of 6 frame digital images captured by Applanix Digital Sensor System (DSS) over the city of Daejeon in South Korea. The DSS camera has a resolution of 16 mega-pixels. The position and orientation of the DSS camera were tracked using onboard GPS/INS systems. The major addition to this dataset is the stereopair from IKONOS satellite platform. This pair was captured in November 2001 over the same area. More details about both cameras are previously listed in Table 5.2. A multi-strip LIDAR coverage, corresponding to the DSS three blocks, was collected with an average point density of 2.67 point/m^2. Figures 5.20 – 5.22 side-by-side show the DSS image blocks and a visualization of the corresponding LIDAR coverage, while Figure 5.23 shows IKONOS coverage and the location of the DSS image blocks.

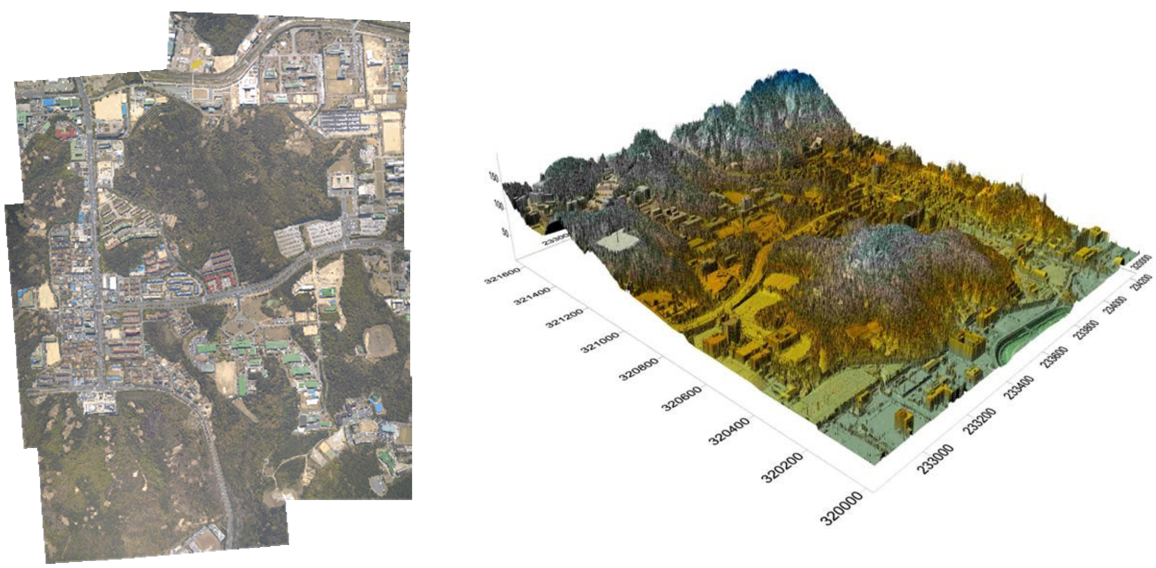

(a) (b)

Figure 5.20. DSS upper image block (a) and the corresponding LIDAR cloud (b)

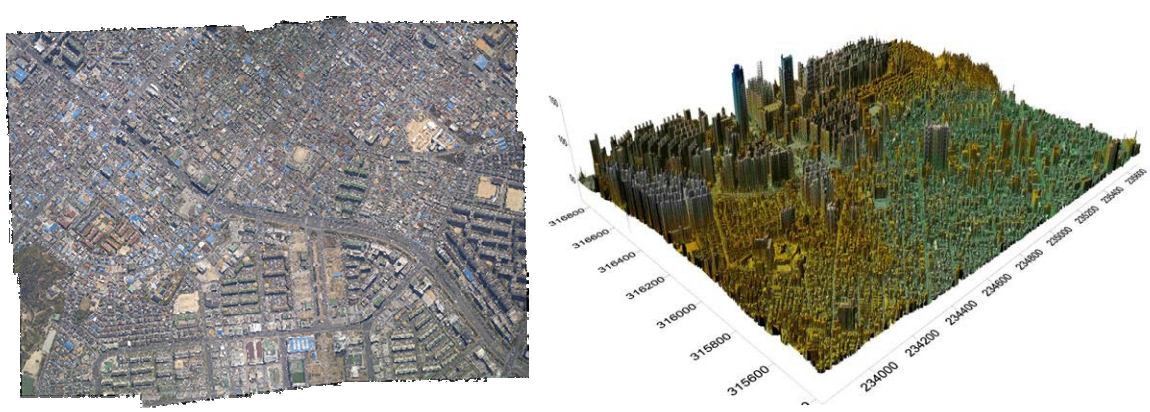

(a) (b)

Figure 5.21. DSS middle image block (a) and the corresponding LIDAR cloud (b)

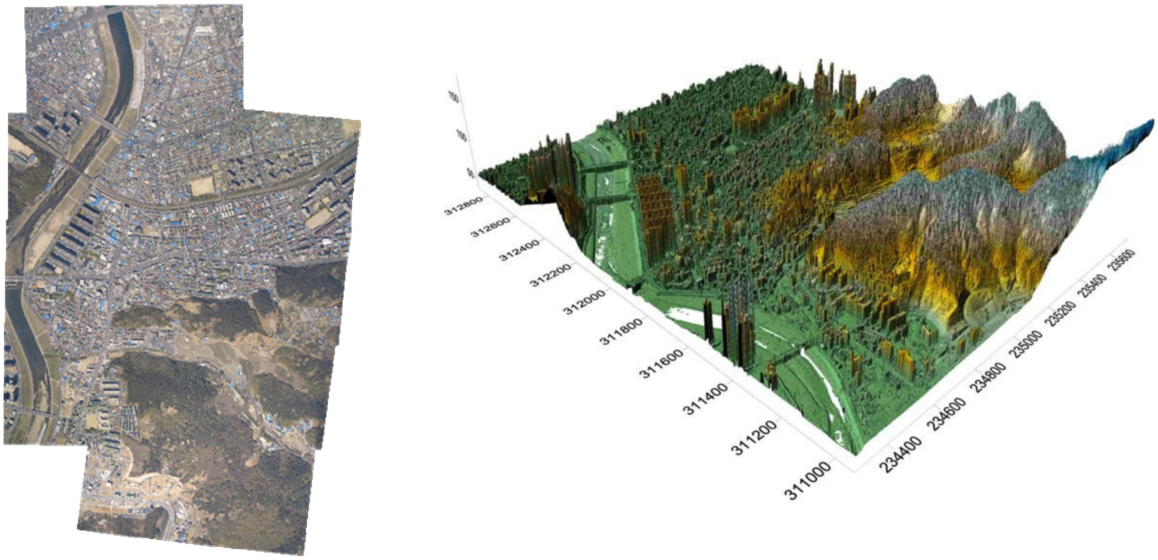

(a) (b)

Figure 5.22. DSS lower image block (a) and the corresponding LIDAR cloud (b)

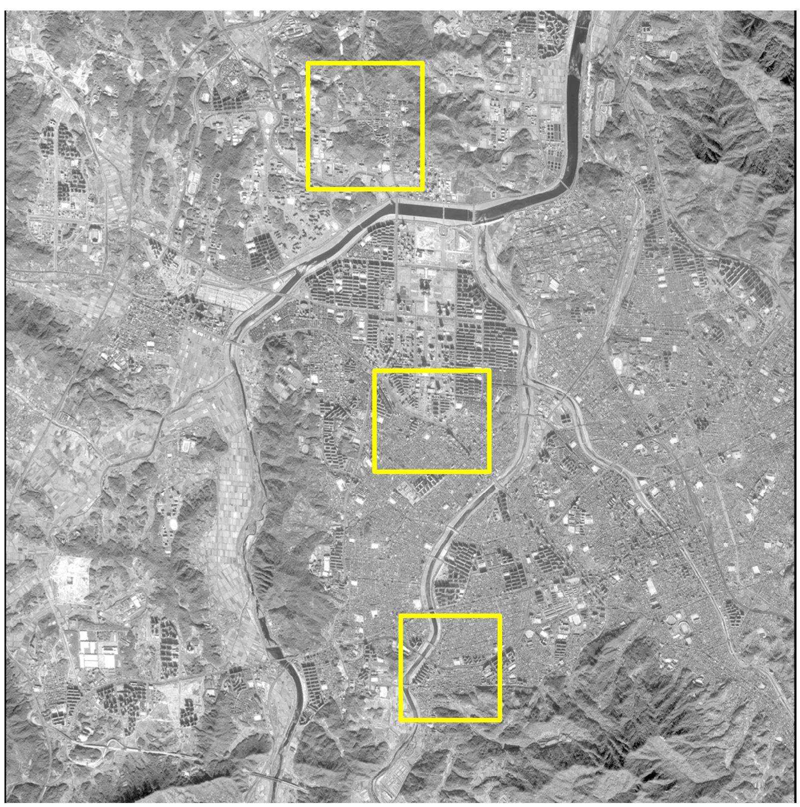

Figure 5.23. DSS imagery and LIDAR coverage location on the IKONOS scene

5.8.3 Evaluation Criteria

A set of 72 control points visible only in the IKONOS scenes were provided with the dataset. The layout and distribution of these control points is shown in Figure 5.24. Based on the experiment, part of these points was used as control in the bundle adjustment, while the rest were used as check points to assess the accuracy of the bundle adjustment.

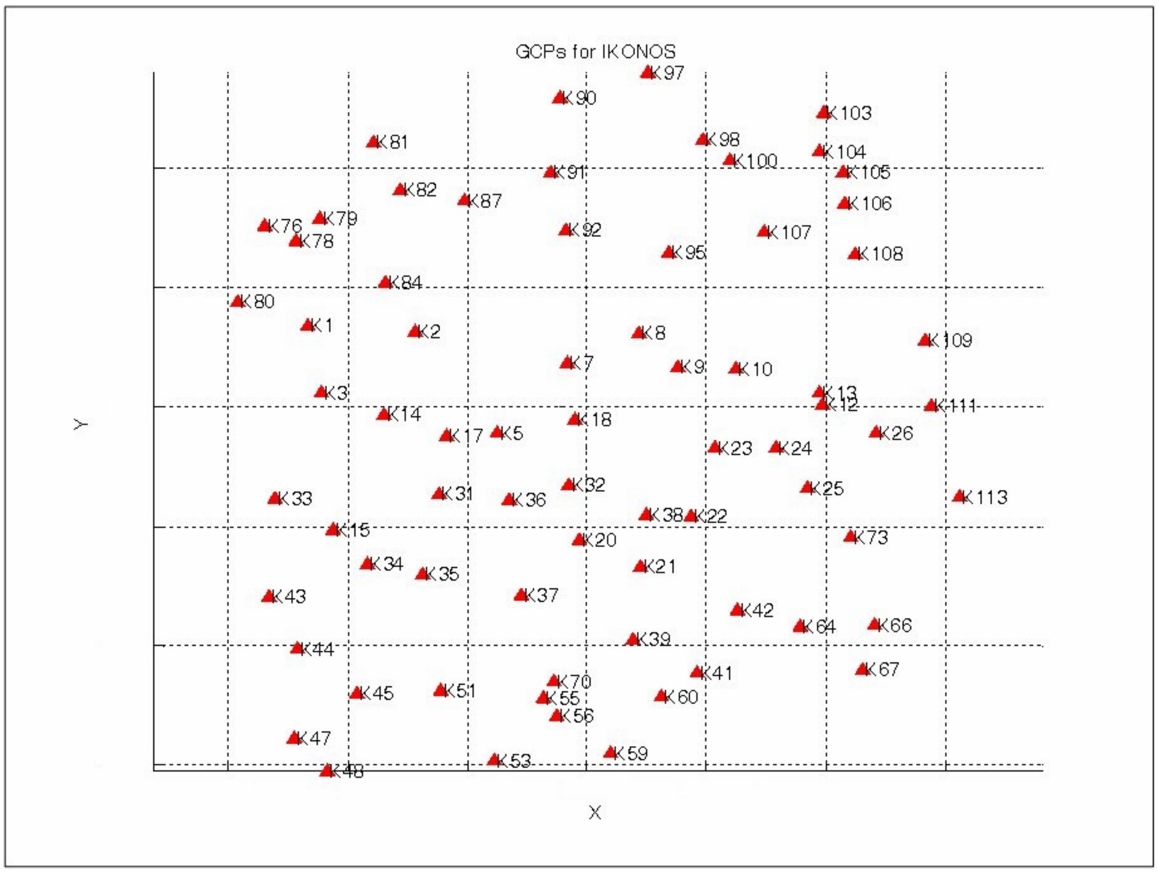

Figure 5.24. Layout and distribution of control points in IKONOS scenes coverage

5.8.4 Processing outline

The processing of this dataset will proceed as detailed in Figure 5.25. One IKONOS-only bundle adjustment will be processed for comparison purpose. In the rest of the cases, IKONOS will be simultaneously processed with the three blocks of DSS imagery. The source of control for the combined case will be varied from control points, control lines, control patches in the IKONOS and DSS scenes. The above cases are repeated while incorporating the observations from the GPS system associated with the DSS camera. Figure 5.25 shows the intended combination of experiments: a case is first selected from line 1 and implemented with all cases in lines 2 and 3. Check-point analysis is implemented for each case

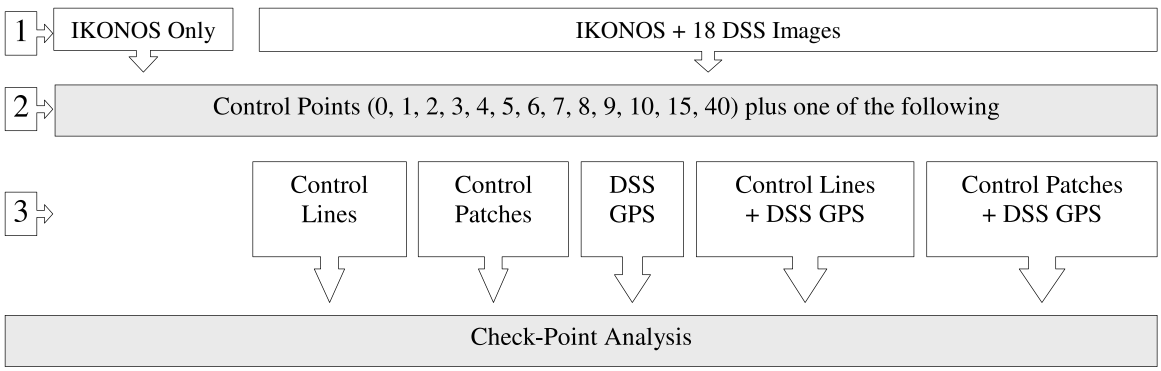

Figure 5.25. Process plan implemented for this dataset

The layout and distribution of control points for each of the cases outlined in line 2 of Figure 5.25 are illustrated in Figure 5.26. The circled points indicate control points while, un-circled points are left as check points. It is interesting to mention that none of the control points available for IKONOS scenes were visible in any of the DSS frame imagery. One hundred and thirty-eight LIDAR lines and one hundred and thirty-nine LIDAR patches were collected from the LIDAR data to be used in the experimentation. The results obtained from the bundle adjustment cases are shown in Table 5.20, followed by the discussion of the results.

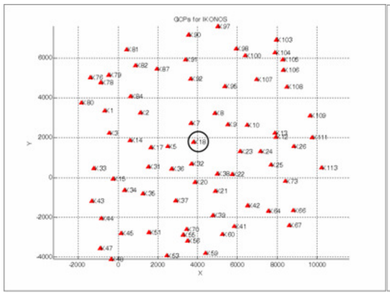

1 control point

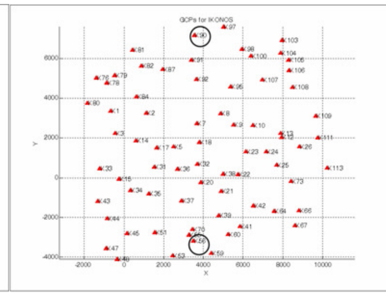

2 control points

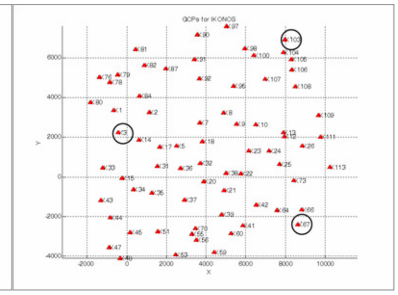

3 control points

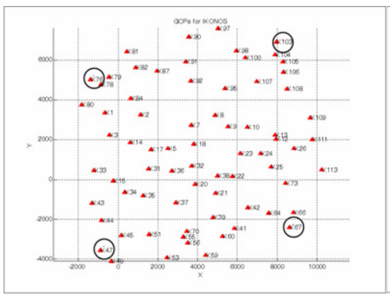

4 control points

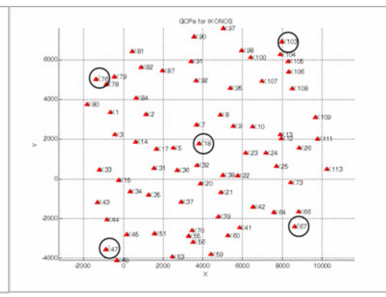

5 control points

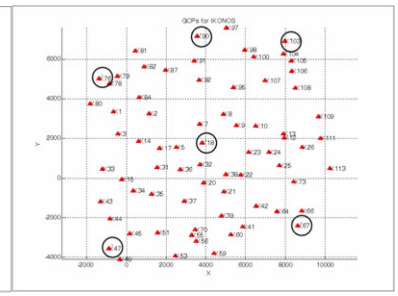

6 control points

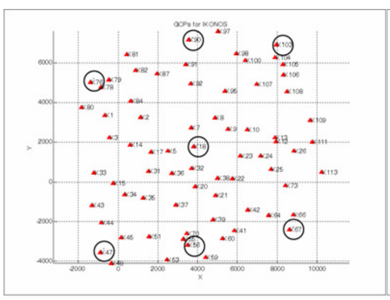

7 control points

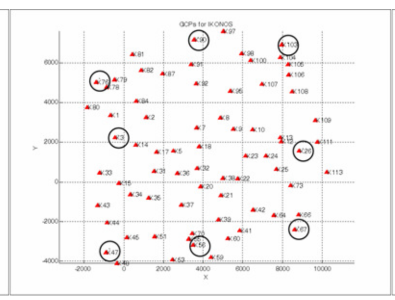

8 control points

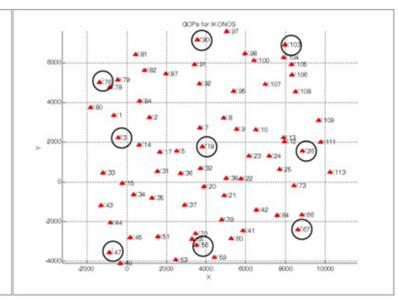

9 control points

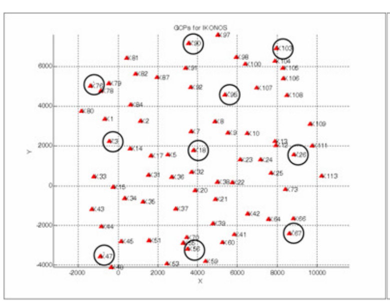

10 control points

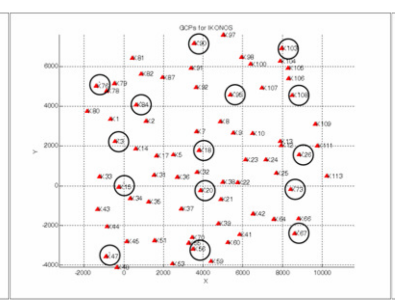

15 control points

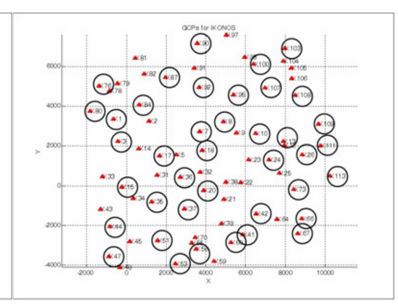

40 control points

Figure 5.26. Control and check points layout and distribution over IKONOS imagery

Table 5.20. Check-point analysis of MST bundle adjustment results

# of GCPs	RMSE, m	IKONOS only	IKONOS + 18 DSS Frame images					
		Control Points Only	Control Points Only	Control Points Plus				
				Control Lines	Control Patches	DSS GPS	Control Lines + DSS GPS	Control Patches + DSS GPS
0	X	N/A	N/A	2.105	3.582	2.109	2.116	2.374
	Y	N/A	N/A	1.370	3.394	1.048	1.358	2.580
	Z	N/A	N/A	1.757	2.207	1.963	1.803	2.294
	Total	N/A	N/A	3.065	5.406	3.066	3.093	4.190
1	X	N/A	N/A	2.122	3.579	2.401	2.125	2.415
	Y	N/A	N/A	1.327	3.358	1.134	1.313	2.691
	Z	N/A	N/A	1.678	2.223	2.072	1.686	2.312
	Total	N/A	N/A	3.013	5.388	3.368	3.014	4.292
2	X	N/A	N/A	2.183	3.383	2.332	2.158	2.500
	Y	N/A	N/A	1.404	2.731	1.023	1.399	2.114
	Z	N/A	N/A	1.743	2.071	1.736	1.799	2.172
	Total	N/A	N/A	3.127	4.816	3.082	3.139	3.930
3	X	N/A	2.024	1.900	1.948	1.797	1.794	1.784
	Y	N/A	1.077	1.253	1.311	1.049	1.244	1.292
	Z	N/A	21.199	1.738	1.756	1.967	1.726	1.766
	Total	N/A	21.322	2.863	2.932	2.863	2.783	2.824
4	X	N/A	2.012	1.717	1.630	1.729	1.768	1.622
	Y	N/A	1.061	1.109	1.001	1.032	1.111	0.999
	Z	N/A	19.826	1.775	1.816	1.886	1.775	1.840
	Total	N/A	19.956	2.707	2.638	2.759	2.741	2.649
5	X	N/A	1.907	1.786	1.670	1.805	1.733	1.647
	Y	N/A	1.084	1.115	1.009	1.024	1.112	1.008
	Z	N/A	3.7474	1.717	1.759	1.770	1.717	1.786
	Total	N/A	4.342	2.716	2.628	2.727	2.681	2.631

Table 5.20 *Continued*

		Control Points Only	Control Points Only	Control Lines	Control Patches	DSS GPS	Control Lines + GPS	Control Patches + GPS
6	X	1.547	1.835	1.747	1.635	1.784	1.798	1.644
	Y	1.302	1.078	1.119	1.018	1.02	1.121	1.016
	Z	3.06	2.59	1.716	1.756	1.754	1.716	1.778
	Total	3.668	3.352	2.692	2.607	2.702	2.726	2.627
7	X	1.442	1.568	1.738	1.516	1.657	1.783	1.578
	Y	1.608	1.029	1.13	1.025	1.025	1.132	1.024
	Z	3.29	2.392	1.722	1.774	1.747	1.724	1.792
	Total	3.936	3.039	2.696	2.549	2.618	2.726	2.598
8	X	1.471	1.673	1.633	1.422	1.526	1.674	1.476
	Y	1.552	1.08	1.124	1.030	1.006	1.127	1.027
	Z	2.884	2.777	1.629	1.709	1.819	1.634	1.729
	Total	3.591	3.417	2.566	2.45	2.579	2.596	2.495
9	X	1.427	1.561	1.649	1.435	1.517	1.691	1.492
	Y	1.867	1.064	1.129	1.04	1.017	1.132	1.037
	Z	3.334	1.702	1.586	1.67	1.727	1.59	1.694
	Total	4.079	2.543	2.552	2.435	2.513	2.582	2.484
10	X	1.746	1.575	1.651	1.46	1.542	1.69	1.511
	Y	1.028	1.041	1.136	1.033	1.012	1.139	1.033
	Z	2.304	1.637	1.591	1.647	1.689	1.593	1.667
	Total	3.068	2.499	2.559	2.432	2.501	2.587	2.476
15	X	1.514	1.43	1.491	1.329	1.389	1.502	1.349
	Y	1.854	1.022	1.048	0.977	1.000	1.049	0.974
	Z	2.051	1.654	1.65	1.738	1.771	1.651	1.757
	Total	3.152	2.413	2.458	2.397	2.463	2.466	2.421
40	X	1.092	1.129	1.173	1.110	1.122	1.143	1.095
	Y	0.870	0.863	0.921	0.845	0.859	0.934	0.846
	Z	1.450	1.528	1.495	1.475	1.563	1.498	1.478
	Total	2.013	2.087	2.112	2.030	2.107	2.103	2.026

In Table 5.20, the "N/A" means that no solution was attainable for this case of sensors/number of control points. For more clarity, the results in Table 5.20 were visually aggregated in Figure 5.27, where the Total RMSE values are plotted against the number of control points. The lower part of Figure 5.27 is enlarged in Figure 5.28 for further clarification. Examining Table 5.20 and Figure 5.27 one can notice the following points:

- The positive effect of adding frame imagery to IKONOS scenes could be noticed early in the results. The solution of the IKONOS-only case needed at least 6 control points converge, while the comparable case with frame images included, started to give results with 3 control points, although the RMSE values were higher in the vertical direction.
- Linear features showed compatible results to those of control points + GPS and control lines + GPS. This result supports the compatibility between the different georeferencing techniques.

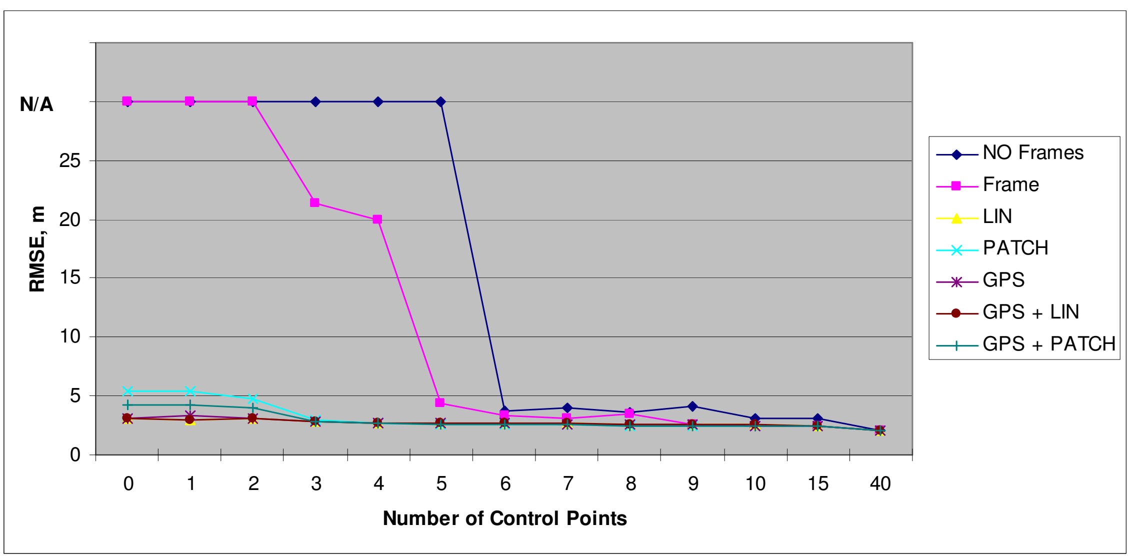

Figure 5.27. Check-point analysis from bundle adjustments involving IKONOS and DSS imagery

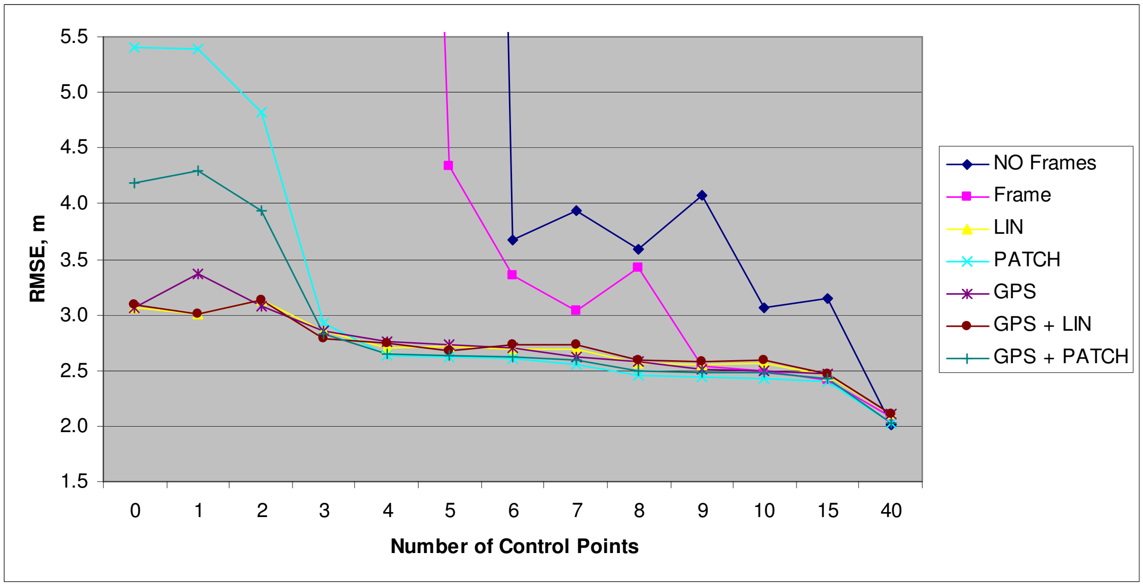

Figure 5.28. Check-point analysis from bundle adjustments involving IKONOS and DSS imagery (enlarged view of Figure 5.27)

- The presence of GPS sensor on top of the DSS camera had its prominent effect in the case where only control points are used. The contribution of the GPS system was minimal in the LIDAR lines and patches case; this indicates the adequacy of LIDAR lines or patches as the source of control in such cases.

- The distribution of the residual errors from check-point analysis is almost uniform around the whole area as shown in Figure 5.29. This figure shows the errors for the case of control patches and 15 control points with no GPS.

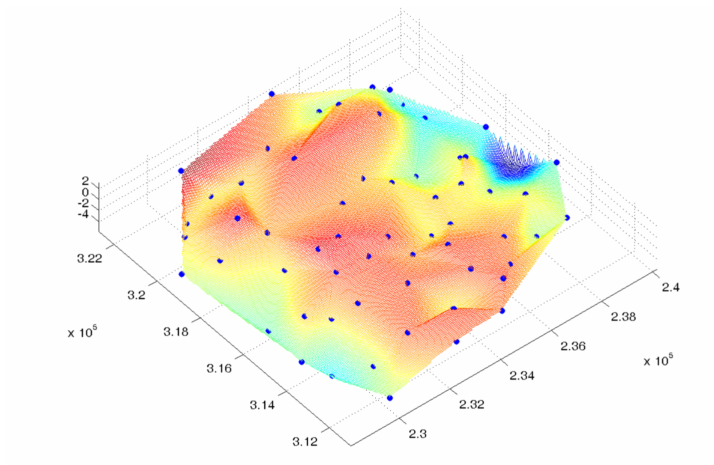

(a)

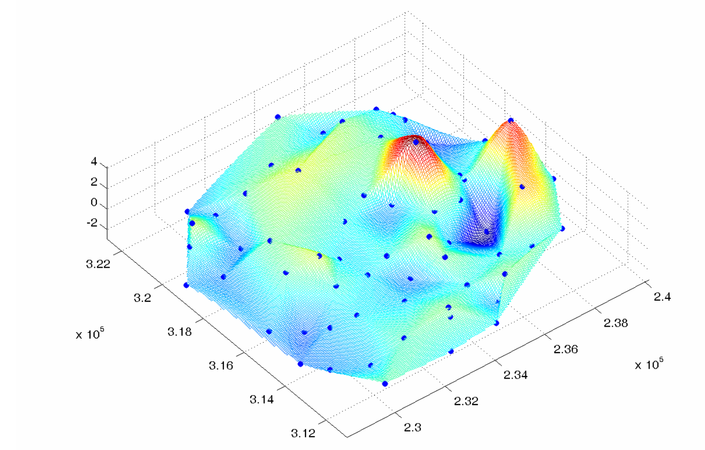

(b)

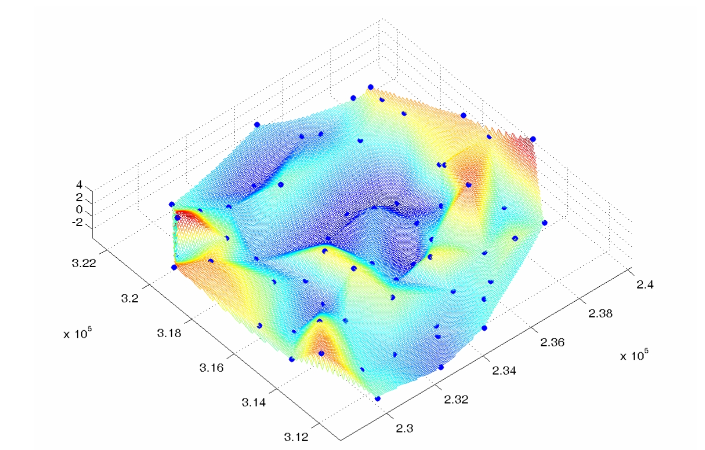

(c)

Figure 5.29. Check points errors for control patches and 15 control points with no GPS experiment in X-direction (a), Y-direction (b), and Z-direction (c)

5.8.5 Conclusions

Analyzing the previous results, a set of conclusions can be made:

- In general, multi sensor environment demonstrated better results than could be attained from single sensors. The combinatorial effect of individual sensor advantages could alleviate the weaknesses in the involved sensor geometry or probable biases in datasets.
- The developed methodologies where successful in georeferencing frame and line cameras scenes simultaneously.
- LIDAR lines proved to be highly reliable in establishing a common reference frame for IKONOS satellite scenes and DSS aerial frame imagery.
- Planar patches proved to be suitable in establishing a common reference frame for the LIDAR and photogrammetric data captured by line cameras, provided that an adequate number of patches with optimal orientation are available. Since most of the patches are almost horizontal, the quality of the georeferencing outcome in the planimetric directions is weaker when compared with point-based and line-based georeferencing procedures. This weakness can be compensated for by the inclusion of few ground control points or lines.

CHAPTER 6

CONCLUSIONS AND FUTURE WORK

6.1 Conclusions

The main objective of this research was to introduce new methodologies for integrating LIDAR and photogrammetric systems. Two categories of methodologies were suggested: one used straight-line features and the other used planar patches. After the introduction and literature review in Chapter 2, the details and implementation of line-based and patch-based methodologies were displayed in Chapters 3 and 4, respectively. Chapter 5 profiled the datasets and experimental work carried out for the verification of the suggested approaches, as well as the obtained results. The work frame of validating the accomplished registration methodologies also included the assessment of the following tasks:

- The compatibility of 1-step and 2-step procedures in incorporating LIDAR control features into the photogrammetric bundle adjustment.
- The ability of the 2-step procedure in detecting systematic errors in either system. This was shown for the imaging system since the system model is explicitly used. This is also possible for LIDAR systems if a reliable sensor model becomes available.
- The applicability to analog and digital frame cameras and digital line cameras. This task was performed on aerial and satellite platforms.

- The effect of LIDAR features collection technique. Two techniques for extracting LIDAR lines were used. One using interpolated range and intensity images and the other using patch intersection.
- Using raw LIDAR data in the patches methodology without interpolation.
- Using the patch-based methodologies for camera self-calibration. It is worth mentioning that utilizing linear features for bundle adjustment with self-calibration was not discussed in this thesis. The viability of linear features for camera calibration was previously introduced in the research work of Habib and Morgan 2003a.

In general, the experiments carried out in Chapter 5 made obvious the compatibility between LIDAR and photogrammetric surfaces. However, it is important to precisely calibrate both systems to guarantee the absence of systematic biases. In addition, the two surfaces must be relative to the same reference frame as a prerequisite for any further integration between the two datasets. Figure 6.1 shows a part of an orthophoto generated from the SONY F717 imagery -after the successful georeferencing of the imagery block- overlaid on interpolated LIDAR intensity image.

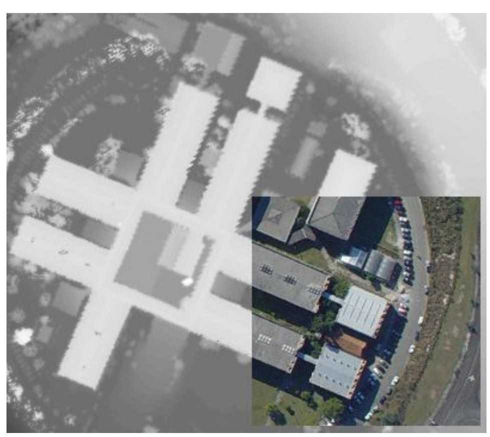

Figure 6.1. A patch of LIDAR intensity image overlaid by SONY-F717 orthophoto

Optical imagery can also be rendered onto the LIDAR data to provide a realistic 3D textured model of the area of interest. It is imperative to mention that applying the proposed methodologies is contingent on the availability of straight linear features and planar patches either natural or man made.

In summary, an overall set of conclusions can be categorized as follows:

General Registration Methodologies

In general terms, the successful outcomes of the developed georeferencing methodologies can be manifested in the following points:

- ♦ The introduced methodologies are successful in:
  - Using LIDAR lines and planar patches for photogrammetric georeferencing.
  - Identifying and justifying discrepancies between the photogrammetric and LIDAR data.
  - Delivering a georeferenced imagery of the same quality as point-based georeferencing procedures.
- ♦ The mathematical models and the similarity measures proved to be suitable and adequate for the purposes set. These models assume the absence of biases, which cannot be modeled by rigid-body transformation between the LIDAR and photogrammetric datasets.
- ♦ Direct incorporation of the LIDAR features in the photogrammetric triangulation is equivalent to independent processing of the image and LIDAR data followed by absolute orientation. In other words, these processing methodologies will not affect

the quality of the registration outcome. The only advantage of the latter methodology is the possibility of investigating the discrepancy pattern between the photogrammetric and LIDAR models after the absolute orientation. Such investigation might give meaningful clues about these discrepancies, which could be linked to systematic biases in the involved systems. On the other hand, the presence of systematic errors while directly using the LIDAR features in the triangulation will manifest itself in higher residuals. The investigation of the residual pattern and relating it to systematic errors is not a trivial task.

- The 2-step line-based methodology is general enough that it can be used for the co-registration of photogrammetric-to-LIDAR and LIDAR-to-LIDAR datasets.

- Line-based photogrammetric georeferencing requires pre-processing of the LIDAR data. While patch-based photogrammetric georeferencing incorporates the raw LIDAR points alleviating potential errors from intersecting planar patches or interpolating LIDAR point cloud.

Registration Features and Their Extraction

The conducted experimental work gave an insight on the proper practices by which datasets are to be processed leading to the extraction of registration primitives. In this context, the following conclusions can be devised:

- Straight line and planar patches proved their suitability to establish a common reference frame for the LIDAR and photogrammetric surfaces. Both registration features demonstrated reliable results and feasible implementation scope.

- An interesting conclusion is the feasibility of using LIDAR intensity images to collect necessary control for orienting photogrammetric models, although additional inaccuracies can be attributed to some difficulties and ambiguities when identifying linear features on the intensity image. The results also showed the effect of the interpolation technique and parameters. Smoothing and oversampling LIDAR data affect the accuracy of extracted features and give inferior results to that when using non-smoothing interpolation and a grid resolution close to the LIDAR point density.

- LIDAR linear features, which are derived from neighboring patch intersection without interpolating the point cloud, are more accurate than those derived from the interpolated intensity and range images. The derived LIDAR linear features from interpolated range and intensity images show better quality if the sampling interval of the produced imagery is commensurate with the point density of the raw LIDAR data. The enormous extra computational effort and storage space spent to produce over-sampled grids inversely affected the reconstruction of the object space.

Imaging Sensors, Biases, and Self-Calibration

From the view point of imaging sensors, their biases, and self-calibration, a set of findings can be summarized in the points that follow:

- The georeferencing using linear features of analog imaging sensors exhibit higher quality when compared to those derived from the digital ones. This should be expected due to the better height-base ratio associated with the analog image blocks. It is also important to note that the quality of derived LIDAR linear features influences the quality of the registration if the photogrammetric features exhibit a commensurate or better quality

- ♦ The registration methodology is capable of identifying biases and systematic errors between the involved datasets. The quality of fit between the registered models is improved following the removal of these biases.
- ♦ LIDAR planar patches can be utilized for self-calibrating involved cameras, provided that an adequate number of patches is involved and oriented along the three principle planes of the coordinate system. Also the patches approach is flexible enough to be used in various types of photogrammetric datasets.
- ♦ The developed methodologies were suitable for georeferencing datasets acquired by analog, digital frame, and line cameras.

Multi-Sensor Triangulation

The suggested georeferencing methodologies were capable of incorporating multiple data acquisition technologies, mainly: high resolution imaging satellites, medium-format digital imaging systems, and LIDAR systems. This integration made the following tasks possible:

- Taking advantage of the extended coverage of imaging satellites.
- Exploiting the high geometric resolution of medium-format digital imaging systems.
- Utilizing sparse frame imagery to improve the weak geometry of imaging satellites while reducing ground control point requirements.
- Using LIDAR data for photogrammetric georeferencing.

- Registering multi-primitive, multi-sensor, and multi-temporal triangulation procedure which enables consistent georeferencing/registration environment for multi-source spatial data.
- The outcomes of this procedure are valuable to change detection and environmental monitoring applications and can be used for high quality ortho-photo generation, Figure 6.2.

6.2 Recommendations for Future Work

It is recommended that future research addresses the following potential areas:

- Automation of the extraction of linear features from photogrammetric and LIDAR data, together with the correspondence between conjugate features.
- Automated segmentation of LIDAR data to extract the patches and linear features.
- More investigation into using the outcome from the georeferencing procedure for the verification of the system calibration.
- Introduce a LIDAR sensor model in the patch-based photogrammetric georeferencing to allow for LIDAR system calibration.
- Develop new visualization tools for an easier portrayal of the registration outcomes such as draping perspective images on LIDAR data to provide 3D textured models, Figure 6.3.
- Utilize the registration outcome for true ortho-photo generation over urban areas. See Figure 6.4 for an example of a generated orthophoto from KOREA I dataset.

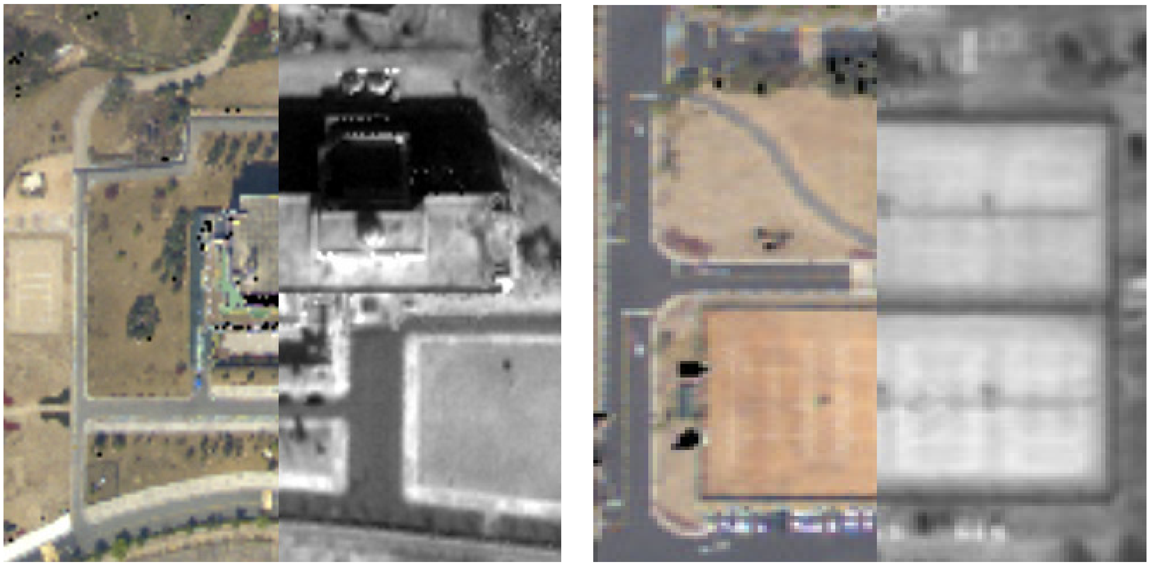

(a) (b)

Figure 6.2. Change detection between DSS (color) and IKONOS (b/w) orthophotos. Smooth transition between the two orthophotos can be observed in (a) while discontinuities are observed in (b) due to changes in the object space.

Figure 6.3. Textured 3D model produced by rendering optical images on LIDAR data

(a)

(b)

Figure 6.4. An orthophoto generated from Canon EOS 1D imagery in KOREA I dataset using differential rectification (a) and using true orthophoto generation technique (b)

REFERENCES

Abdel-Aziz, Y., and H. Karara, 1971. Direct linear transformation from comparator coordinates into object space coordinates in close-range photogrammetry, *American Society of Photogrammetry, Symposium on Close-Range Photogrammetry*, Urbana, Illinois 433, pp. 1-18.

Ackermann, F., 1999. Airborne laser scanning – present status and future expectations, *ISPRS Journal of Photogrammetry & Remote Sensing*. 54(2-3):64-67.

ANZLIC (Australia and New Zealand Land Information Council), 2006. Glossary:spatial information related terms, Retrieved March 23, 2006 from http://www.anzlic.org.au/glossary_terms.html

Baltsavias, E., 1999. A comparison between photogrammetry and laser scanning, *ISPRS Journal of Photogrammetry & Remote Sensing*, 54(1):83–94.

Brown, L., 1992. A survey of image registration techniques, *ACM computing surveys*, 24(4):325-376.

Chen, L., T. Teo, Y. Shao, Y. Lai, and J. Rau, J., 2004. Fusion of LIDAR data and optical imagery for building modeling, *International Archives of Photogrammetry and Remote Sensing*, 35(B4):732-737.

Cramer, M., D. Stallmann, and N. Haala, 2000. Direct georeferencing using GPS/Inertial exterior orientations for photogrammetric applications, *International Archives of Photogrammetry and Remote Sensing*, 33(B3):198-205.

Ebner, H., and T. Ohlhof, 1994. Utilization of ground control points for image orientation without point identification in image space, *International Archives of Photogrammetry and Remote Sensing*, 30(3/1):206–211.

El-Rabbany, A., 2002. *Introduction to GPS: The Global Positioning System*, Artech House Inc., Boston, Massachusetts.

El-Sheimy, N, C. Valeo, and A. Habib, 2005. *Digital Terrain Modelling: Acquisition, Manipulation and Applications*, Artech House, Inc., Norwood, Massachusetts.

Faruque, F., 2003. LIDAR image processing creates useful imagery. *ArcUser Magazine*, January-March 2003, Vol. 6, No.1.

Fonseca, L., and B. Manjunath, 1996. Registration techniques for multisensor remotely sensed imagery, *Photogrammetric Engineering and Remote Sensing*, 62(9):1049-1056.

Habib, A., 2006. ENGO 531 Course Notes, http://dprg.geomatics.ucalgary.ca (Last accessed April 25, 2006).

Habib, A., and B. Beshah, 1998. Multi sensor aerial triangulation, *ISPRS Journal of Photogrammetry and Remote Sensing,* Commission III Symposium in Columbus, Ohio, pp. 37-41.

Habib, A., and M. Morgan, 2003a. Automatic calibration of low-cost digital cameras, *Journal of Optical Engineering*, 42(4):948-955, April 2003.

Habib, A., and M. Morgan, 2003b. Linear features in photogrammetry, Invited Paper, *Geodetic Science Bulletin*, 9 (1): 3.

Habib, A., and T. Schenk, 1999. A new approach for matching surfaces from laser scanners and optical sensors, *International Archives of Photogrammetry and Remote Sensing*, 32(3W14):55-61.

Habib, A., H. Lin, and M. Morgan, 2003. Autonomous space resection using point- and line-based representation of free-form control linear features, *Journal of Photogrammetric Record*, 18 (103): 244-258.

Habib, A., K. Kim, S. Shin, C. Kim, K. Bang, E. Kim, D. Lee, 2006a. Comprehensive analysis of sensor modeling alternatives for high resolution imaging satellites, *Photogrammetric Engineering and Remote Sensing,* (accepted for publication).

Habib, A., M. Morgan, and Y. Lee, 2002. Bundle adjustment with self-calibration using straight lines, *Photogrammetric Record*, 17(100): 635-650.

Habib, A., R. Cheng, E. Kim, E. Mitishita, R. Frayne, and J. Ronsky, 2006b. Automatic surface matching for the registration of LIDAR data and MR imagery. *Electronics and Telecommunications Research Institute Journal,* (accepted for publication).

Habib, A., Y., Lee, and M. Morgan, 2001. Surface matching and change detection using modified iterative Hough transform for robust parameter estimation, *Photogrammetric Record*, 17 (98): 303-315.

Heuvel, F., 2000. Line-photogrammetry and its application for reconstruction from a single image, Jahrestagung der DGPF, Essen, *Publikationen der Deutschen Gesellschaft für Photogrammetrie und Fernerkundung*, Vol. 8, 255-263.

Huber H., W. Schickler, S. Hinz, and A. Baumgartner, 2003. Fusion of Lidar data and aerial imagery for automatic reconstruction of building surfaces, *The 2nd GRSS/ISPRS Joint Workshop on Data fusion and remote sensing over urban areas*, Berlin, May 2003, pp. 82–86.

Jaw, J., 1999. Control surface in aerial triangulation, Ph.D. dissertation, The Dept. of Civil and Environmental Engineering and Geodetic Science, The Ohio State University, Columbus, Ohio.

Jaw, J., and Y. Wu, 2006, Control patches for automatic single photo orientation, *Photogrammetric Engineering & Remote Sensing*, Vol. 72, No. 2, February 2006, pp. 151-158.

Kilian, J., N. Haala, and M. Englich, 1996. Capture and evaluation of airborne laser scanner data, *International Archives of Photogrammetry and Remote Sensing*, 31(B3):383-388.

Kraus, K., 1993. Photogrammetry, *Volume 1: Fundamentals and standard processes*, Ferd. Dummler's Verlag, Bonn.

Kraus, K., 2002. Principles of airborne laser scanning. *Journal of the Swedish Society for Photogrammetry and Remote Sensing*, Stockholm, 1:53-56.

McGlone, J., 2004. Manual of photogrammetry 5th edition. *American Society of Photogrammetry and Remote Sensing*, Bethesda, Maryland.

Mikhail, E., J. Bethel, and J. McGlone, 2001. *Introduction to modern photogrammetry*, John Wiley & Sons, New York.

Mulawa, D., and E. Mikhail, 1988. Photogrammetric treatment of linear features, *International Archives of Photogrammetry and Remote Sensing*, 27(B10): III383-III393.

Nakagawa, M., R. Shibasaki, and Y. Kagawa, 2002. Fusion stereo linear CCD image and laser range data for building 3D urban model, *International Archives of Photogrammetry and Remote Sensing*, 34(4):200-211.

Postolov, Y., A. Krupnik, and K. McIntosh, 1999. Registration of airborne laser data to surfaces generated by photogrammetric means, *International Archives of Photogrammetry and Remote Sensing*, 32(3W14):95-99.

Rottensteiner F., J. Trinder, S. Clode, and K. Kubik, 2004. Building detection by Dempster-Shafer fusion of LIDAR data and multispectral aerial imagery. Proceedings of the 17th *International Conference on Pattern Recognition* (ICPR) at Cambridge (UK), Aug. 23-26.

Rottensteiner, F., and J. Jansa, 2002. Automatic extraction of building from LIDAR data and aerial images, *International Archives of Photogrammetry and Remote Sensing*, Vol.34, Part 4, pp. 295-301.

Satale, D., and M. Kulkarni, 2003. LiDAR in mapping. *Map India Conference GISdevelopment.net*. http://www.gisdevelopment.net/technology/gis/mi03129.htm (Last accessed March 28, 2006).

Savopol, F. and C. Armenakis, 2004. Assessment of Lidar and digital camera data in the context of rapid change detection methodologies. *International Archives of Photogrammetry, Remote Sensing and Spatial Information Sciences*, 35(B4):968-973.

Schenk T., 1999a. Photogrammetry and laser altimetry. Vol. 32, Part 3-W14, Proceedings of ISPRS Workshop “Mapping Surface Structure and Topography by Airborne and Spaceborn Lasers”, La Jolla, California, 9-11 November 1999, pp. 3-12.

Schenk, T., 1999b. Determining transformation parameters between surfaces without identical points, *Technical Report Photogrammetry No. 15*, Department of Civil and Environmental Engineering and Geodetic Science, OSU, 22 pages.

Schenk, T., 2001. Modeling and analyzing systematic errors in airborne laser scanners. *Technical Report Photogrammetry No. 19*, Department of Civil and Environmental Engineering and Geodetic Science, OSU, 39 pages.

Schenk, T., 2004. From point-based to feature-based aerial triangulation, *Photogrammetric Engineering & Remote Sensing*, 58(5):315-329.

Schenk, T., and B. Csatho, 2002. Fusion of LIDAR data and aerial imagery for a more complete surface description, *International Archives of Photogrammetry, Remote Sensing and Spatial Information Sciences* 34(3A):310-317.

Schenk, T., S. Seo, and B. Csatho, 2001. Accuracy study of airborne laser scanning data with photogrammetry, In: *International Archives of Photogrammetry and Remote Sensing*, vol. 34 (part 3/W4), Annapolis, MD, pp.113.

Wegmann, H., C. Heipke, and K. Jacobsen, 2004. Direct sensor orientation based on GPS network solutions, *International Archives of Photogrammetry and Remote Sensing*. 35(B1):153-158.

Wehr, A., and U. Lohr, 1999. Airborne laser scanning---an introduction and overview, *ISPRS Journal Of Photogrammetry And Remote Sensing* 54(2-3):68-82.

Wolf, P., and B. Dewitt, 2000. *Elements of Photogrammetry, with Applications in GIS*, McGraw-Hill, Boston (3rd Edition).

Vosselman, G., 2002. Fusion of laser scanning data, maps and aerial photographs for building reconstruction, *International Geoscience and Remote Sensing Symposium*, 2002, 24-28 June, Toronto,Canada, on CD-ROM.

APPENDIX A

Stochastic Model of the Planar Patches Mathematical Model

In Chapter 4, the mathematical model of co-registering was implemented through the constraint in Equation A.1

$$\begin{aligned}\mathbf{V} = \; & \mathbf{X_P}\{\mathbf{Y_A}(\mathbf{Z_B}-\mathbf{Z_C})-\mathbf{Z_A}(\mathbf{Y_B}-\mathbf{Y_C})+(\mathbf{Y_B Z_C}-\mathbf{Y_C Z_B})\} \\ & -\mathbf{Y_P}\{\mathbf{X_A}(\mathbf{Z_B}-\mathbf{Z_C})-\mathbf{Z_A}(\mathbf{X_B}-\mathbf{X_C})+(\mathbf{X_B Z_C}-\mathbf{X_C Z_B})\} \\ & +\mathbf{Z_P}\{\mathbf{X_A}(\mathbf{Y_B}-\mathbf{Y_C})-\mathbf{Y_A}(\mathbf{X_B}-\mathbf{X_C})+(\mathbf{X_B Y_C}-\mathbf{X_C Y_B})\} \\ & -1\cdot\{\mathbf{X_A}(\mathbf{Y_B Z_C}-\mathbf{Y_C Z_B})-\mathbf{Y_A}(\mathbf{X_B Z_C}-\mathbf{X_C Z_B})+\mathbf{Z_A}(\mathbf{X_B Y_C}-\mathbf{X_C Y_B})\}=0\end{aligned} \tag{A.1}$$

This nonlinear relation between the parameters and observations must be linearized to be included in the general photogrammetric bundle adjustment procedure. In this model, both the parameters and the observations should be treated as observations infected by random errors and linearization should be done with respect to the parameters and the observations. The Gauss-Helmert (condition equations with parameters) model is used for solving the problem, as stated in Equation A.2.

$$\mathbf{w}=\mathbf{By}=\mathbf{A}\xi+\mathbf{Be} \qquad \mathbf{e}\sim\left(\mathbf{0},\sigma_o^2\mathbf{P}^{-1}\right) \tag{A.2}$$

where

- **w** is the vector of linear combinations of the random vector, **y** (or, when B is the Jacobian of the linearized observation equations, the vector of linear combinations of the incremental changes in observations),
- **B** is the nonrandom Jacobian matrix of the linearized observation equations with respect to the observations.

- **y** is an *n x 1* random vector of observations (or, when B is the Jacobian of the linearized observation equations, a vector of incremental changes in observations),
- **A** is an *n x m* non-random design matrix of rank q ≤ m built from the linear relationships between the parameters to be estimated and the observations (again, this is typically the Jacobian matrix defining a local differential relationship between parameters and observations),
- ξ is the *m x 1* non-random parameter vector (or incremental parameter vector of the linearized observation equations),
- **e** is the *n x 1* random error vector,
- **P** is an *n x n* weight matrix.

This condition is applied for each LIDAR point within the patch under consideration. The solution proceeds by building the components of the normal system as shown in the following steps.

Let $\mathbf{M} = \mathbf{B}\mathbf{P}^{-1}\mathbf{B}^{\mathrm{T}}$, then the normal matrix and normal vector can be written as in Equations A.3 and A.4, respectively:

$$\mathbf{N} = \mathbf{A}^{\mathrm{T}}\mathbf{M}^{-1}\mathbf{A} \tag{A.3}$$

$$\mathbf{C} = \mathbf{A}^{\mathrm{T}}\mathbf{M}^{-1}\mathbf{w} \tag{A.4}$$

And the estimated parameters are found as shown in Equation A.5

$$\hat{\xi} = \mathbf{N}^{-1}\mathbf{C} = \left(\mathbf{A}^{\mathrm{T}}\mathbf{M}^{-1}\mathbf{A}\right)^{-1}\mathbf{A}^{\mathrm{T}}\mathbf{M}^{-1}\mathbf{w} = \left(\mathbf{A}^{\mathrm{T}}\left(\mathbf{B}\mathbf{P}^{-1}\mathbf{B}^{\mathrm{T}}\right)^{-1}\mathbf{A}\right)^{-1}\mathbf{A}^{\mathrm{T}}\left(\mathbf{B}\mathbf{P}^{-1}\mathbf{B}^{\mathrm{T}}\right)^{-1}\mathbf{w} \tag{A.5}$$

The dispersion of estimated parameters are shown in Equation A.6

$$\mathbf{D}\left\{\hat{\xi}\right\} = \sigma_o^2\mathbf{N}^{-1} = \sigma_o^2\left(\mathbf{A}^T\mathbf{M}^{-1}\mathbf{A}\right)^{-1} = \sigma_o^2\left(\mathbf{A}^T\left(\mathbf{BP}^{-1}\mathbf{B}^T\right)^{-1}\mathbf{A}\right)^{-1} \tag{A.6}$$

The predicted errors and residuals are shown in Equations A.7and A.8 respectively:

$$\tilde{\mathbf{e}} = \mathbf{B}^{-1}(\mathbf{w} - \mathbf{A}\hat{\xi}) \tag{A.7}$$

$$\tilde{\tilde{\mathbf{e}}} = \mathbf{B}\tilde{\mathbf{e}} = \mathbf{w} - \mathbf{A}\hat{\xi} \tag{A.8}$$

The variance component can be estimated from Equation A.9:

$$\hat{\sigma}_o^2 = \frac{\tilde{\tilde{\mathbf{e}}}^T\mathbf{M}^{-1}\tilde{\tilde{\mathbf{e}}}}{\mathbf{r}} = \frac{(\mathbf{B}\tilde{\mathbf{e}})^T\mathbf{M}^{-1}\mathbf{B}\tilde{\mathbf{e}}}{\mathbf{r}} = \frac{(\mathbf{B}\tilde{\mathbf{e}})^T\left(\mathbf{BP}^{-1}\mathbf{B}^T\right)^{-1}\mathbf{B}\tilde{\mathbf{e}}}{\mathbf{r}} \tag{A.9}$$

The partial derivatives of the mathematical model, Equation A.1 with respect to the parameters, repeated her in Equation A.10

$$\begin{aligned} \mathbf{V} = \;& \mathbf{X_P}\{\mathbf{Y_A}(\mathbf{Z_B} - \mathbf{Z_C}) - \mathbf{Z_A}(\mathbf{Y_B} - \mathbf{Y_C}) + (\mathbf{Y_B Z_C} - \mathbf{Y_C Z_B})\} \\ & - \mathbf{Y_P}\{\mathbf{X_A}(\mathbf{Z_B} - \mathbf{Z_C}) - \mathbf{Z_A}(\mathbf{X_B} - \mathbf{X_C}) + (\mathbf{X_B Z_C} - \mathbf{X_C Z_B})\} \\ & + \mathbf{Z_P}\{\mathbf{X_A}(\mathbf{Y_B} - \mathbf{Y_C}) - \mathbf{Y_A}(\mathbf{X_B} - \mathbf{X_C}) + (\mathbf{X_B Y_C} - \mathbf{X_C Y_B})\} \\ & - 1 \cdot \{\mathbf{X_A}(\mathbf{Y_B Z_C} - \mathbf{Y_C Z_B}) - \mathbf{Y_A}(\mathbf{X_B Z_C} - \mathbf{X_C Z_B}) + \mathbf{Z_A}(\mathbf{X_B Y_C} - \mathbf{X_C Y_B})\} = 0 \end{aligned} \tag{A.10}$$

- With respect to point A(X_A,Y_A,Z_A):

$$\begin{aligned} \frac{\partial \mathbf{V}}{\partial \mathbf{X_A}} &= -\mathbf{Y_P}(\mathbf{Z_B} - \mathbf{Z_C}) + \mathbf{Z_P}(\mathbf{Y_B} - \mathbf{Y_C}) - (\mathbf{Y_B Z_C} - \mathbf{Y_C Z_B}) \\ \frac{\partial \mathbf{V}}{\partial \mathbf{Y_A}} &= \mathbf{X_P}(\mathbf{Z_B} - \mathbf{Z_C}) - \mathbf{Z_P}(\mathbf{X_B} - \mathbf{X_C}) + (\mathbf{X_B Z_C} - \mathbf{X_C Z_B}) \\ \frac{\partial \mathbf{V}}{\partial \mathbf{Z_A}} &= -\mathbf{X_P}(\mathbf{Y_B} - \mathbf{Y_C}) + \mathbf{Y_P}(\mathbf{X_B} - \mathbf{X_C}) - (\mathbf{X_B Y_C} - \mathbf{X_C Y_B}) \end{aligned} \tag{A.11}$$

- With respect to point B(X_B,Y_B,Z_B)

$$\begin{aligned} \frac{\partial \mathbf{V}}{\partial \mathbf{X_B}} &= \mathbf{Y_P}\{\mathbf{Z_A} - \mathbf{Z_C}\} + \mathbf{Z_P}\{\mathbf{Y_C} - \mathbf{Y_A}\} + \{\mathbf{Y_A Z_C} - \mathbf{Z_A Y_C}\} \\ \frac{\partial \mathbf{V}}{\partial \mathbf{Y_B}} &= \mathbf{X_P}\{\mathbf{Z_C} - \mathbf{Z_A}\} + \mathbf{Z_P}\{\mathbf{X_A} - \mathbf{X_C}\} - \{\mathbf{X_A}(\mathbf{Z_C}) + \mathbf{Z_A} - \mathbf{X_C}\} \end{aligned} \tag{A.12}$$

$$\frac{\partial \mathbf{V}}{\partial \mathbf{Z_B}} = \mathbf{X_P}\{\mathbf{Y_A}\mathbf{Z_B} - \mathbf{Y_C}\} + \mathbf{Y_P}\{\mathbf{X_C} - \mathbf{X_A}\} + \{\mathbf{X_A}\mathbf{Y_C} - \mathbf{X_C}\mathbf{Y_A}\}$$

- With respect to point $C(X_C,Y_C,Z_C)$

$$\frac{\partial \mathbf{V}}{\partial \mathbf{X_C}} = -\mathbf{Y_P}\{\mathbf{Z_A} - \mathbf{Z_B}\} + \mathbf{Z_P}\{\mathbf{Y_A} - \mathbf{Y_B}\} + \{\mathbf{Z_A}\mathbf{Y_B} - \mathbf{Y_A}\mathbf{Z_B}\}$$

$$\frac{\partial \mathbf{V}}{\partial \mathbf{Y_C}} = \mathbf{X_P}\{\mathbf{Z_A} - \mathbf{Z_B}\} + \mathbf{Z_P}\{-\mathbf{X_A} + \mathbf{X_B}\} - \{\mathbf{X_A}\mathbf{Z_B} + \mathbf{Z_A}\mathbf{X_B}\} \tag{A.13}$$

$$\frac{\partial \mathbf{V}}{\partial \mathbf{Z_C}} = \mathbf{X_P}\{-\mathbf{Y_A} + \mathbf{Y_B}\} - \mathbf{Y_P}\{-\mathbf{X_A} + \mathbf{X_B}\} - \{\mathbf{X_A}\mathbf{Y_B} - \mathbf{Y_A}\mathbf{X_B}\}$$

The Jacobian matrix **A** is constructed for each point and then used to update the general normal matrix (**N**) and the normal vector (**C**) as seen in Equations A.14.

$$\mathbf{A_A} = \begin{bmatrix} \frac{\partial \mathbf{V}}{\partial \mathbf{X_A}} & \frac{\partial \mathbf{V}}{\partial \mathbf{Y_A}} & \frac{\partial \mathbf{V}}{\partial \mathbf{Z_A}} \end{bmatrix}$$

$$\mathbf{A_B} = \begin{bmatrix} \frac{\partial \mathbf{V}}{\partial \mathbf{X_B}} & \frac{\partial \mathbf{V}}{\partial \mathbf{Y_B}} & \frac{\partial \mathbf{V}}{\partial \mathbf{Z_B}} \end{bmatrix} \tag{A.14}$$

$$\mathbf{A_C} = \begin{bmatrix} \frac{\partial \mathbf{V}}{\partial \mathbf{X_C}} & \frac{\partial \mathbf{V}}{\partial \mathbf{Y_C}} & \frac{\partial \mathbf{V}}{\partial \mathbf{Z_C}} \end{bmatrix}$$

The partial derivatives of the mathematical model, Equation A.1 with respect to the observations, $P(X_P,Y_P,Z_P)$:

$$\frac{\partial \mathbf{V}}{\partial \mathbf{X_P}} = \mathbf{Y_A}(\mathbf{Z_B} - \mathbf{Z_C}) - \mathbf{Z_A}(\mathbf{Y_B} - \mathbf{Y_C}) + (\mathbf{Y_B}\mathbf{Z_C} - \mathbf{Y_C}\mathbf{Z_B})$$

$$\frac{\partial \mathbf{V}}{\partial \mathbf{Y_P}} = -\mathbf{X_A}(\mathbf{Z_B} - \mathbf{Z_C}) - \mathbf{Z_A}(\mathbf{X_B} - \mathbf{X_C}) + (\mathbf{X_B}\mathbf{Z_C} - \mathbf{X_C}\mathbf{Z_B}) \tag{A.15}$$

$$\frac{\partial \mathbf{V}}{\partial \mathbf{Z_P}} = \mathbf{X_A}(\mathbf{Y_B} - \mathbf{Y_C}) - \mathbf{Y_A}(\mathbf{X_B} - \mathbf{X_C}) + (\mathbf{X_B}\mathbf{Y_C} - \mathbf{X_C}\mathbf{Y_B})$$

The Jacobian matrix **B** with respect to the observations which are the coordinates of each LIDAR point (X_P,Y_P,Z_P) is shown in Equation A.16:

$$\mathbf{B_P} = \begin{bmatrix} \dfrac{\partial \mathbf{V}}{\partial \mathbf{X_P}} & \dfrac{\partial \mathbf{V}}{\partial \mathbf{Y_P}} & \dfrac{\partial \mathbf{V}}{\partial \mathbf{Z_P}} \end{bmatrix} \tag{A.16}$$

As for the observation vector **w**, we use the differential between the observed (assumed) quantity and its estimation since we have a linearized system,

$$\mathbf{w} = \mathbf{By} = 0 - \mathbf{V} = -\begin{pmatrix} \mathbf{X_P}\{\mathbf{Y_A}(\mathbf{Z_B}-\mathbf{Z_C}) - \mathbf{Z_A}(\mathbf{Y_B}-\mathbf{Y_C}) + (\mathbf{Y_B}\mathbf{Z_C}-\mathbf{Y_C}\mathbf{Z_B})\} \\ -\mathbf{Y_P}\{\mathbf{X_A}(\mathbf{Z_B}-\mathbf{Z_C}) - \mathbf{Z_A}(\mathbf{X_B}-\mathbf{X_C}) + (\mathbf{X_B}\mathbf{Z_C}-\mathbf{X_C}\mathbf{Z_B})\} \\ +\mathbf{Z_P}\{\mathbf{X_A}(\mathbf{Y_B}-\mathbf{Y_C}) - \mathbf{Y_A}(\mathbf{X_B}-\mathbf{X_C}) + (\mathbf{X_B}\mathbf{Y_C}-\mathbf{X_C}\mathbf{Y_B})\} \\ -\mathbf{1}\cdot\{\mathbf{X_A}(\mathbf{Y_B}\mathbf{Z_C}-\mathbf{Y_C}\mathbf{Z_B}) - \mathbf{Y_A}(\mathbf{X_B}\mathbf{Z_C}-\mathbf{X_C}\mathbf{Z_B}) + \mathbf{Z_A}(\mathbf{X_B}\mathbf{Y_C}-\mathbf{X_C}\mathbf{Y_B})\} \end{pmatrix} \tag{A.17}$$

Finally, the updates to the general normal matrix can formulated as shown in Equations A.18

$$\begin{aligned}
\mathbf{N_{11}} &= \mathbf{A_A^T}\left(\mathbf{BP^{-1}B^T}\right)^{-1}\mathbf{A_A} \\
\mathbf{N_{12}} &= \mathbf{A_A^T}\left(\mathbf{BP^{-1}B^T}\right)^{-1}\mathbf{A_B} \\
\mathbf{N_{13}} &= \mathbf{A_A^T}\left(\mathbf{BP^{-1}B^T}\right)^{-1}\mathbf{A_C} \\
\mathbf{N_{21}} &= \mathbf{A_B^T}\left(\mathbf{BP^{-1}B^T}\right)^{-1}\mathbf{A_A} \\
\mathbf{N_{22}} &= \mathbf{A_B^T}\left(\mathbf{BP^{-1}B^T}\right)^{-1}\mathbf{A_B} \\
\mathbf{N_{23}} &= \mathbf{A_B^T}\left(\mathbf{BP^{-1}B^T}\right)^{-1}\mathbf{A_C} \\
\mathbf{N_{31}} &= \mathbf{A_C^T}\left(\mathbf{BP^{-1}B^T}\right)^{-1}\mathbf{A_A} \\
\mathbf{N_{32}} &= \mathbf{A_C^T}\left(\mathbf{BP^{-1}B^T}\right)^{-1}\mathbf{A_B} \\
\mathbf{N_{33}} &= \mathbf{A_C^T}\left(\mathbf{BP^{-1}B^T}\right)^{-1}\mathbf{A_C}
\end{aligned} \tag{A.18}$$

With $\mathbf{M} = \mathbf{BP^{-1}B^T}$, these updates are added to the overall normal matrix in the locations shown in Figure A.1.

As for the normal vector **C**, the updates ($\mathbf{C_A}$**,** $\mathbf{C_B}$**,** $\mathbf{C_C}$) are constructed and added to the general C vector as shown in Equations A.19 and Figure A.2 respectively.

$$\begin{aligned}
\mathbf{C_A} &= \mathbf{A_A^T}\,\mathbf{M^{-1}}\,\mathbf{w} \\
\mathbf{C_B} &= \mathbf{A_B^T}\,\mathbf{M^{-1}}\,\mathbf{w} \\
\mathbf{C_C} &= \mathbf{A_C^T}\,\mathbf{M^{-1}}\,\mathbf{w}
\end{aligned} \tag{A.19}$$

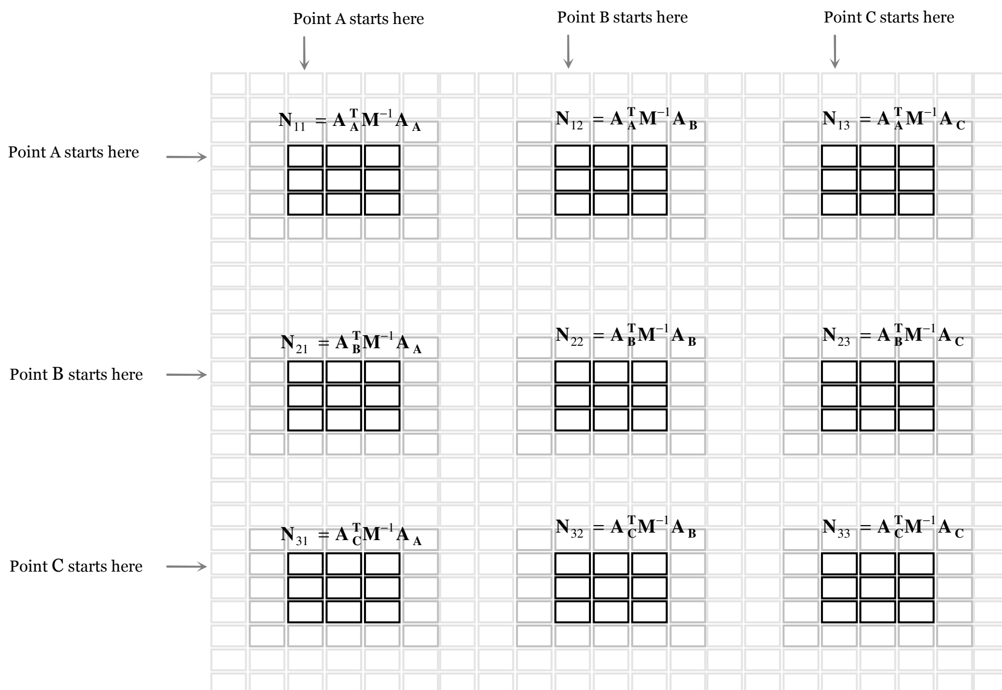

Figure A.1. Updates to the normal matrix **N**

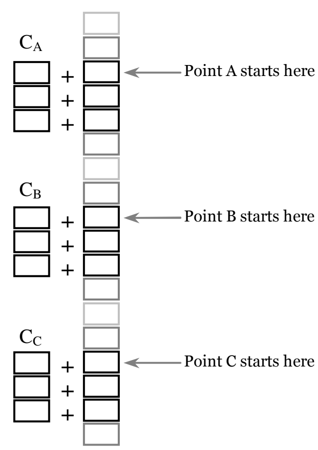

Figure A.2. Updates to the normal vector **C**

APPENDIX B

Published Work

Journal Papers

1. Habib, A., M. Ghanma, M. Morgan, and R. Al-Ruzouq, 2005, Photogrammetric and LIDAR Data Registration Using Linear Features, Photogrammetric Engineering & Remote Sensing, Vol. 71, No. 6, June 2005, pp. 699–707
2. Habib, A., M. Ghanma, and E. Mitishita, 2004, Co-Registration of Photogrammetric and LIDAR Data: Methodology and Case Study, (Invited paper), Brazilian Journal of Cartography (RBC), Vol. 56/01, July 2004, pp.1-13.
3. Habib, A., M. Ghanma, and E. Mitishita, 2005, Photogrammetric Georeferencing Using LIDAR Linear and Areal Features, (Invited paper), Korean Journal of Geomatics, Vol. 5, No. 1, December 2005, pp. 7-19.
4. Habib, A., M. Ghanma, S. Shin, K. Kim, C. Kim, E. Kim. Algorithms for Multi-Sensor and Multi-Primitive Photogrammetric Triangulation. Submitted to the ISPRS Journal, April, 2006.

Conferences:

5. Habib, A., M. Ghanma, E. Mitishita, A. Machado, E. Kim, C. Kim, 2005, Comparative Analysis of the Performance of Metric-Analog Cameras, Amateur-Digital Cameras, and LIDAR, IGARSS 2005, International Geoscience and Remote Sensing Symposium, Soul, Korea (27-29 July, 2005)
6. Habib, A., M. Ghanma, and E. Mitishita, 2005, Indirect Geo-Referencing of Photogrammetric Models Using LIDAR Data, Canadian Institute of Geomatics 98th Annual Conference, "Geomatics: Powering the Future", Ottawa, Ontario, Canada, (13-15 June, 2005)
7. Habib, A. and M. Ghanma, 2005, Lidar Features for the Indirect Geo-Referencing of Photogrammetric Data, ISPRS Working Group I/2 Workshop

2005, "3D Mapping from InSAR and LiDAR", Banff, Alberta, Canada, (7-10 June, 2005)

8. Mitishita, E., A. Habib, A., Machado, and M. Ghanma, 2005, Urban Vector Mapping Using Low Cost Digital Cameras and Lidar Data: A Case Study, ISPRS Working Group I/2 Workshop 2005, "3D Mapping from InSAR and LiDAR", Banff, Alberta, Canada, (7-10 June, 2005)

9. Habib, A., M. Ghanma, 2005, Co-Registration of Photogrammetric and LIDAR Surfaces for the Evaluation and Validation of Systems' Calibration, GEOIDE's 7th Annual Scientific Conference, Québec, Québec, Canada (29-31 May 2005)

10. Ghanma, M. 2005, New Approach for Image Geo-Referencing Utilizing LIDAR Data, The Second Annual Faculty of Engineering Graduate Student Research Conference, Calgary, Canada (2-3 May 2005)

11. Habib, A., M. Ghanma, E. Kim, 2005, LIDAR Data for Photogrammetric Geo-Referencing, FIG Working Week 2005 and GSDI-8, "From Pharaohs to Geoinformatics", Cairo, Egypt, (16–21 April 2005)

12. Habib, A., M. Ghanma, M. F. Morgan, E. Mitishita, 2004, Integration of Laser and Photogrammetric Data for Calibration Purposes, XXth ISPRS Congress, Istanbul, Turkey, PS WG II/2 Systems for SAR and LIDAR Processing, pp.170, (12-23 July 2004)

13. Habib, A., M. Ghanma, M. Tait, 2004, Integration of LIDAR and Photogrammetry for Close Range Applications, XXth ISPRS Congress, Istanbul, Turkey, PS ThS 1 Integration and Fusion of Data and Models, (12-23 July 2004)

14. Habib, A., M. Ghanma , C. J. Kim, E. Mitishita, 2004, Alternative Approaches for Utilizing LIDAR Data as a Source of Control Information for Photogrammetric Models, XXth ISPRS Congress, Istanbul, Turkey, PS WG I/5 Platform and Sensor Integration, pp.193, (12-23 July 2004)

15. Habib, A., Ghanma, M., Tait, M., and Fox, R., 2003. Using Ground Based Laser Scanners to Establish the Orientation of Terrestrial Imagery. Proceedings of the 6th Conference on Optical 3-D Measurements Techniques, pp. 306-314, Zurich, Switzerland, (22-15 September 2003)

Reports:

16. Habib, A., Ghanma, M., Al-Ruzouq, R., Morgan, M., Mrstik, P., Mitishita, E., 2005. Co-Registration of Photogrammetric And LIDAR Surfaces. Submitted to the GEOIDE Research Network, Canada. (52 pages).

17. Habib, A., Ghanma, 2005. Development of Multi-Sensor and Multi-Primitive Triangulation Algorithms: Incorporation of LIDAR Data in Photogrammetric Triangulation. Submitted to the Korean Electronics and Telecommunications Research Institute (ETRI), Korea. (67 pages).